

Saving Lives and Charting a Path to the Future.



KIST's Brain Science Institute specializes in convergence research encompassing neuroscience, micro systems engineering, medicine, pharmacology and genetics. The goal of this research is to understand the neural mechanisms responsible for controlling human behavior and to look for ways to overcome brain dysfunctions. By unraveling the mysteries of the brain, the Brain Science Institute will become a hub for international brain science research.

Korea Institute of Science and Technology

KISToday
Vol. 6 No. 1 April 2013

Vol. 6 No. 1 April 2013
ISSN 2005-9043

Bio / Medical

• **Technical Review**

A Single Vesicle Fusion Assay for *In Vitro* Studies of SNARE-Induced Vesicle Fusion

Materials / Systems

• **Technical Review**

Reducing Pollution by Abatement of NO_x Emissions Through NH₃ SCR

Energy / Environment

• **Technical Review**

Organic Semiconductors for High Performance Ambipolar Field Effect Transistors

Contents

Foreword	03
Bio / Medical	
Technical Review	
A Single Vesicle Fusion Assay for <i>In Vitro</i> Studies of SNARE-Induced Vesicle Fusion	04
Feature Articles	
Phosphorescent Nanoparticles for Quantitative Measurements of Oxygen Profiles <i>In Vitro</i> and <i>In Vivo</i>	12
Increase in Antioxidant and Anticancer Effects of Ginsenoside by Maillard Reaction	20
Design, Synthesis and Biological Evaluation of Novel Antidepressants: 3-Substituted Azetidine Derivatives as Triple Reuptake Inhibitors	25
Materials / Systems	
Technical Review	
Reducing Pollution by Abatement of NO _x Emissions Through NH ₃ SCR	30
Feature Articles	
Real-Time <i>In Vivo</i> Imaging of the Beating Mouse Heart at Microscopic Resolution	39
Highly Efficient Transparent Gas Sensors	47
Strain Evolution of Each Grain Type In Poly-Crystalline (Ba,Sr)TiO ₃ Thin Films Grown by Sputtering	54
Energy / Environment	
Technical Review	
Organic Semiconductors for High Performance Ambipolar Field Effect Transistors	60
Feature Articles	
Development of Low-Temperature Solid Oxide Fuel Cells with Thin Bilayer Electrolytes Produced by Chemical Solution Deposition	67
Analysis of Rainwater Quality and Quantity for Effective Urban Water Management	73
Effect of Steric Factors Affecting the Preferential Diffusion of Cu(II) in Mesoporous Structures	78
Research Highlights	84
KIST News	90
A Sign of the Times	94
Interview	96

Foreword

William Temple, a Bishop of the Church of England and highly respected teacher, once said that the existence of science lies in the ceaseless spirit that does not rest. This statement sums up what our goal is at KIST: to continuously strive for innovation rather than be content with prior achievements or the status quo.

Despite a difficult economic climate, KIST was still able to achieve many outstanding results in 2012. Some of our more important accomplishments included:

- an improved level of research performance as evidenced by ten articles published in the distinguished international journals *Nature* and *Cell*;
- selection of memory research conducted by our Brain Science Research Center as one of the ten greatest science and technology news items of the year by the Korean Federation of Science and Technology Societies.
- commissioned research totaling 246 billion won;
- an income of 4.5 billion won from technology royalties, including technology transfers to advanced countries such as the U.S. and Italy.

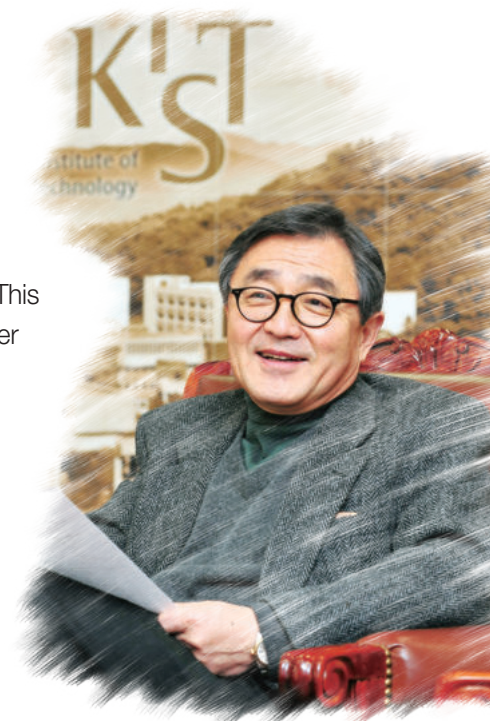
In the international arena we continue to be very active, particularly in providing support and building relationships in the developing world. Two milestones in 2012 were:

- the completion of a pilot plant for the production of bio-ethanol in Serpong, Indonesia; and
- the signing of a Memorandum of Understanding with the government of Vietnam to establish V-KIST, an institute of science and technology, based on KIST as an operating model.

We've made a strong start to the year and look forward to many new ventures in 2013. There are many exciting changes occurring in our country, including the election of Korea's first female president, the transfer of government offices to Sejong City, and the reorganization of many levels of government including the Ministry of Science and Technology which will now be responsible for the future growth and advancement of Korea.

With the efforts of our outstanding staff, I am confident that KIST will continue to provide the very finest scientific and technological research in this dynamic, changing environment.

Dr. Kil-Choo Moon
President of KIST



[Technical Review]

A Single Vesicle Fusion Assay for *In Vitro* Studies of SNARE-Induced Vesicle Fusion



Cherlhyun Jeong

Center for
Theragnosis
che.jeong@
ksit.re.kr



Yoosoo Yang

chirpy84@
gmail.com



Yeon-Kyun Shin

colishin@
iastate.edu

Introduction

Neurotransmitter release at synapses, a process critical to the brain's major functions in areas such as cognition, emotion and memory, requires that synaptic vesicles fuse with the presynaptic plasma membrane. Once the vesicle is delivered to the plasma membrane (PM), it docks there prior to the fusion. The fusion of two lipid membranes in an aqueous medium is an inefficient process due to the presence of a repulsive hydration force [1]. It has been suggested that "bridging" proteins can act as a fusion machine to provide the necessary energy for membrane fusion [2]. Members of a superfamily of membrane proteins, called SNAREs (Soluble N-ethylmaleimide-sensitive factor attachment protein receptors), are known to be essential to all exocytotic membrane fusion, including synaptic vesicle fusion [3-5].

All SNARE systems consist of two cognate pairs, v- and t-SNAREs (vesicular and target SNAREs), which are anchored in two fusing membranes. They can form a four- α -helix bundle via association of their "SNARE motifs" that are composed of 15 hydrophobic core layers (60 amino acid residues) [6]. The SNARE motifs are unstructured when the SNAREs are free in the solution. However, when the proteins on opposing membranes interact, their SNARE motifs undergo spontaneous restructuring into a highly stable, elongated four helical coiled-coil structure called the "core complex" [7, 8].

The neuronal SNAREs are largely responsible for the fast (sub-milliseconds) neurotransmitter release. The t-SNARE proteins on the presynaptic membrane, consisting of Syntaxin 1a, SNAP-25 and v-SNARE VAMP2 on the synaptic vesicle, form a four-helix bundle, which bridges two membranes in *trans*- and mediates fusion. The fast calcium-triggered neurotransmitter release is the result of the fusion of the synaptic vesicle membrane to the plasma membrane and is driven by the neuronal SNARE proteins, which are under tight regulation by a number of accessory proteins such as synaptotagmin, complexin and Munc18 [9, 10].

Method development

Since 1998, ensemble bulk fluorescence (Förster) resonance energy transfer (FRET) has been used as a standard *in vitro* tool for studying SNARE-mediated membrane fusion (henceforth referred to as bulk lipid-mixing assay) [5]. In the most commonly used scheme, v- and t-SNARE proteins are reconstituted into two independent populations of vesicles, where one population contains both acceptor and donor fluorophore-labeled lipophilic molecules and the other population contains no fluorophores. Upon fusion, lipid mixing results in a dilution of donors and acceptors, and the degree of fusion can be quantified from the recovery of the donor fluorescence emission. For SNARE protein reconstitution, both standard and direct methods have been widely used. The standard method is a co-micellization method whereby lipids and proteins are initially co-solubilized with detergent. The direct method refers to a preparation process whereby detergent-solubilized proteins are incorporated into preformed vesicles. The diameter of protein-reconstituted vesicles may be ascertained through electron microscopy or dynamic light scattering, and is ~50 nm by the standard method and ~90 nm by the direct method. A detailed comparison between standard and direct methods regarding vesicle size, protein

incorporation and fusion ability has been reported by the Rizo group [11].

Despite its common use, the bulk lipid-mixing assay cannot clearly distinguish different stages of the fusion process, such as docking, hemifusion and full fusion, due to ensemble averaging. Recognizing this limitation, many researchers developed fusion assays that can visualize the docking and fusion of individual vesicles to the planar bilayer [12-14]. Because having the SNARE proteins on the planar bilayer in close proximity to a glass surface may potentially influence the fusogenic function of the proteins [12-14], we sought an alternative approach in which the reaction observed is the fusion between two single vesicles [15]. In this assay, one set of vesicles is surface-tethered and the other set is free-floating above the surface. Unlike the bulk lipid-mixing assay in which both the donor and acceptor fluorophores are typically in the same vesicle before fusion, in the single-vesicle assay each pair is formed by one vesicle with donor fluorophore-conjugated lipids and another acceptor fluorophore-labeled vesicle. FRET between each pair of vesicles can be measured either after the samples have equilibrated and the unreacted vesicles have been washed away, or in real time as free-floating vesicles dock and fuse to the surface-tether vesicles. The data from the equilibrated samples can be used to differentiate between docked and lipid-mixed populations. Furthermore, through careful analysis of hundreds of real-time FRET efficiency trajectories (time resolution of 100–200 milliseconds), transient intermediate states between the docked (low FRET) and the fully lipid mixed (high FRET) state can be observed, strongly suggesting the presence of fusion intermediates, such as hemifusion. Using this assay, we have also shown evidence for distinct fusion pathways such as kiss-and-run events [15] and full-collapse fusion [16].

Nonetheless, this single vesicle-vesicle lipid mixing is still blind to fusion pore opening and expansion, the final crucial step of the full-collapse fusion pathway [17]. A fundamental assumption of using lipid mixing to study

membrane fusion is that there is a direct correlation between lipid and content mixing. However, a recent study on DNA-mediated membrane fusion showed that this might not be the case [17]. By comparing results from separate sets of experiments, one using lipid-mixing indicators and the other using content-mixing indicators, this study showed that a high level of lipid mixing can occur with a limited degree of content mixing, thus demonstrating that lipid mixing alone may be an insufficient marker for fusion pore opening [17]. The next-generation liposome fusion assay would have to use content-mixing reporters in addition to lipid-mixing reporters.

In order to study fusion pore expansion, we were inspired by the single-molecule vesicle encapsulation approach [18] to develop a single-molecule FRET-based vesicle-vesicle fusion assay with fluorescent probes encapsulated inside SNARE-reconstituted vesicles [16]. The probe, often referred to as a molecular beacon, is a DNA molecule conjugated with a donor fluorophore (Cy3) and an acceptor fluorophore (Cy5). By itself, the probe forms a hairpin structure so that the two fluorophores are close together, giving rise to high FRET. When a poly-A oligonucleotide is added, it hybridizes with the loop sequence (poly-T) of the hairpin probe, opening up the hairpin and reducing FRET. If the poly-A strand is encapsulated inside another vesicle, the FRET changes described here can only be seen when the two vesicles merge their content with a pore large enough for the DNA strand(s) to pass through.

Recently, Brunger and co-workers developed an advanced single vesicle-vesicle fusion assay that allows the simultaneous monitoring of lipid and content mixing by using a small content-mixing probe [19]. Subsequently, using methods detecting the intervesicular mixing of small and large cargoes at a single-vesicle level, Sulforhodamine B (SRB) and large DNA cargoes, Shin and co-workers [20] were able to analyze fusion pore formation and expansion in the presence of fusion effectors such as synaptotagmin 1 (Syt1), Ca^{2+} , and complexin.

Applications

By using our single vesicle-vesicle lipid-mixing assay on yeast SNAREs that function in membrane trafficking from endoplasmic reticulum to Golgi, we discovered multiple intermediates [15] and the role of the SN1 and SN2 helices of Sec9c [21]. For the neuronal SNARE system, we found the dual function of complexin (i.e., docking inhibition and enhancement of fusion after docking [22]), the rapid aggregation of vesicles induced by C2AB/ Ca^{2+} [23], the fusion-promoting role of Munc18 binding to the SNARE core [24] and fast lipid mixing induced by membrane-anchored synaptotagmin 1 [25]. By using our vesicle-vesicle content-mixing assay, we recently showed that fusion pore formation and expansion in neuronal SNARE-dependent vesicle fusion requires syt1 and Ca^{2+} [16].

Experimental design

Single-vesicle lipid-mixing assay. In our vesicle-vesicle lipid-mixing assay, the v- and t-SNARE proteins (or vice versa) are reconstituted into two different groups of vesicles labeled with acceptor (DiD) and donor (DiI) fluorophores, respectively. The acceptor-labeled vesicles are immobilized on the surface and then the donor-labeled vesicles are added in order to observe the formation of a single vesicle-vesicle complex through specific SNARE interactions [15] (Figure 1). A flow chamber is assembled on a quartz slide that has been coated with PEG cushions to eliminate nonspecific binding. The passivation of the flow chamber surface is crucial to ensure that (i) tethered vesicles are free of interaction with the surface and (ii) free-floating vesicles will not randomly adhere to the surface.

NeutrAvidin is then added to coat the surface. Through the specific interaction between NeutrAvidin and biotin-conjugated lipid molecule in the membrane, the v-SNARE vesicles are tethered to the bottom surface of the flow chamber. After washing out free v-SNARE

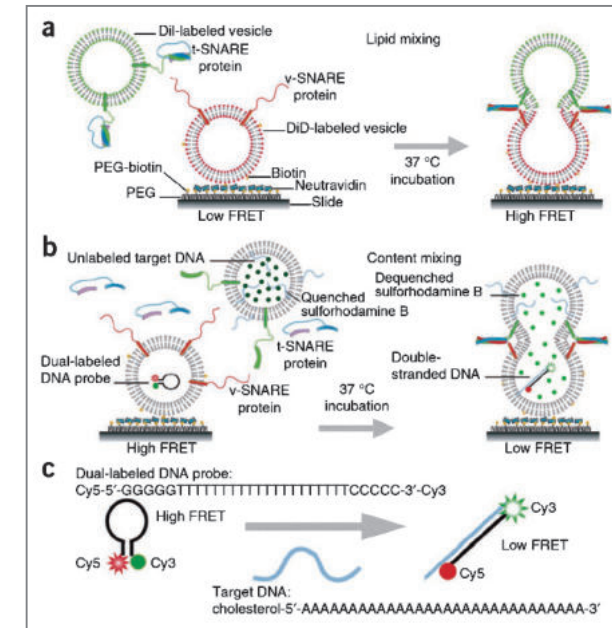


Figure 1. Experimental scheme. (a) Single vesicle-vesicle lipid-mixing assay: DiI (acceptor)-labeled v-SNARE vesicles are immobilized on the bottom surface of a flow chamber, which is also the imaging surface of the TIR fluorescence microscope. When t- and v-SNARE vesicles proceed to fuse, resultant lipid mixing will entail an increase in the FRET efficiency. (b) Single vesicle-vesicle content-mixing assay: vesicles reconstituted with v-SNARE proteins and encapsulating dual-labeled DNA probes (large DNA cargoes) or t-SNARE proteins with empty content are immobilized on the surface of the flow cell. Vesicles reconstituted with t-SNARE proteins and encapsulating complementary poly-A DNA strands or v-SNARE proteins and sulforhodamine B (small cargoes) are flowed in, and the sample is incubated at 37°C. (c) The Cy3/Cy5 dual-labeled DNA probe is a single-stranded oligonucleotide with a stem-and-loop hairpin structure. When the hairpin probe is in the closed state, Cy3 and Cy5 fluorophores linked to the ends are in close proximity and show a high FRET value. When the hairpin probe hybridizes to a target DNA, it switches to the open state, increasing the distance between two dyes and showing a low FRET value. The size of both the probe and target DNA molecules is several nanometers in diameter, which is much larger than the size of normal neurotransmitters.

vesicles, the t-SNARE vesicles are diluted with accessory proteins and injected into the flow chamber to induce assembly of SNARE complexes and membrane fusion between a single pair of t- and v-SNARE vesicles. The use of a low concentration of t-SNARE vesicles can dramatically reduce the probability of multiple vesicle interactions to guarantee an operation at the single vesicle-vesicle pair level. After incubation at 37°C, free

t-SNARE vesicles and accessory proteins are removed by washing, and FRET measurements are made using a total internal reflection (TIR) fluorescence microscope to reveal the final outcome of the fusion reaction. Docking and fusion reactions can also be observed in real time. From increasing values of the FRET efficiency, real-time fusion intermediates with different degrees of lipid mixing can be discerned. For example, an intermediate FRET is obtained for hemifusion, in which only the outer leaflets mix. From the hemifusion state, after merging inner leaflets, a fusion pore would open to mix content, which corresponds to the highest FRET value.

Single-vesicle content-mixing assay with sulforhodamine B (SRB). To monitor fusion pore opening, we adopted a single-vesicle assay based on content mixing of small cargoes (Figure 1b, sulforhodamine B) developed by Brunger and coworkers [19]. We prepared v-vesicles encapsulating SRB in a high enough concentration (50mM) to have fluorescence self-quenching and empty t-vesicles separately. The empty t-SNARE vesicles, reconstituted with t-SNARE proteins SNAP-25 and Syntaxin 1A, were immobilized on a polymer-coated quartz surface via biotinylated lipids. The v-SNARE vesicles, reconstituted with v-SNARE protein synaptobrevin 2 (or VAMP2), were then flown in and allowed to to the t-vesicle on the surface. We expected to observe a sudden increase of the SRB fluorescence signal due to dilution-induced fluorescence dequenching when content mixing occurred.

Single-vesicle content-mixing assay with large DNA cargoes. Inspired by conventional molecular beacons which use a DNA hairpin labeled with a fluorophore and a quencher [26], we designed a DNA hairpin composed of a 5-bp stem and a poly-thymidine loop (T20) labeled with a donor (Cy3) and an acceptor (Cy5) fluorophore at either end of the stem (Figure 1c). When the loop region of this Cy3/Cy5 dual-labeled DNA probe hybridizes with a second DNA strand that has a complementary sequence (A30), the formation of a long double-strand breaks apart the stem region and separates

the donor and the acceptor fluorophores (Figure 1b). The v-SNARE vesicles, with v-SNARE proteins reconstituted in the membrane and the DNA hairpin encapsulated inside, are immobilized on a polymer-coated quartz surface via biotinylated lipids. The t-SNARE vesicles containing t-SNAREs and harboring multiple poly-A DNAs with a cholesterol modification are added together with soluble t-SNAREs. Cholesterol modification increases the incorporation efficiency of poly-A DNA in the t-SNARE vesicle membrane, thus increasing the probability that a fusion event results in the opening of the DNA hairpin. When two vesicles dock and a large enough fusion pore forms between them, the two DNA molecules with a molecular weight of ~10 kDa, which is much larger than the size of normal neurotransmitters, should hybridize, thereby resulting in a change in the FRET efficiency (E).

Equipment setup

TIR fluorescence microscope setup. A schematic illustration of a prism-type TIR fluorescence microscope is shown in Figure 2. The excitation beam is focused onto a Pellin-Broca prism placed on top of a quartz slide with a thin layer of immersion oil. The donor (DiI or Cy3 or SRB)

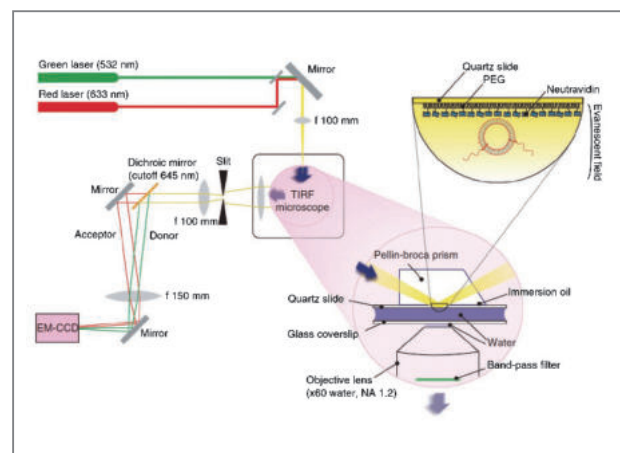


Figure 2. The schematic illustration of a prism-type TIR fluorescence (TIRF) microscopy with both excitation and emission pathways, as well as the TIR occurring at the interface between a quartz slide and water.

and acceptor (DiD or Cy5) dyes are excited by an Nd:YAG laser (532 nm) and a HeNe laser (633 nm), respectively. The emission beam passes through a slit to adjust its total width, and is split to donor and acceptor emission by a 645-nm dichroic mirror and detected simultaneously by the electron-multiplying charge-coupled device camera with a time resolution of 100 ms. Additional details of the wide-field TIR fluorescence microscope setup can be found in our previous review papers [27-29].

Procedure

Vesicle preparation. As summarized in Figure 3, vesicles prepared by both standard and direct methods [30] can be used for the single vesicle-vesicle assay: the composition of the lipid solutions required for the preparation of lipid-mixing vesicles (direct method), the preparation of content-mixing vesicles (direct method) and the preparation of the lipid mixture (standard method). The composition can be changed according to the purpose

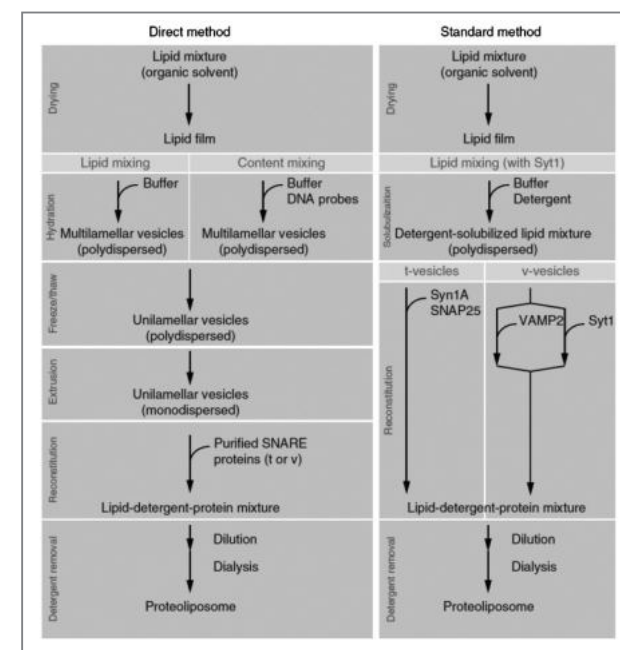


Figure 3. Standard versus direct methods of preparing SNARE-reconstituted vesicles.

of the experiment [15, 22]. Rizo, et al. report the detailed procedures in [11].

Results

Histograms were plotted from FRET signals collected from over one thousand vesicles before and after the fusion reaction. In Figure 4, the y axis shows a normalized population in which we divided the distribution by the total number of vesicles measured, and the x axis is the FRET efficiency (E) value. For lipid mixing (Figure 4a), the nonzero but low E value (open arrow) suggests close contact or docking between the donor and the acceptor vesicles without a high degree of lipid mixing, whereas the

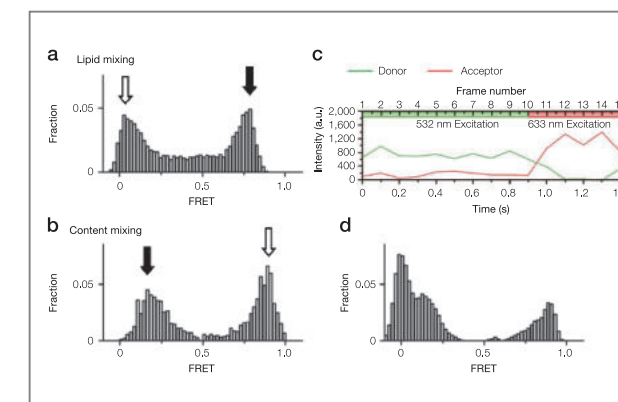


Figure 4. Experimental results. (a) E distribution from a lipid mixing is obtained by continuous 532-nm laser excitation. The y axis is the normalized population and the x axis is E . Open and solid arrows indicate nonfused and fused vesicle populations, respectively. Owing to a background contribution in the acceptor channel from direct excitation, the FRET histogram is plotted on the basis of vesicles identified in the donor channel only. (b) The E distribution from a typical content-mixing assay is obtained from FRET beacon molecules containing both donor (Cy3) and acceptor (Cy5) dyes. Open and solid arrows indicate nonfused and fused vesicle populations, respectively. Unlike the lipid-mixing sample, in which labeling efficiency is ensured by the presence of multiple dyes in the vesicle membranes, some dual-labeled DNA probes may lack one or both dyes. (c) The presence of both dyes may be verified by short (5 frames) exposure of 633-nm illumination followed by 532-nm (10 frames) illumination. (d) With only 532-nm excitation, the E distribution shows an extra donor-only peak at $E = 0$. We selected only those DNA probes with both donor (532-nm excitation) and acceptor (633 nm excitation) fluorescence signals to construct the final histogram (b). a.u., arbitrary units.

high E peak (solid arrow) indicates substantial lipid mixing. For content mixing (Figure 4b), non-fused v-SNARE vesicles with dual-labeled probes in the closed state show a high E value (open arrow). In contrast, a nonzero low E peak (solid arrow) corresponds to the vesicle population with a DNA-hybridized, opened probe induced by content mixing. E distribution of content mixing with the donor-only population subtracted can be obtained through an alternating laser excitation system of 532 and 633 nm (Figure 4c). As shown in Figure 4d, a donor-only peak of zero E appears when we use 532-nm excitation only. As the nonzero low E peak is a positive sign of content mixing, this zero E population complicates data analysis.

A typical single-vesicle lipid-mixing time trace is shown in Figure 5, demonstrating key advantages of our assay; fusion intermediates can be seen directly. Docking of a t-SNARE liposome to a surface-tethered v-SNARE vesicle is observed as an abrupt increase of the donor fluorescence intensity, and the FRET efficiency monotonically increases with increasing lipid mixing (observed as an increase in the acceptor intensity accompanied by an anticorrelated decrease in donor

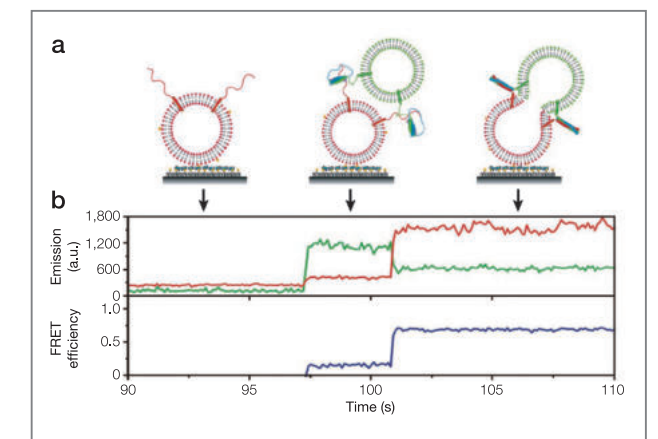


Figure 5. Real-time lipid mixing for lipophilic dyes. (a) Cartoons showing different stages of fusion reaction between a vesicle pair. (b) Fluorescence intensity time traces of the donor (DiI, green) and the acceptor (DiD, red, top) and the corresponding trace of FRET efficiency, E (blue, bottom). No appreciable fluorescence signal change was observed until a t-SNARE liposome docked to a v-SNARE liposome. Rapid lipid mixing between the two vesicles caused by fusion leads to an increase in E . a.u., arbitrary units.

intensity) (Figure 5). Additional docking by another t-SNARE vesicle can be ruled out, as such an event would show a further sharp increase in donor intensity, which was not observed at the low vesicle concentration used (~100 pM). For real-time content mixing of SRB (Figure 6), the v-vesicle encapsulating SRB was docked onto the

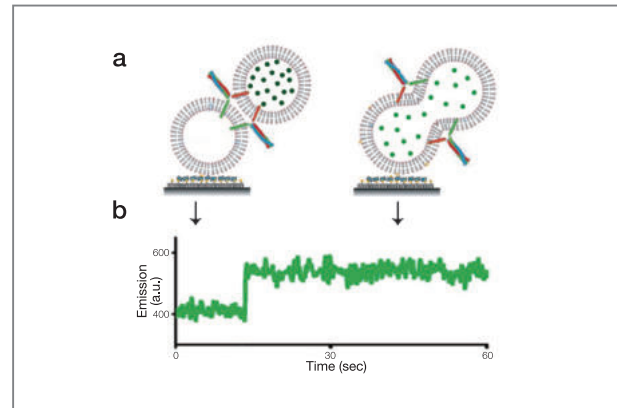


Figure 6. Real-time content mixing of SRB for content labeling only. (a) Different reaction steps of vesicle fusion. Fluorescent dyes of a v-vesicle are initially self-quenched. When a fusion pore opens, the volume of the fused vesicle is increased and the fluorescent dyes are diluted and the signal is dequenched. (b) A real-time content-mixing time trajectory of fluorescence intensities. a.u., arbitrary unit.

empty t-vesicle tethered to the surface. The fluorescence signal of SRB initially showed low intensity. However, when Ca^{2+} was added to the fusion reaction between a v-vesicle with Syt1 and t-vesicle, there was an increase of fluorescence intensity for a single vesicle pair. Also, when the data were accumulated for many vesicle pairs the rate of fusion opening was increased significantly. For real-time content mixing of large DNA cargoes (Figure 7), the vesicle containing unlabeled target DNAs needs to be tethered to the surface. In this scheme, the fluorescence intensity time trace initially showed no FRET. The binding event of a v-vesicle that has the FRET beacon is seen as a sudden appearance of the fluorescence signal with a high E value. When Ca^{2+} was added to the fusion reaction in the presence of Syt1 in the v-vesicle, DNA hybridization caused by content mixing decreases E

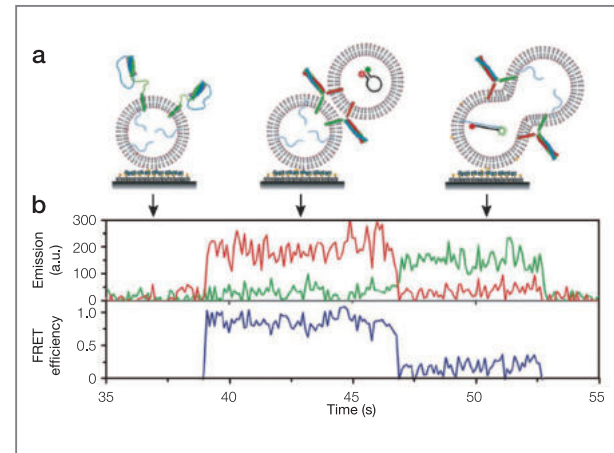


Figure 7. Real-time content mixing of large DNA cargoes for content labeling only. (a) For this real-time experiment, we switched the surface immobilization configuration so that vesicle docking can be clearly marked as an abrupt increase in fluorescence signal. t-vesicles with the target DNAs (poly-A) are surface-immobilized and v-vesicles containing FRET beacons are flowed into the imaging chamber. To eliminate DNA molecules outside vesicles, DNase I treatment was applied before reactions. (b) A real-time content-mixing time trajectory of fluorescence intensities (green curve for Cy3, red curve for Cy5) and the corresponding E (blue curve). a.u., arbitrary unit.

to a lower value, ~0.2. Using the above methods, Shin and co-workers showed that cooperative action of Syt1 and Ca^{2+} is the primary impetus for pore opening and expansion. However, pore expansion is as much as 13 times slower than small pore opening probed with SRB, indicating that pore expansion is the rate-limiting step for full-collapse SNARE-dependent membrane fusion [20]. These results from single-vesicle fusion assays using lipophilic probes, small cargo, and large cargo, paints a more detailed picture than seen before of the regulation of individual fusion steps, including hemifusion, fusion pore formation, and pore expansion by Syt1, Ca^{2+} , and another fusion regulator, complexin 1. It appears that SNAREs alone are sufficient in promoting membrane hemifusion, although Syt1 and Ca^{2+} are required to carry over toward pore formation and expansion. Pore expansion is the late-determining step for the entire membrane fusion process, which might play an important role in allowing the kiss-and-run mechanism for synaptic recycling.

Note

This article and images are cited from “A single vesicle-vesicle fusion assay for *in vitro* studies of SNAREs and accessory proteins” in *Nature Protocol*, Vol. 7 (5), pp. 921-934 and “Fusion pore formation and expansion induced by Ca^{2+} and synaptotagmin 1” in *PNAS*, Vol. 110 (4), pp. 1333-1338.

References

- [1] Zimmerberg, J., S.S. Vogel, et al., *Annu Rev Biophys Biomol Struct.* 1993; 22: 433-66.
- [2] Monck, J.R. and J.M. Fernandez, *Curr Opin Cell Biol.* 1996; 8(4): 524-33.
- [3] Montecucco, C., G. Schiavo, et al., *Trends in Biochemical Sciences* 2005; 30(7): 367-372.
- [4] Jahn, R. and R.H. Scheller, *Nat Rev Mol Cell Biol.* 2006; 7(9): 631-43.
- [5] Weber, T., Zemelman, B. V., et al., *Cell* 1998; 92(6): 759-72.
- [6] Sutton, R.B., Fasshauer, D., et al., *Nature* 1998; 395(6700): 347-53.
- [7] Hanson, P.I., Roth, R., et al., *Cell* 1997; 90(3): 523-35.
- [8] Lin, R.C. and R.H. Scheller, *Annu Rev Cell Dev Biol.* 2000; 16: 19-49.
- [9] Rizo, J. and C. Rosenmund, *Nat Struct Mol Biol.* 2008; 15(7): 665-74.
- [10] Brunger, A.T., Weninger, K., et al., *Annu Rev Biochem.* 2009; 78: 903-28.
- [11] Chen, X.C., Arac, D., et al., *Biophys J.* 2006; 90: 2062-2074.
- [12] Bowen, M.E., Weninger, K., et al., *Biophys J.* 2004; 87: 3569-3584.
- [13] Fix, M., Melia, T. J., et al., *Proc Natl Acad Sci USA.* 2004; 101: 7311-7316.
- [14] Liu, T.T., Tucker, W. C., et al., *Biophys J.* 2005; 89: 2458-2472.
- [15] Yoon, T.Y., Okumus, B., et al., *Proc Natl Acad Sci USA.* 2006; 103: 19731-19736.
- [16] Diao, J.J., Su, Z., et al. *Nat Commun.* 2010; 1.
- [17] Chan, Y.H.M., B. van Lengerich, et al., *Proc Natl Acad Sci USA.* 2009; 106: 979-984.
- [18] Boukobza, E., A. Sonnenfeld, et al., *J Phys Chem B.* 2001; 105: 12165-12170.
- [19] Kyoung, M., Srivastava, A., et al., *Proc Natl Acad Sci USA.* 2011; 108: E304-E313.
- [20] Lai, Y., Diao, J., et al., *Proc Natl Acad Sci USA.* 2013; 110(4): 1333-1338.
- [21] Su, Z.L., Ishitsuka, Y., et al., *Structure* 2008; 16: 1138-1146.
- [22] Yoon, T.Y., Lu, X., et al., *Nat Struct Mol Biol.* 2008; 15: 707-713.
- [23] Diao, J.J., Yoon, T. Y., et al., *Langmuir* 2009; 25: 7177-7180.
- [24] Diao, J.J., Su, J., et al., *ACS Chem Neurosci.* 2010; 1: 168-174.
- [25] Lee, H.K., Yang, Y., et al., *Science* 2010; 328: 760-763.
- [26] Tyagi, S. and F.R. Kramer, *Nat Biotechnol.* 1996; 14: 303-308.
- [27] Joo, C., Balci, H., et al., *Annu Rev Biochem.* 2008; 77: 51-76.
- [28] Roy, R., S. Hohng, et al., *Nat Methods* 2008; 5: 507-516.
- [29] Selvin, P.R.H. and T. Ha, *Single Molecule Techniques: A Laboratory Manual* 2008.
- [30] Diao, J., Ishitsuka, Y., et al., *Nat Protocols* 2012; 7(6): 921-934.

Phosphorescent Nanoparticles for Quantitative Measurements of Oxygen Profiles *In Vitro* and *In Vivo*



Nak Won Choi, Ph.D.
Center for BioMicrosystems,
Brain Science Institute
nakwon.choi@kist.re.kr

Introduction

Spatiotemporal variation of the concentration of oxygen in tissue plays a central role in regulating biological processes, including embryonic, vascular and bone development, as well as stem cell function and wound healing. Diseases that involve these processes, such as cancer, are also strongly regulated by the distribution and concentration of oxygen in tissue [1, 2]. Tools to measure profiles of oxygen with micrometer-scale resolution in three-dimensional (3-D) systems could help improve basic understanding of the role of oxygen in a range of both physiological and pathological processes; to date, few such tools are available. In this feature article, we present the development and characterization of nanoparticles loaded with a custom phosphor; we exploited these nanoparticles to perform quantitative measurements of the concentration of oxygen within 3-D tissue cultures *in vitro* and blood vessels *in vivo*. We synthesized a customized ruthenium (Ru)-phosphor and incorporated it into polymeric nanoparticles via self-assembly. We demonstrated that the encapsulated phosphor is non-toxic with and without illumination. We evaluated two distinct modes of employing the phosphorescent nanoparticles for the measurement of concentrations of oxygen: 1) *in vitro*, in a 3-D microfluidic tumor model via ratiometric measurements of intensity with an oxygen-insensitive fluorophore as a reference; and 2) *in vivo*, in mouse vasculature using measurements of phosphorescence lifetime. With both methods, we demonstrated

micrometer-scale resolution and absolute calibration to the dissolved oxygen concentration. Based on the ease and customizability of the synthesis of the nanoparticles and the flexibility of their application, these oxygen-sensing polymeric nanoparticles are expected to find a natural home in a range of biological applications, benefiting studies of physiological as well as pathological processes in which oxygen availability and concentration play a critical role.

Quantification of oxygen concentration from optical measurements

The concentration of oxygen was extracted from optical measurements (i.e., intensity or lifetime) using the Stern-Volmer relationship. Assuming that quenching is

the only process that affects the luminescence decay of the phosphor, the ratio between the luminescence lifetime (or integrated luminescence intensity) in the absence and presence of quenching molecules (oxygen molecules in this study) is linearly proportional to the concentration of the quencher: $\tau_0/\tau = I_{phos,0}/I_{phos} = 1 + K_{SV}c_{O_2}$ where τ [s] is phosphorescence lifetime. The subscript 0 denotes the absence of oxygen. I_{phos} is phosphorescence intensity, K_{SV} [M⁻¹] is the Stern-Volmer constant or oxygen sensitivity, and c_{O_2} [M] is the concentration of dissolved oxygen.

Synthesis and size characterization of oxygen-sensing nanoparticles

Amphiphilic reactive oligomers, urethane acrylate nonionmer (UAN) [3, 4] chains are composed of a

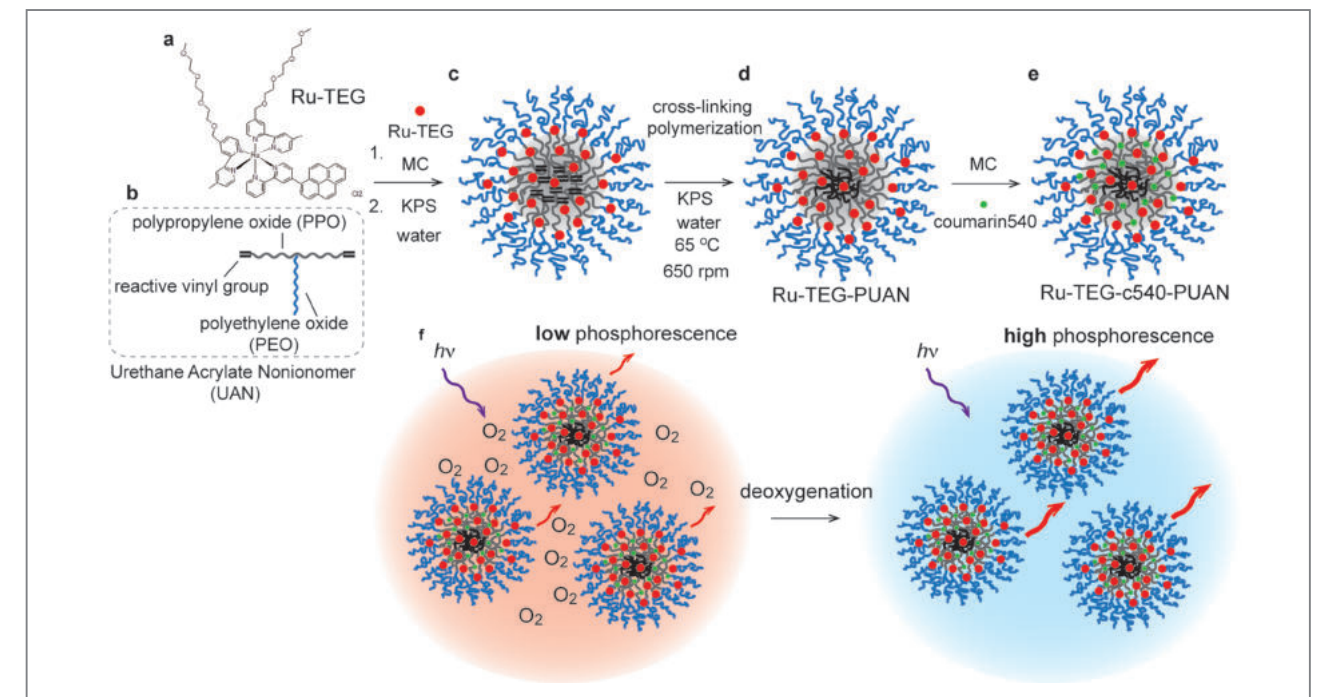


Figure 1. Schematic illustration representing synthesis of oxygen-sensing nanoparticles. (a) Chemical structure of oxygen-sensitive phosphor, [(TEG-bpy)₂Ru(bpy-pyr)]Cl₂ (Ru-TEG). (b) Amphiphilic reactive oligomer, urethane acrylate nonionmer (UAN) consisting of hydrophilic polyethylene oxide segment (PEO; blue) and hydrophobic polypropylene oxide segment (PPO, gray) with reactive vinyl groups (black). (c) UAN nanoparticle loaded with Ru-TEG (red circle). (d) Ru-TEG-PUAN nanoparticle synthesized via chemical cross-linking polymerization. (e) Ru-TEG-PUAN nanoparticle with a post-incorporated reference fluorophore, coumarin540 (c540; green circle). (f) Schematic representation of principle of oxygen imaging. Purple arrows represent incident excitation light. Red arrow represents phosphorescence emission from Ru-TEG in the presence (left) and absence (right) of oxygen molecules.

hydrophilic PEO segment and a hydrophobic PPO segment that are covalently connected via urethane linkage (Figure 1b). On mixing with water, UAN chains form micelle-like nanoparticles via self-assembly due to intermolecular hydrophobic interaction (Figure 1c). Through the formation of micelle-like UAN nanoparticles in water, PEG segments oriented toward the water phase form a hydrophilic shell whereas PPO segments and their vinyl groups form a hydrophobic core. The chemical cross-linking polymerization takes place only between vinyl groups in the hydrophobic core within UAN nanoparticles, and allows for a permanent lock-in of their micelle-like nanostructure; this transformation converts UAN nanoparticles to core-cross-linked polymeric nanoparticles (Figure 1d). An oxygen-sensitive phosphor, $[(\text{TEG-bpy})_2\text{Ru}(\text{bpy-pyr})]\text{Cl}_2$ (Ru-TEG), was first

partitioned in UAN by dissolving in methylene chloride (MC). After allowing for the evaporation of MC, the UAN partitioned with Ru-TEG was mixed with a solution of potassium persulfate (KPS; radical initiator) dissolved in deionized (DI) water, thereby dispersing nanoparticles in water (Figure 1c). Coumarin540 (c540; Exciton) as a reference fluorophore was post-incorporated after cross-linking the Ru-TEG-PUAN particles. Ru-TEG-c540-PUAN nanoparticles are dispersed well in water and can be stored at room temperature prior to use. Average diameters of Ru-TEG-PUAN and Ru-TEG-c540-PUAN were 41.50 ± 0.799 and 41.53 ± 0.755 nm with a polydispersity index (PDI) of 0.120 ± 0.009 and 0.109 ± 0.010 , respectively, as measured by DLS. We also verified that the luminophores remained stably incorporated within PUAN for several months.

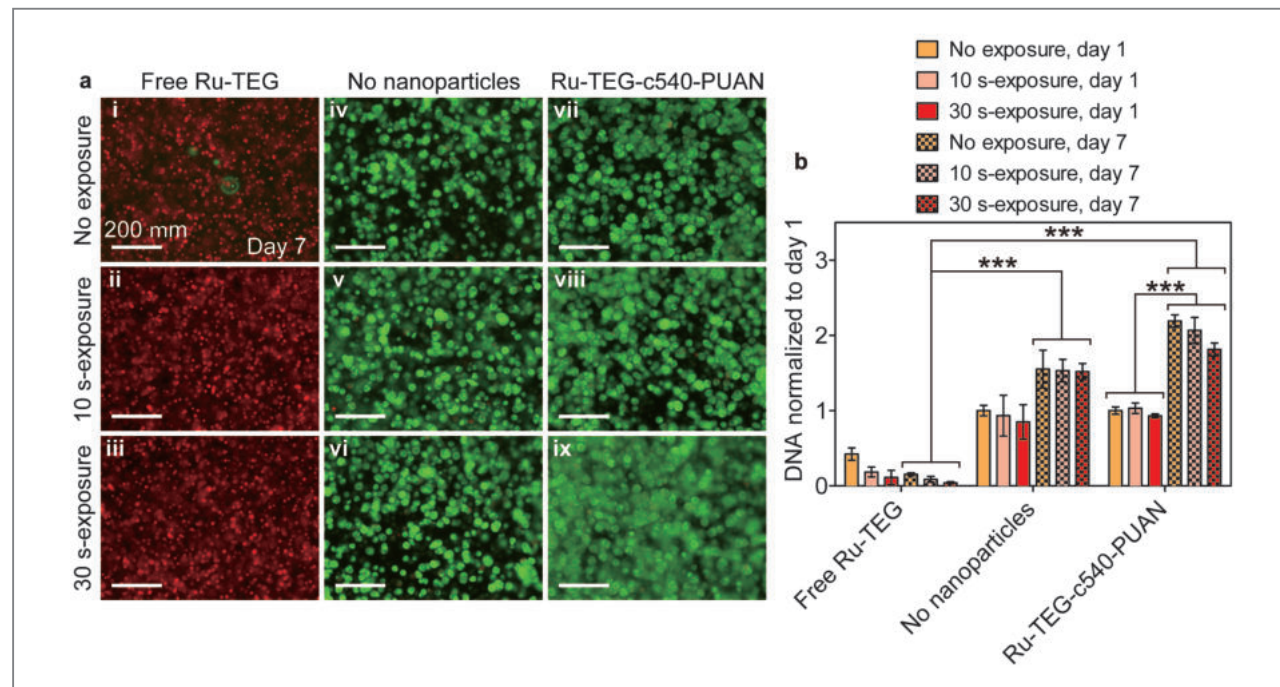


Figure 2. Biocompatibility of oxygen-sensing nanoparticles. (a) Fluorescence micrographs showing cells stained by 5 μM calcein-AM (green - live) and 5 μM ethidium homodimer-1 (red - dead) after 7 days of culture of OSCC-3s seeded in 4% [w/v] calcium alginate discs (200 μm -thick). (b) DNA content per alginate disc, normalized to day 1-DNA amount without exposure. Images and grouped bar graphs from left to right correspond to: free Ru-TEG dissolved in culture media, no oxygen-sensing nanoparticles dispersed in OSCC-3-seeded alginate discs, and Ru-TEG-c540-PUAN nanoparticles dispersed in alginate discs. Images from top to bottom and bar graphs within each group from left to right represent no exposure to excitation light (392 nm), 10 s-exposure, and 30 s-exposure per day. Bar graphs with black squares inside represent normalized DNA content on day 7. Error bars represent standard deviation of mean. Statistical significance *** represents $p < 0.001$.

Biocompatibility of oxygen-sensing nanoparticles

Oxygen-sensitive phosphors (typically metal-ligand complexes) can be highly toxic to cells because they are small amphiphilic molecules that are home to cellular lipid bilayers. To evaluate the toxicity of Ru-TEG, we cultured oral squamous cell carcinoma cells (OSCC-3; received as a gift from Peter Polverini, University of Michigan) in 200 μm -thick alginate discs (4 mm in diameter) in contact with either freely dissolved or nanoparticle-encapsulated phosphor. We observed that the culture of OSCC-3s in media containing free Ru-TEG resulted in significant cell death; both live-dead staining and DNA quantification showed significant cellular death as early as the first day of culture; by day 7, viability was less than 25% even in the absence of exposure to the excitation light (Figure 2a i-iii and 2b). The significant cell death with free Ru-TEG indicates that Ru-TEG presents direct toxicity to the cells. In contrast, OSCC-3s cultured within discs with phosphor encapsulated in nanoparticles showed high cell viability similar to those within control discs (i.e., no Ru-TEG-c540 nanoparticles within discs), by both live-dead staining (Figure 2a iv-ix) and DNA quantification (Figure 2b) out to 7 days of culture. Overall, these results demonstrate that encapsulation of phosphors within nanoparticles eliminates the toxicity of these luminophores. *In vivo*, we also observed that mice injected with oxygen-sensing nanoparticles (i.e., Ru-TEG-PUAN) did not show any immediate (acute) toxicity. We therefore conclude that encapsulation of Ru-TEG within PUAN nanoparticles is effective in eliminating the toxicity of the free phosphor.

Evaluation of both direct phosphorescence and ratiometric approaches for optically measuring oxygen depletion

To characterize oxygen imaging based on direct phosphorescence intensity, I_{phos} and normalized intensity, \bar{I}

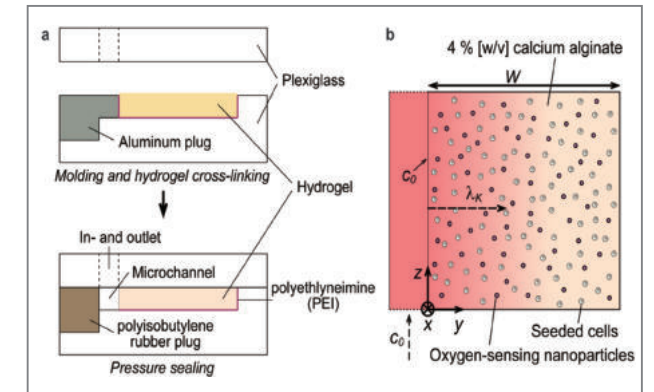


Figure 3. Fabrication of 1-channel microfluidic system for visualization and optical measurement of oxygen-depletion lengths (Krogh lengths). (a) Schematic diagram showing the fabrication of microfluidic system. The red line indicates polyethyleneimine (PEI) coating. (b) Schematic representation of oxygen-sensing microfluidic scaffold seeded with cells (top-down view). Dispersed cells are depicted as double circles and oxygen-sensing nanoparticles as red circles. The pink shading represents steady-state distribution of oxygen within the cell-seeded scaffold. W is width of the scaffold. The Krogh length, λ_K , is the characteristic distance over which oxygen diffuses into the scaffold from the microchannel. c_0 is oxygen concentration at the microchannel-scaffold interface.

($= I_{\text{phos}} / I_{\text{fluor}}$) with PUAN nanoparticles, we focused on the depletion of oxygen due to the metabolic activity of tumor cells in 3-D scaffolds. Figure 3 presents the fabrication and geometry of our oxygen-sensing microfluidic scaffold: a 500 μm -thick slab of alginate (4 mm \times 4 mm) seeded with OSCC-3 was sealed within a plexiglass jig such that one edge was adjacent to a single microchannel. Media delivered through the channel were the sole source of oxygen in this system, such that a steady-state oxygen profile could be reached in which diffusion from the channel balanced cellular consumption within the bulk. \bar{I} was calibrated by delivering media maintained at controlled oxygen levels (Figure 4a). We attained a master calibration curve and used this master curve to convert the ratio of intensities, \bar{I} to the concentration of dissolved oxygen, c_{O_2} with $\bar{I}_0 / \bar{I} = 1 + K_{\text{SV}}^{\bar{I}} c_{\text{O}_2}$. From the Stern-Volmer plot (Figure 4b), the estimated $K_{\text{SV}}^{\bar{I}}$ (i.e., slope of the black solid line; oxygen sensitivity of Ru-TEG) was $(4.056 \pm 0.55) \times 10^{-3} \mu\text{M}^{-1}$. Wide-field luminescence images were taken using both Ru-TEG and c540 emission channels.

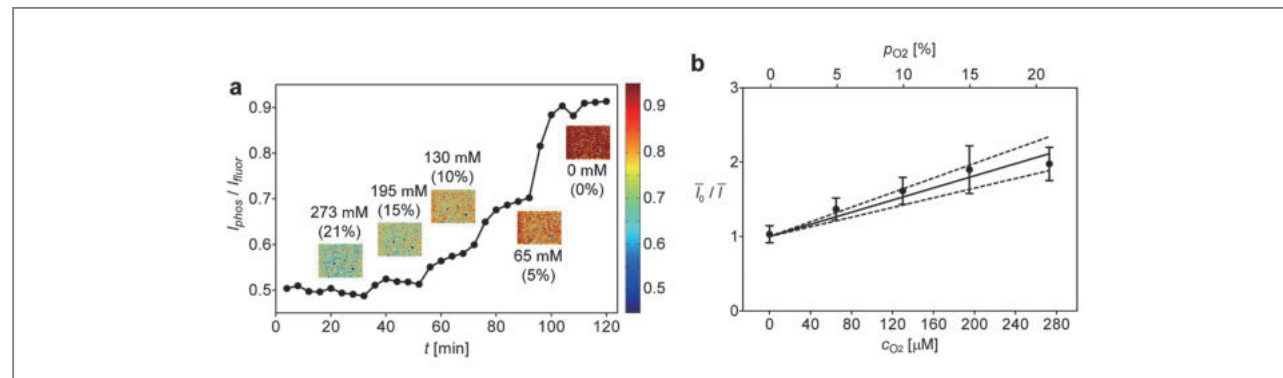


Figure 4. Intensity-based calibration of oxygen-sensing nanoparticles. (a) Representative transient profiles of luminescence intensity during intensity-based calibration. The ratio of phosphorescence and fluorescence intensities (i.e., $\bar{I} = I_{phos} / I_{fluor}$) calculated as oxygen concentration was incrementally decreased from ambient (0 min) to deoxygenated (120 min) states. The insets present color-mapped micrographs of \bar{I} from an OSCC-3-seeded scaffold (2×10^7 cell/mL) equilibrated at various concentrations of oxygen. (b) Stern-Volmer plot obtained from the intensity-based calibration with cell-seeded scaffolds: 3 scaffolds at 5×10^6 cell/mL and 3 scaffolds at 2×10^7 cell/mL. Black circles are the mean values \bar{I}_0 / \bar{I} , and error bars are uncertainties. The solid lines are linear regressions weighted by uncertainties (standard deviation of residuals, $S_{yx} = 0.1011$ (d)), and gray dotted lines represent 95% confidence interval for the linear regressions.

The micrographs in Figure 5a show representative phosphorescence intensity with background subtracted (I_{phos}) as a color map for two different seeding densities, 5×10^6 (left; Figure 5a i) and 2×10^7 cell/mL (right; Figure 5a ii), 45 min after the initiation of flow through the channel. The variation of I_{phos} represents the variation in the concentration of oxygen, from the ambient oxygen source (left; red) towards hypoxic bulk (right; blue). As expected, the spatial variation of $I_{phos}(y)$ was more rapid for the higher density of cells (Figure 5c). Figure 5d presents the actual distribution of oxygen concentration within the scaffolds, $c_{O_2}(y)$ calculated with the Stern-Volmer equation from the profile of ratiometric intensity. The solid lines (dark red and dark blue) in Figure 5d present the calculated profiles based on the assumption of Michaelis-Menten kinetics in which we used a single value of $K_M = 12.3 \mu\text{M}$. Our predicted K_M implies that it is generally appropriate to assume zeroth-order consumption kinetics under typical cell culture conditions. This agreement indicates that, with our ratiometric approach, the Ru-TEG nanoparticles can provide quantitative measurements of the spatial distribution of oxygen within a 3-D culture via direct imaging. Oxygen heterogeneity will inevitably impact cellular behavior [2, 5], and such behavior would have

obvious implications for tumor progression, as temporal variations in hypoxia are thought to be associated with development of a more aggressive and therapy-resistant tumor type. Furthermore, as 3-D culture platforms become more ubiquitous, it is becoming more important to have flexible techniques for the measurement of oxygen levels that are often variable throughout the bulk of these systems. Optical measurement with our encapsulated nanoparticle sensors provides one practical solution, enabling online measurement of oxygen level with high spatial as well as temporal resolution.

In vivo oxygen imaging of mouse vasculature

We also employed our oxygen-sensing nanoparticles for the quantitative measurement of oxygen concentration in mouse vasculature (Figure 6). We pursued lifetime measurements with multiphoton microscopy for *in vivo* oxygen measurements since lifetime is known to be independent of artifacts such as optical scattering and luminophore concentration [6]. Figure 6a shows the lifetime-based Stern-Volmer plot for Ru-TEG-PUAN

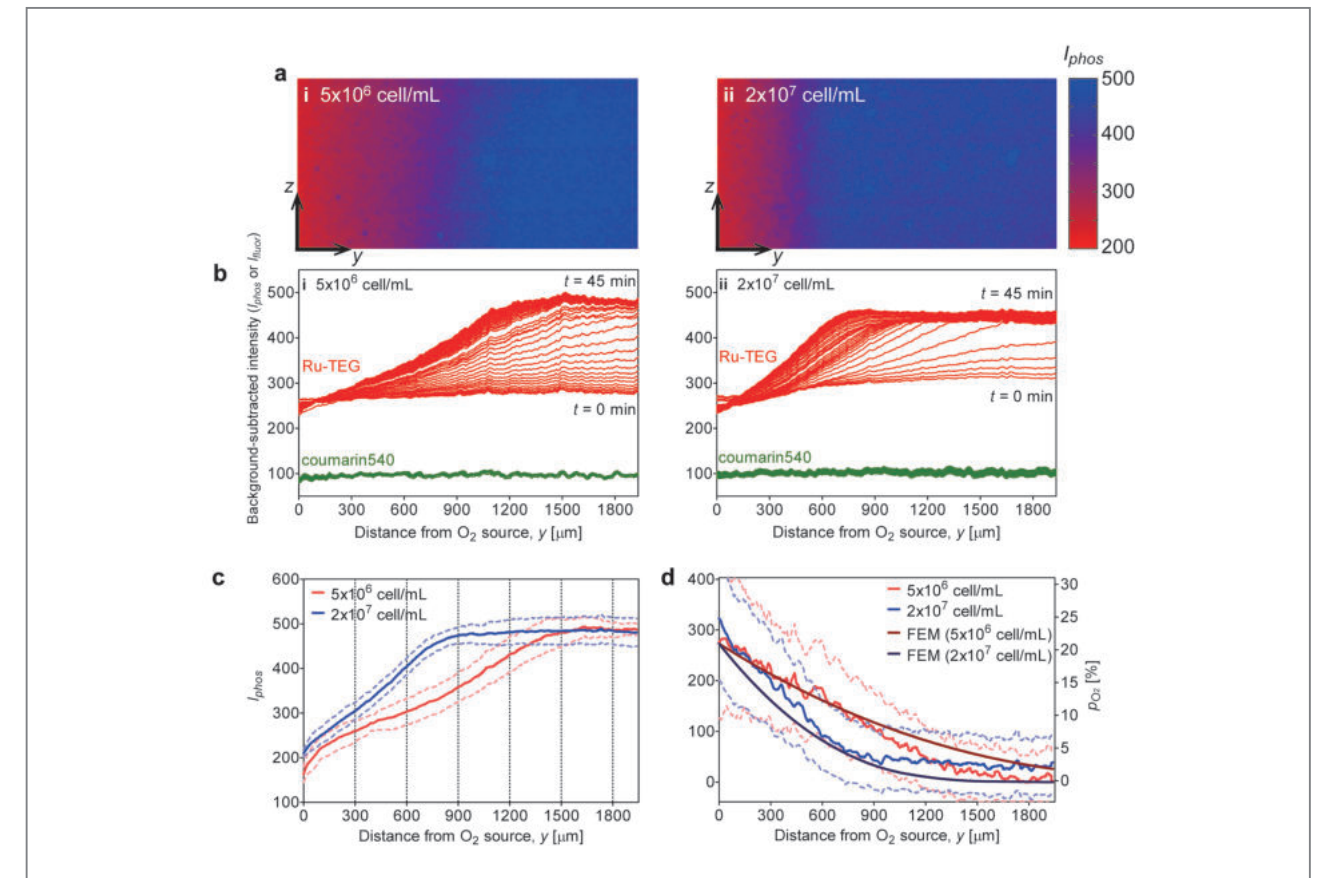


Figure 5. Visualization and quantification of oxygen-depletion in microfluidic tumor model. (a) Phosphorescence micrographs of alginate scaffolds seeded with Ru-TEG nanoparticles and OSCC-3 cells at 5×10^6 cell/mL (frame i) and 2×10^7 cell/mL (frame ii). The color-maps show phosphorescence intensity from which the background intensity was subtracted pixel-by-pixel (also see Section 2.11 in Materials and Methods). Red and blue represent ambient and hypoxic oxygen levels respectively. (b) Transient profiles along y -direction of images as in (a). Red lines represent phosphorescence from Ru-TEG with background subtracted (I_{phos}); green lines represent fluorescence of the Coumarin 540 reference (I_{fluor}). The profiles were extracted from frames taken every minute out to 45 min. (c) Profile of I_{phos} along y -direction at 45 min for 5×10^6 cell/mL (red) and 2×10^7 cell/mL (blue). Dash lines represent standard deviation of I_{phos} from three replicates for each cell seeding density. (d) Spatially resolved distributions of oxygen concentration. Red and blue represent cell seeding densities of 5×10^6 cell/mL and 2×10^7 cell/mL, respectively. Solid and dash lines are $c_{O_2}(y)$ and estimated uncertainty, from three replicates for each cell seeding density. Dark red and dark blue solid lines in (b) are computationally calculated oxygen concentration in a finite element model with an assumption of Michaelis-Menten kinetics: $D_{O_2} = 2.76 \times 10^{-9} \text{m}^2/\text{s}$, $c_0 = 273 \mu\text{M}$, $V_{m,cell} = 5.4 \times 10^{-17} \text{mol/s} \cdot \text{cell}$, $K_M = 12.3 \mu\text{M}$, $\rho_{cell} = 5 \times 10^6 \text{cell/mL}$ (dark red) and $2 \times 10^7 \text{cell/mL}$ (dark blue). In these calculations, concentration boundary conditions were maintained at the channel walls ($c_{y=0} = c_0$), and no-flux conditions were maintained at other boundaries.

nanoparticles dispersed in water equilibrated at various concentrations of oxygen ($K_{SV}^T = (5.18 \pm 0.24) \times 10^{-3} \mu\text{M}^{-1}$). Phosphorescence lifetime values of Ru-TEG in the saphenous artery (red) and vein (blue), estimated from the single-exponential fit (solid curves in Figure 6e), were 4.73 and 13.4 μs for artery and vein, respectively. Our *in vivo* measurements demonstrate that these nanoparticles can be used to provide reproducible, three-dimensionally

resolved oxygen measurements at capillary spatial scales. Based on their small size, the nanoparticles we present also could enable tissue oxygen imaging in biological systems with leaky vasculature, such as tumors or tissues where extensive matrix remodeling occurs. Direct injection of nanoparticles, local Mannitol administration [7] for temporarily permeabilizing vasculature, or functionalization of the PUAN nanoparticles with homing peptides

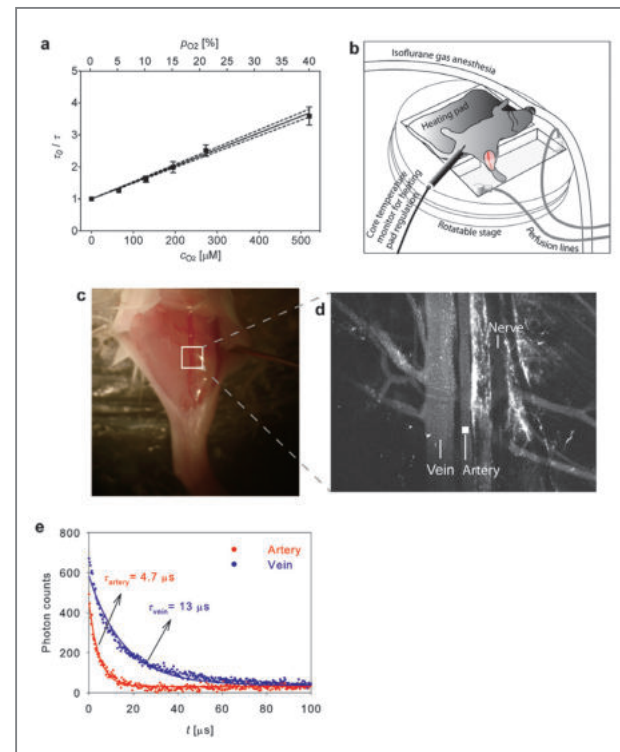


Figure 6. Lifetime-based quantification of oxygen concentration *in vivo*. (a) Stern-Volmer plot based on phosphorescence lifetime of for Ru-TEG-PUAN nanoparticles dispersed in water. Black squares are the mean values of τ_0/τ , and error bars are standard deviation (multiple measurements at each c_{O_2} were used from two independent calibration experiments). The solid line is a linear regression (standard deviation of residuals, $S_{y,x} = 0.1622$), and gray dotted lines represent 95% confidence interval for the linear regression. (b) Schematic of *in vivo* oxygen imaging platform. (c) Mouse saphenous vasculature, exposed by an incision through the skin, leaving the fascia intact. (d) Multiphoton image of saphenous vessels from the region of interest (highlighted in c; white square) after intracardiac injection of oxygen-sensing nanoparticles. (e) Phosphorescence lifetime decay of Ru-TEG-PUAN nanoparticles in saphenous artery (red dots) and vein (blue dots). Solid lines in red and blue are single-exponential decay curves fit to the experimental data points.

could provide alternative avenues of delivery to tissues of interest. Potential future advantages could include tunability of size, hydrophilic/hydrophobic balance, and functionality of nanoparticles via changes in PEG or PPO chain length or chemical modifications of UAN chains. Furthermore, the potential tunability of these oxygen sensors could lead to the development of multi-purpose nanoparticles, one example being oxygen-pH sensing.

Conclusions

We have presented a new set of tools to quantify the concentration of dissolved oxygen for applications both *in vitro* and *in vivo*, by encapsulating a specially designed Ru-based phosphor within PUAN nanoparticles. The phosphor represents an improvement over widely used chemistries with respect to sensitivity to oxygen concentration ($5.2 \times 10^{-3} \mu M^{-1}$). The UAN amphiphilic reactive oligomer offers a number of advantages as a nano-vehicle over amphiphilic block copolymers, surfactant micelles, and dendrimers, including: 1) simple self-assembly driven synthesis; and 2) high stability and long term incorporation of phosphors due to chemical cross-linking of hydrophobic cores. We have used these nanoparticles to demonstrate non-invasive and real-time measurements of oxygen gradients occurring due to cellular consumption in a 3-D cell culture platform, as well as *in vivo* oxygen levels in mouse vasculature. We anticipate that the versatility of the materials and techniques we present will lead to the adoption of similar approaches for online oxygen measurement in a range of experimental systems.

Note

This article and images are cited from “Phosphorescent nanoparticles for quantitative measurements of oxygen profiles *in vitro* and *in vivo*” in *Biomaterials*, Vol. 33, pp. 2710-2722.

References

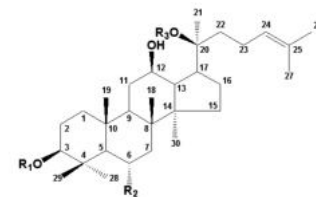
- [1] Harris AL. *Nat. Rev. Cancer* 2002; 2 (1): 38-47.
- [2] Verbridge SS, Choi NW et al. *Tissue Eng Part A* 2010; 16 (7): 2133-2141.
- [3] Kim JY, Shim SB. *J. Ind. Eng. Chem.* 2002; 8 (3): 225-235.
- [4] Kim JY, Shin DH et al. *Macromol. Chem. Phys.* 2002; 203 (17): 2454-2462.

- [5] Fischbach C, Chen R et al. *Nat. Methods* 2007; 4 (10): 855-860.
- [6] Rodriguez JCC, Garcia MAP et al. *IEEE Trans. Instrum. Meas.* 1999; 48 (5): 949-955.
- [7] Sugahara KN, Teesalu T et al. *Cancer Cell* 2009; 16 (6): 510-520.

Increase in Antioxidant and Anticancer Effects of Ginsenoside by Maillard Reaction

Introduction

The root of ginseng, *Panax ginseng* C.A. Meyer (Araliaceae), has traditionally been used as a functional food as well as a herbal medicine in Asia. Unlike other plants, *Panax* species plants contain dammarane-based saponin in common with 1 to 4 saccharides combined to a dammarane backbone. The saponins contained at high concentrations in ginseng include ginsenosides Rb₁, Rb₂, Rc, Rd and Re (Figure 1) [1]. These saponins have a variety of efficacies that vary significantly in terms of type and intensity depending on their structures.



Rb₁ : R₁ = Glc(2←1)Glc, R₂ = H, R₃ = Glc(6←1)Glc
Rb₂ : R₁ = Glc(2←1)Glc, R₂ = H, R₃ = Glc(6←1)Ara(p)
Rc : R₁ = Glc(2←1)Glc, R₂ = H, R₃ = Glc(6←1)Ara(f)
Rd : R₁ = Glc(2←1)Glc, R₂ = H, R₃ = Glc
Re : R₁ = H, R₂ = O-Glc(2←1)Rha, R₃ = Glc

Figure 1. Structures of ginsenosides. -Glc: D-glucopyranosyl, -Rha: L-rhamnopyranosyl, -Ara(f): L-arabinofuranosyl, -Ara(p): L-arabinopyranosyl.



Ki Sung Kang
 Natural Medicine Center
 kkang@kist.re.kr

Panax ginseng is harvested after four to six years of cultivation and is classified into three types depending on how it is processed. Fresh ginseng can be consumed in an unprocessed state. White ginseng is dried ginseng root, and red ginseng is ginseng root steamed at 98–100°C (Figure 2). Red ginseng is more commonly used than white ginseng as a medicinal herb in Asian countries because steaming induces changes in the chemical constituents and enhances the biological activities of ginseng [1,2]. A novel heat-processing method of autoclaving ginseng at a higher temperature than red ginseng was recently developed to achieve an even stronger activity than that of red ginseng, and this ginseng product is referred to as heat-processed ginseng (Figure 2) [3]. Our research group as well as others have reported that heat-processed ginseng exhibits more potent pharmacological effects than conventional white or red ginseng, including antioxidant, vasorelaxation, anxiolytic-like, and antitumor activities, [3–5].

Maillard reaction products (MRPs) are generated whenever reducing sugars are heated in the presence of amino acids, peptides, or proteins, which mainly occurs during the heat-processing of foods, and it is also known as a major class of compounds with enhanced biological activity generated by thermal treatment of various crude

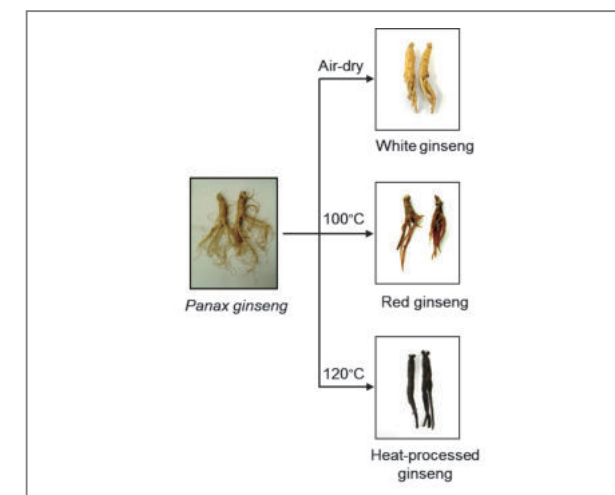


Figure 2. Classification of *Panax ginseng* products by heat-processing methods.

drugs. However, little is known about the structural and biological activity changes in ginsenosides upon Maillard reaction. The focus of this article is on KIST's efforts in identifying the active components of heat-processed *Panax ginseng* by investigating the chemical changes in structures of ginsenosides by Maillard reaction and their antioxidant and anticancer activities.

Maillard reaction of ginsenosides

To demonstrate the Maillard reaction of ginsenosides, ginsenoside Re, a well-known triol-type triterpene

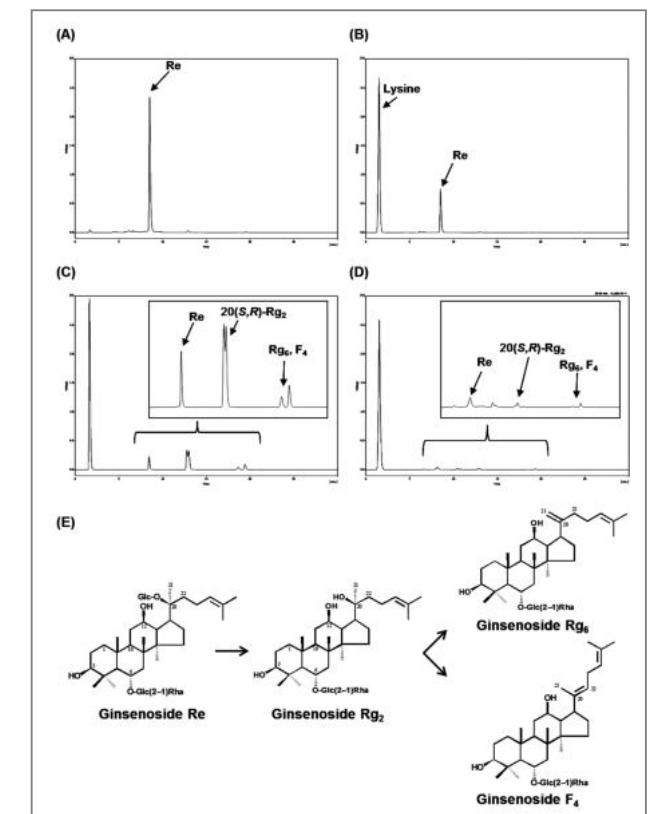


Figure 3. Changes in HPLC chromatograms of ginsenoside Re and ginsenoside Re-lysine mixtures by heat processing. (a) HPLC chromatogram of ginsenoside Re before heat processing. (b) HPLC chromatogram of ginsenoside Re-lysine mixture before heat processing. (c) HPLC chromatogram of ginsenoside Re after heat processing. (d) HPLC chromatogram of ginsenoside Re-lysine mixture after heat processing. (e) Changes in chemical structure of ginsenoside Re during heat-processing.

glycoside that exists abundantly in *Panax ginseng*, was steamed with lysine, a frequently used amino acid in the Maillard reaction model system and also contained in ginseng. As shown in the HPLC chromatograms of the ginsenoside Re and ginsenoside Re-lysine mixture, most of the ginsenoside Re disappeared and the contents of less-polar ginsenosides were newly detected upon heat-processing at 120°C (Figure 3). Ginsenoside Rg₂ was generated by elimination of the glycosyl residue at carbon-20 during the steaming process, and greater amounts of less-polar ginsenosides such as Rg₆ and F₄ were produced by the elimination of H₂O at carbon-20 of ginsenoside Rg₂ under high pressure and temperature conditions [6].

The generation of color is an obvious feature of Maillard reaction. The level of browning products in ginsenoside Re and ginsenoside Re-lysine mixture increased after heat-processing at 120°C (Figure 4). In the case of the glucose-lysine mixture, the level of browning products increased to 6.1 times higher than the value of the ginsenoside Re-lysine mixture. Therefore, MRPs were generated after the heat-processing of ginsenoside Re,

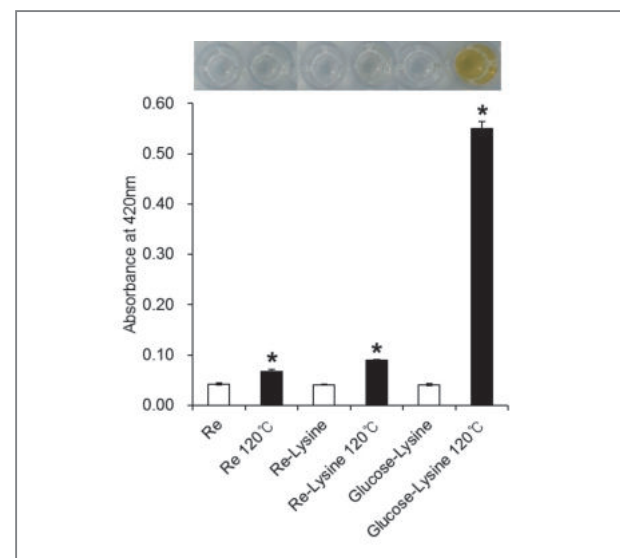


Figure 4. Changes in browning compound levels of ginsenoside Re, ginsenoside Re-lysine and glucose-lysine mixtures by heat-processing. (a) The level of browning products. (b) The level of advanced MRPs. * $p < 0.05$ compared to the not-treated value.

ginsenoside Re-lysine and glucose-lysine mixtures [6].

Increase in antioxidant activity of ginsenoside by Maillard reaction

No significant antioxidant effect of ginsenoside Re,

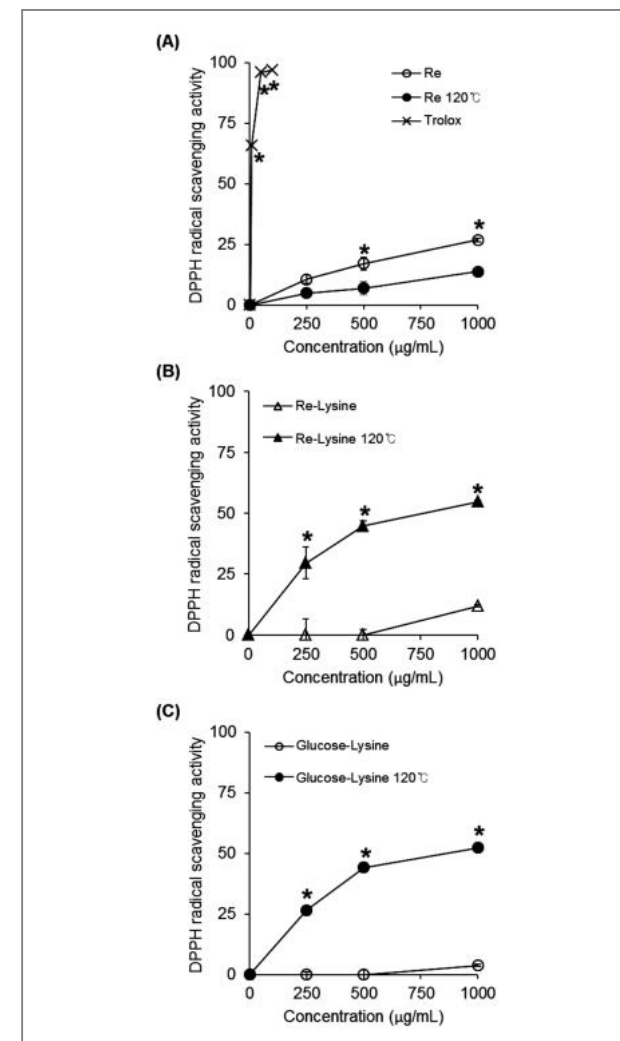


Figure 5. Changes in DPPH radical-scavenging activities of ginsenoside Re, ginsenoside Re-lysine and glucose-lysine mixtures by heat-processing. (a) Comparison of DPPH radical-scavenging activity of ginsenoside Re upon heat processing. (b) Comparison of DPPH radical-scavenging activity of ginsenoside Re-lysine mixture upon heat processing. (c) Comparison of DPPH radical-scavenging activity of glucose-lysine mixture upon heat processing. * $p < 0.05$ compared to the not-treated value.

measured by a DPPH radical-scavenging activity test, was confirmed, but its activity increased slightly after heat-processing (Figure 5(a)). The ginsenoside Re-lysine mixture showed weak antioxidant activity, but its effect increased markedly after heat-processing at 120°C (Figure 5(b)). The glucose-lysine mixture demonstrated no DPPH radical-scavenging activity, but its effect significantly increased after heat-processing at 120°C (Figure 5(c)). The scavenging activity of various MRPs against reactive oxygen species such as DPPH, hydroxyl radical and superoxide anion, in cell-free and cell-culture systems has been extensively discussed [7]. In light of these findings, a comparison of DPPH radical-scavenging activities of ginsenoside Re and its MRPs suggests that the increased free radical-scavenging activity of the ginsenoside Re-lysine mixture upon heat-processing was mainly mediated by the MRPs from glucose and lysine [6].

Increase in anticancer activity of ginsenoside by Maillard reaction

Many researchers have discussed the anticancer activity of antioxidants [8]. Ginsenoside Re-lysine mixture was also found to suppress human stomach cancer AGS cell proliferation upon heat-processing in a dose-dependent manner (Figure 6). The loss of cell proliferation following treatment of ginsenoside Re-lysine mixture without heat-processing was not observed. Next, we sought to determine whether the antiproliferating effect of ginsenoside Re-lysine mixture is due to the ginsenoside Re or antioxidant MRPs. Our results showed a strong antiproliferating activity with the treatment of ginsenoside Re upon heat-processing. The MRPs from the glucose and lysine mixture showed significant suppression, but less activity, compared to that of ginsenoside Re upon heat-processing (Figure 6(c)). Therefore, the antiproliferating efficacy of ginsenoside Re-lysine upon heat-processing was mainly derived from less-polar ginsenosides such as Rg₂, Rg₆ and F₄ (Figure

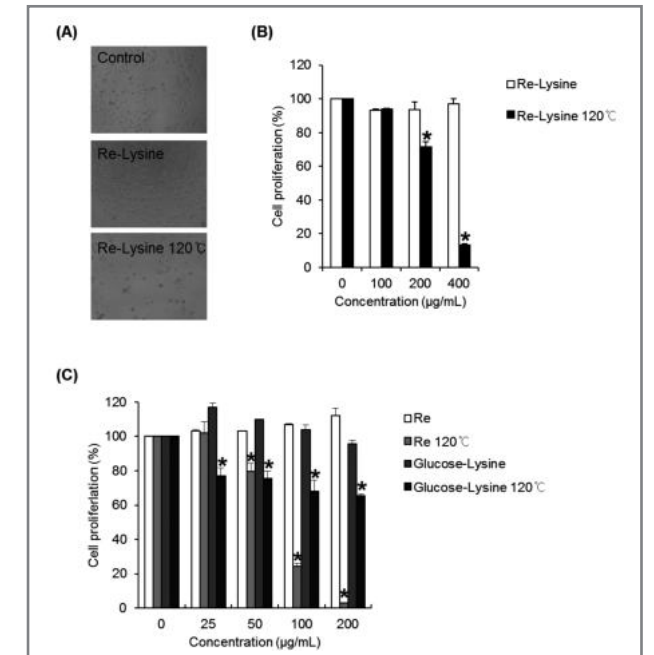


Figure 6. Changes in effects of ginsenoside Re-lysine, ginsenoside Re and glucose-lysine mixtures upon heat processing on AGS cell proliferation. (a) Morphological changes were confirmed using phase-contrast microscopy. (b) Cells were treated with ginsenoside Re-lysine mixture with or without heat processing at different concentrations (100, 200, and 400 µg/mL) for 24 h. (c) Cells were treated with ginsenoside Re or glucose-lysine mixture with or without heat processing, respectively, at different concentrations (25, 50, 100, and 200 µg/mL) for 24 h. Relative cell proliferation was measured by the CCK-8 assay. * $p < 0.05$ compared to the not-treated value.

2), suggesting that this efficacy was not related to the antioxidant activity.

Since apoptosis is a mechanism by which cells die to control cell proliferation, and heat processed-ginsenoside Re possessed a strong antiproliferating effect on AGS cells, we also confirmed the molecular mechanisms of apoptotic effects by Western blotting. As shown in Figure 7, examination of Bax and Bcl-2 expression during apoptosis indicated that treatments with heat processed-ginsenoside Re dose-dependently up-regulated the expression of pro-apoptotic protein Bax, whereas the expression of anti-apoptotic protein Bcl-2 was down-regulated with an increasing concentration of heat processed-ginsenoside Re at 120°C. Caspases, which are cysteine proteases, play pivotal roles in cell

apoptosis. Caspase-3 is an apoptosis executioner and is activated by other activated caspases, such as caspase-8 and caspase-9, in response to pro-apoptotic signals [9]. We demonstrated that active forms (cleaved forms) of caspase-8, caspase-9, and caspase-3 were up-regulated in a dose-dependent manner after treatment of heat processed-ginsenoside Re at 120°C (Figure 7). Subsequently, PARP, a well-known substrate of caspase-3, was cleaved by the activated caspase-3, resulting in AGS cell apoptosis (Figure 7).

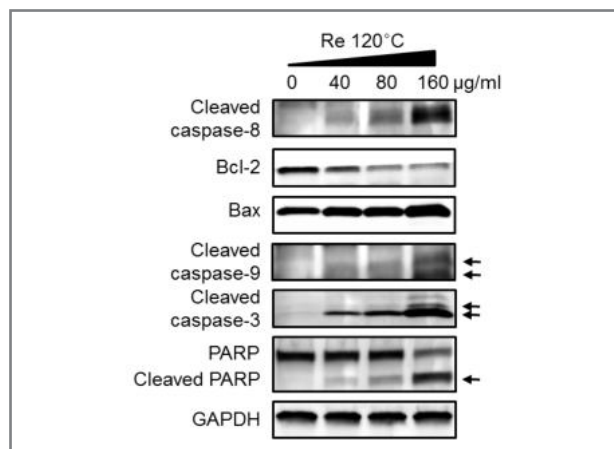


Figure 7. Effect of heat processed-ginsenoside Re on pro- and anti-apoptosis proteins in AGS cells.

Conclusion

Research has been conducted into the development of a method for increasing the pharmaceutical effect of ginseng by conversion of the dammarane-based saponin by high temperature, high pressure thermal processing [2,3]. Our investigation clearly demonstrated that heat-processing strengthened antioxidant and anticancer effects of ginsenoside. The free radical-scavenging activity of ginsenoside Re-lysine mixture increased upon heat-processing due to the generation of antioxidant MRPs. However, the increased anticancer effect of ginsenoside Re-lysine mixture upon heat-processing was mainly derived from less-polar ginsenosides and was not

related to the antioxidant MRPs. Molecular mechanisms involved in ginsenoside Re upon heat-processing-induced apoptosis might be attributed to the regulation of Bcl-2 and Bax, as well as the caspase-dependent apoptotic pathway. A better understanding of the mechanism of the antioxidant and antiproliferating effects of ginsenoside upon heat-processing will aid in the development of effective cancer chemotherapeutic strategies involving their use as potential anticancer adjuvants.

Note

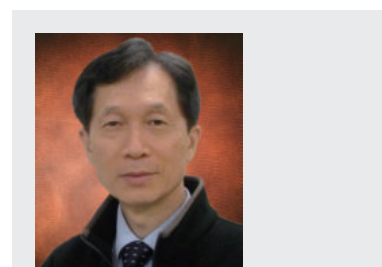
This article and images are cited from “Increase in antioxidant and anticancer effects of ginsenoside Re-lysine mixture by Maillard reaction” in *Food Chemistry*, Vol. 138 (2-3), pp. 876-883.

References

- [1] Yun TK. *J. Kor. Med. Sci.* 2001; 16: S3-S5.
- [2] Kasai R, Besso H, Tanaka O, Saruwatari Y, Fuwa T. *Chem. Pharm. Bull.* 1983; 31: 2120-2125.
- [3] Kim WY, Kim JM, Han SB, Lee SK, Kim ND, Park MK, Kim CK, Park JH. *J. Nat. Prod.* 2000; 63: 1702-1704.
- [4] Kang KS, Lee YJ, Park JH, Yokozawa T. *Biol. Pharm. Bull.* 2007; 30: 1975-1978.
- [5] Yamabe N, Lee JG, Lee YJ, Park CH, Kim HY, Park JH, Yokozawa T, Kang KS. *J. Ginseng Res.* 2011; 35: 60-68.
- [6] Yamabe N, Kim YJ, Lee S, Cho EJ, Park SH, Ham J, Kim HY, Kang KS. *Food Chem.* 2013; 138: 876-883.
- [7] Chuyen NV, Ijichi K, Umetsu H, Moteki K. *Adv. Exp. Med. Biol.* 1998; 343: 201-212.
- [8] Caputo F, Vegliante R, Ghibelli L. *Biochem. Pharmacol.* 2012; 84: 1292-1306.
- [9] Thornberry NA, Lazebnik Y. *Science* 1998; 281: 1312-1316.

[Feature Articles]

Design, Synthesis and Biological Evaluation of Novel Antidepressants: 3-Substituted Azetidine Derivatives as Triple Reuptake Inhibitors



Hahn, Hoh Gyu

Chemical Kinomics Research Center
hghahn@kist.re.kr

Introduction

Depression is one of the leading causes of disease worldwide. Epidemiological studies demonstrate that depressive disorders are highly prevalent; it is estimated that, in general, the lifetime prevalence of major depression is 20% in women and 10% in men. The incidence of depression has risen every year since the early 20th century. There are probably many reasons for this rise, though most studies point to significant socioeconomic changes and complicated circumstances experienced by the younger generation. Pathophysiologically, the cause of depression is commonly associated with a deficiency of monoamine neurotransmitters (serotonin (5-HT), norepinephrine (NE) and dopamine (DA)) in the brain, and a number of antidepressants aim to increase the levels of these neurotransmitters in the synapses (see Figure 1). Historically however, the earliest medications, like monoamine oxidase inhibitors and tricyclic antidepressants, were associated with serious side effects [1]. Among various monoaminergic strategies for maintaining the concentration of neurotransmitters, blocking the reuptake of neurotransmitters by pre-synaptic 5-HT, NE and DA transporters (SERT, NET and DAT) has been an important strategy in modern antidepressant therapy [2]. More recently, drugs which act by either selectively blocking the reuptake of one or two of the neurotransmitters, such as serotonin, norepinephrine or dopamine, have been established as effective antidepressants. An important recent development has been achieved with the discovery of triple reuptake

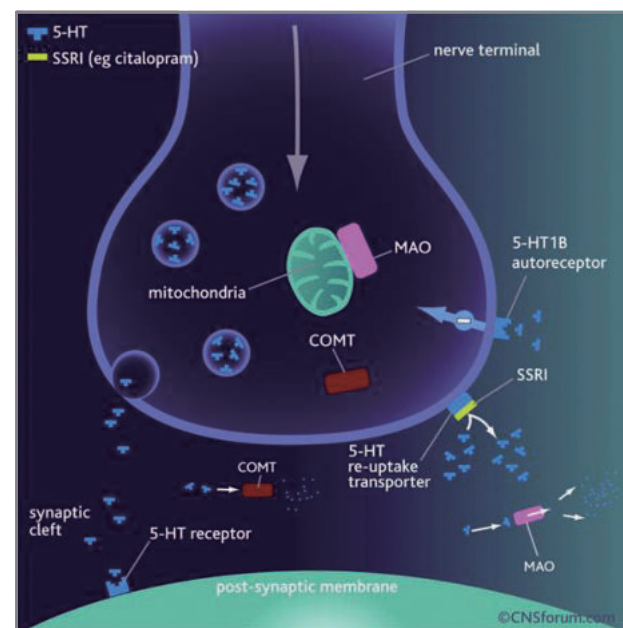


Figure 1. Secretion, signal transmission and reuptake of serotonin in synapse [3].

inhibitors (TRI), broad spectrum antidepressants that are capable of inhibiting the reuptake of monoamines by one molecule (see Figure 2). TRIs working as a single molecule are expected to become the next generation of antidepressants and offer desirable therapeutic effects.

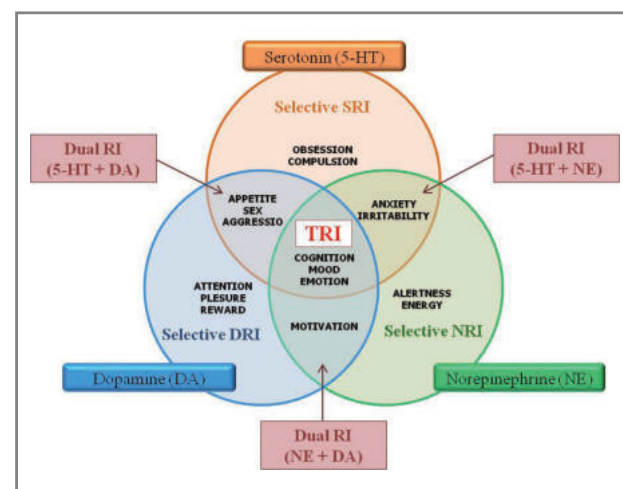


Figure 2. The target Triple Reuptake Inhibitor (TRI) in major neurotransmitters (5-HT, NE and DA) and their related physiological function.

Design

Our initial effort to explore target compounds for the development of a novel TRI for use as an antidepressant focused on the design of novel compounds through the structure analysis and molecular modification of already-marketed reuptake transporter-based antidepressants. We selected fluoxetine [4], atomoxetine, reboxetine [5] and duloxetine [6], all of which have the 3-aryl-3-oxypropylamine scaffold in their structures. These compounds significantly affect the central nervous system (CNS) by the monoamine reuptake inhibitory mechanism. The characteristic common point of these compounds is that they have a 3-aryl-3-oxypropylamine scaffold and rotatable bonds (α and β) (see Figure 3).

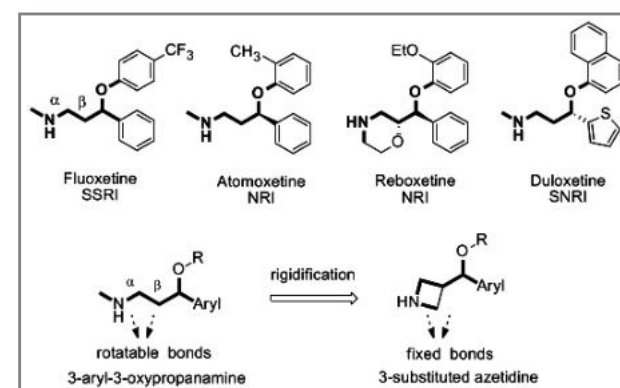
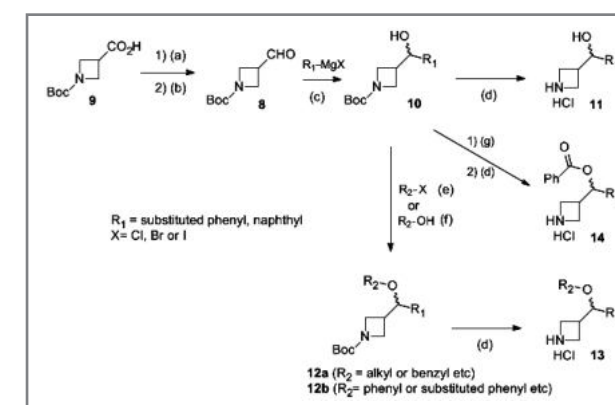


Figure 3. Design of 3-azetidine derivatives by rigidification of rotatable bonds based on antidepressant 3-aryl-3-oxypropylamine derivatives.

Based on structural analysis of selected compounds that show TRI activity, structures which show antidepressant activity should: a) be basic due to the 2° or 3° amino moiety; b) have an amino nitrogen atom present in the cyclic ring; c) have one or two aromatic groups present; and d) have one or more hydrogen bonding acceptors or donors. With these preliminary intentions in mind, we designed novel 3-substituted azetidine derivatives by modifying the 3-aryl-3-oxypropylamine scaffold.

Syntheses

The overall synthetic route of azetidine derivatives **13** is depicted in Scheme 1. Aldehyde **8** was obtained in 80% yield from the reduction of commercially available **9** by the treatment of borane-dimethyl sulfide complex in tetrahydrofuran (THF) at 0°C, followed by Swern oxidation. Grignard reaction of **8** with aryl magnesium halide in THF at 0°C gave an intermediate, secondary alcohol **10**. Azetidinyl alkyl ether **12a** (R_2 = alkyl, benzyl etc) was prepared by two synthetic methods. In the case of R_2 = alkyl, the secondary alcohol **10** was treated with either alkyl halide or benzyl halide in the presence of sodium hydride in THF at ambient temperature to give the corresponding alkyl or benzyl ether **12a** in high yields (48–87%). In the case of R_2 = phenyl or substituted phenyl, azetidinyl phenyl ether derivatives **12b** were prepared successfully by Mitsunobu reaction. The reaction of **10** with substituted phenol in the presence of triphenylphosphine and diisopropyl azodicarboxylate in THF at room temperature afforded the corresponding ether **12b** in high yields (75–91%). Deprotection of the Boc group in **12a** or **12b** by the treatment of 1N HCl in boiling methanol gave the corresponding **13**. The products **13** could be simply obtained by filtration from the reaction mixture with isolated yields ranging from 12 to



Scheme 1. Reagents and reaction conditions: (a) $BH_3 \cdot SMe_2$, THF, 0°C; (b) $(COCl)_2$, DMSO, then TEA, CH_2Cl_2 , -78°C to 0°C; (c) THF, 0°C; (d) 1N HCl, MeOH, 60°C; (e) NaH, THF, reflux; (f) PPH_3 , DIAD, THF, r.t.; and (g) benzoyl chloride, TEA, DAMP, CH_2Cl_2 , 0°C to r.t.

99%. The structures were confirmed by 1H and ^{13}C NMR spectroscopy and HRMS. The obtained solids were the corresponding hydrogen chloride salts of azetidine, which could be used directly for TRI screening. We synthesized 86 analogues of the azetidines **11**, and **13** in this manner.

Biological screening

DA, NE, and serotonin neurotransmitter uptake activities were measured using the Neurotransmitter Transporter Uptake Assay Kit (Molecular Devices, Sunnyvale, CA, USA) with a FDSS6000 96 well fluorescence plate reader, which is a high throughput screening device (Hamamatsu Photonics, Hamamatsu, Japan) [7]. Human embryonic kidney 293 (HEK293) cells stably transfected with human DA transporter (HEK-hDAT), human NE transporter (HEK-hNET), or human serotonin transporter (HEK-hSERT) were used for the assay. The IC_{50} values of the synthesized compounds revealed the superiority of the azetidine derivatives **13** as a superior novel scaffold for application as three monoamine reuptake inhibitors in comparison to the three reference compounds (fluoxetine, nisoxetine, and GRB12909). Some compounds showed excellent biological activities against three monoamine uptake inhibition as well as hERG inhibition profiles [8]. Having obtained the three monoamine uptake inhibitory profiles, we carried out human cytochrome P450 (CYP) enzyme assay and investigated the metabolic stability at human liver microsomes.

In the next step of the characterization, the drug development of a novel scaffold was related to the *in vivo* behavior activity of the compounds using an animal model. Based on their overall balanced profiles in terms of IC_{50} values against three monoamine uptake inhibitory activity, CYP assay data, metabolic stability, and hERG inhibition data, we chose two compounds for further brain-blood barrier (BBB) study and pharmacokinetic (PK) investigation. Since BBB permeability [9] is one of the

factors relevant to the success of CNS-targeted drugs, brain penetration was also evaluated. These compounds showed adequate brain to plasma ratio of 0.86 and 2.70, respectively. The PK profiles of these compounds in rats were evaluated and showed moderate bioavailability (F) of 5.68 and 5.84, respectively.

To verify the potential antidepressant effect *in vivo* of these novel azetidine derivatives, we selected one compound for profiling in a forced swimming test (FST) in mice, known for sensitivity to antidepressant drugs. The compound showed a dose-dependent reduced immobility time at 5.0 and 10.0 mg/kg, which was statistically significant compared to the control group. Oral administration also showed dose-dependent reductions in immobility at 20 and 40 mg/kg.

Figure 4 summarizes the compound exploration process. Starting from a structural analysis and molecular modification of marketed antidepressants, two hit compounds were developed through a unique design and synthesis process based on their structure-activity relationships. The compounds were then subjected to various screenings, including functional assay, CYP450 inhibition, microsomal stability, hERG channel, BBB, PK and *in vivo* testing.

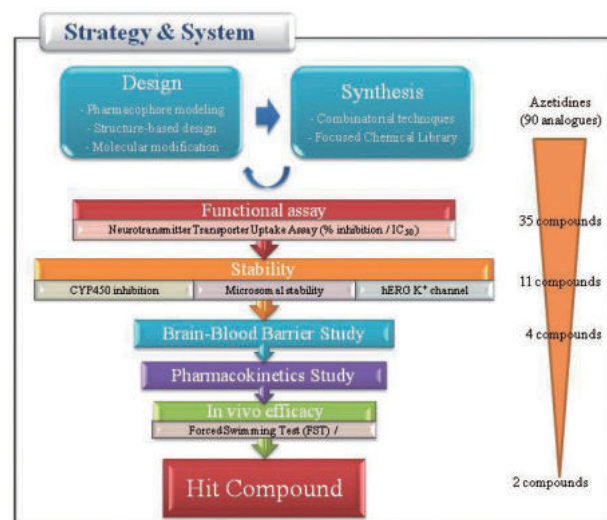


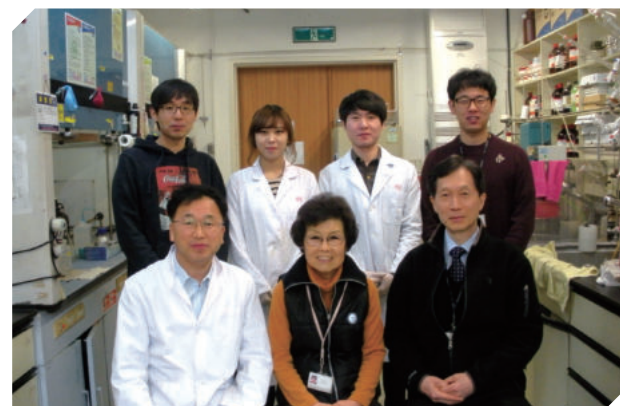
Figure 4. An overview of the system used for exploration of hit compounds.

Summary

We designed a novel class of 3-substituted azetidine derivatives **13** by molecular modification of 3-aryl-3-oxypropylamine analogues, and thereby achieved the study goal of creating a single molecular entity with triple activities as 5-HT, NE and DA reuptake transporters. The bulkiness of the substituent at oxygen (R_2) and the presence of the naphthyl moiety at R_1 were clearly important for these activities. To verify the potential antidepressant effect *in vivo* of these novel azetidine derivatives, we selected one compound for FST profiling in mice. This compound showed a dose-dependent reduction of immobility at 5 and 10 mg/kg IV. A similar result was obtained by oral administration of the compound. These 3-substituted azetidine derivatives therefore represent an important new scaffold to act as single-molecule TRIs for application as the next generation of antidepressants

Note

This article and images are cited from “Exploration of novel 3-substituted azetidine derivatives as triple reuptake inhibitors” in *J. Med. Chem.* 2012; 55: 8188-8192.



References

- [1] Zisook S, Rush AJ, et al. *Biol. Psychiatry* 2006; 59: 203-210.
- [2] Prins J, Olivier B, et al. *Expert Opin. Investig. Drugs* 2011; 20: 1107-1130.
- [3] Rang, HP, Dale MM, et al. *Pharmacology*, 4th Edition. Edinburgh, UK: Harcourt Publishers Ltd: 2001; pp. 165-176.
- [4] Wong DT, Perry KW, et al. *Nat. Rev. Drug Discov.* 2005; 4: 764-774.
- [5] Bymaster FP, Katner JS, et al. *Neuropsychopharmacology* 2002; 27: 699-711.
- [6] Schueler YB, Koesters M, et al. *Acta Psychiatr. Scand.* 2011; 123: 247-265.
- [7] Jørgensen S, Nielsen EØ, et al. *J. Neurosci. Methods* 2008; 169: 168-176.
- [8] Choi KH, Song C, et al. *Biochim. Biophys. Acta* 2011; 1808: 1560-1566.
- [9] Reichel A. *Curr. Drug Metab.* 2006; 7: 183-203.

[Technical Review]

Reducing Pollution by Abatement of NO_x Emissions Through NH₃ SCR



Heon Phil Ha
Center for Materials Architecture
heonphil@kist.re.kr



Kyungju Lee
leekj@kist.re.kr

Introduction

Nitrogen oxides (NO_x, x = 1,2), are major air pollutants, which contribute to environmental degradation in various ways, through photochemical smog, acid rain, ozone depletion, and fine particle pollution. The major source of nitrogen oxides is the combustion of fossil fuels, particularly petroleum and petroleum products in vehicle engines as well as coke in thermal power plants [1]. In particular, abatement of NO_x from diesel engines has been a major challenge in environmental catalysis, but recently, research into selective catalytic reduction (SCR) of NO_x with NH₃ (NH₃-SCR) has led to a highly promising technology for the removal of NO_x from diesel engines at low temperatures. The main focus of this technical review is to describe KIST's efforts in developing SCR catalysts for the removal of NO_x by ammonia in the presence of excess SO₂ and H₂O at low temperatures.

Background

In recent decades, extensive work has been carried out in the development of SCR catalysts for the removal of NO_x from stationary and mobile sources. As part of ongoing research, ammonia-SCR catalysts have been extensively investigated for application in heavy-duty vehicles and

industrial applications [2]. In addition, emissions from locomotive and marine diesel engines have been a cause of much concern due to their emission of large amounts of NO, which is expected to increase due to projected future growth in the use of diesel engines. In the case of marine applications, high sulfur-containing fuel is typically used and flue gas temperature is quite low. Therefore, only limited success has been achieved in reducing emissions from these sources because of the presence of large quantities of SO₂ and water, which prevent the application of current existing technology, especially at low temperatures.

Most low-temperature catalysts have been investigated using V₂O₅, Fe₂O₃ and MnO_x as active components on metal oxide supports such as TiO₂, Al₂O₃ and ZrO₂ [3, 4]. It has been found that using titanium dioxide (TiO₂) as a supporting material is an effective strategy to improve the sulfur tolerance [5]. Matsumoto et al. [6] reported that the decomposition temperature of sulfates on a TiO₂ support was lower than that on a Al₂O₃ support under reducing conditions. Therefore, the commercially developed NH₃-SCR catalysts in industry are mainly based on V₂O₅-WO₃/TiO₂. Although vanadia-titania-based catalysts are highly active and quite resistant to SO₂, there are several drawbacks to their use, including: (a) poor N₂ selectivity at high temperatures; (b) higher amount of toxic V₂O₅; (c) high conversion of SO₂ to SO₃; (d) phase transformation of TiO₂ from anatase to rutile at high temperatures (above 500°C) reducing its activity; and (e) a narrow active temperature window of 300–400°C (although this temperature range does help to avoid pore plugging from the deposition of ammonium sulfate salts such as NH₄HSO₄ and (NH₄)₂SO₄ on the catalyst surface) [7]. The addition of tungsten (W) or molybdenum (Mo) has helped to overcome the phase transformation problem, and many other efforts have been made by researchers to further modify the V₂O₅-WO₃/TiO₂ catalyst system for NH₃ SCR.

Catalyst design by QCC modeling There have been different models developed by scientists that assist

in identifying possible chemical structures and/or their chemical interactions with intermediates and products. At KIST we have designed catalysts by quantum chemical calculation (QCC) to weaken the adsorption of ammonium bisulfate on the catalyst surface. Our ultimate goal was to develop a highly active catalyst (LTC) for NH₃-SCR in the presence of excess H₂O and SO₂ at low-temperatures. In this regard, adsorption of ammonium bisulfate on the V₂O₅/TiO₂ promoted by metal (M) was modeled as described in Figure 1. QCC was carried out to estimate bonding strengths between ammonium bisulfate and transition metals. In the course of this study, metals which had weak bond strength were screened from the periodic table and selected as candidate-promoting materials for NH₃-SCR to reduce the low-temperature sulfur dioxide deactivation caused by the formation and deposition of ammonium bisulfate salts over metal-promoted V₂O₅/TiO₂ catalysts.

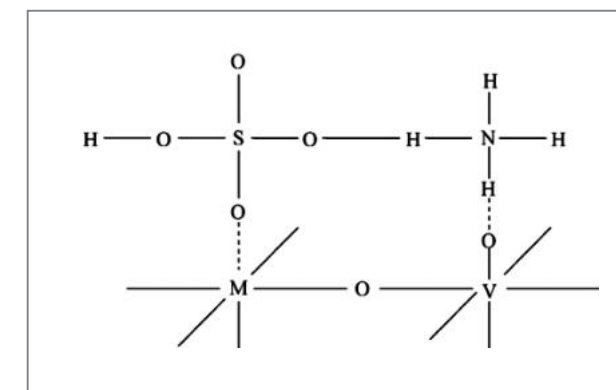


Figure 1. Modeling for the adsorption of ammonium bisulfate over V₂O₅-MO_x/TiO₂.

Experimental

Preparation of the catalysts A commercial TiO₂ (DT-51, Millennium Chemicals) powder was used as a support for the preparation of all catalysts. The V₂O₅/TiO₂ catalyst was prepared by incipient wetness co-impregnation of vanadia on titania by using an ammoniummetavanadate

(NH_4VO_3) (99%, Junsei chemicals) precursor. The required amount of ammoniummetavanadate was added to an oxalic acid solution, followed by heating to dissolve ammoniummetavanadate. A calculated amount of titania (DT-51) powder was added to this solution and stirred for an hour, followed by evaporation, drying and calcination at 500°C for 5 h in air. Following the same procedure, a series of $\text{MO}_x\text{-V}_2\text{O}_5/\text{TiO}_2$ catalysts were prepared by using different metal (Se, Sb, Cu, S, B, Bi, Pb and P) precursor salts (99%, Aldrich chemicals) [8]. Similarly, to understand the effect of Ce-addition, $\text{V}_2\text{O}_5\text{-CeO}_2/\text{TiO}_2$ and $\text{Sb-V}_2\text{O}_5\text{-CeO}_2/\text{TiO}_2$ (Sb was chosen due to excellent sulfur tolerance at low temperatures) catalysts were prepared by incipient wetness co-impregnation of vanadia and antimony on a prepared $\text{CeO}_2/\text{TiO}_2$ support. The $\text{CeO}_2/\text{TiO}_2$ support was synthesized by a deposition precipitation method by hydrolysis with ammonium hydroxide (Aldrich, 25%). In a typical experiment, the required quantities of cerium (III) nitrate ($\text{Ce}(\text{NO}_3)_3 \cdot 6\text{H}_2\text{O}$, Alfa Aesar, 99.5%) and commercial TiO_2 (DT-51, Millennium Chemicals) powder were mixed together in a beaker with de-ionized water. To this mixture solution, dilute aqueous ammonia was added as a precipitating agent and the resultant precipitate was filtered off. The obtained cake was oven dried at 120°C for 12 h and then calcined at 500°C for 5 h. The obtained $\text{V}_2\text{O}_5\text{-Ce}/\text{TiO}_2$ and $\text{Sb-V}_2\text{O}_5\text{-Ce}/\text{TiO}_2$ catalysts were denoted as VCe/TiO_2 and $\text{SbVxCe}/\text{TiO}_2$ ($x = 0, 5, 10$ and 15 wt% of ceria).

Results and discussion

Screening of metals by QCC modeling QCC was carried out to estimate bonding strength between ammonium bisulfate and different promoters chosen from the periodic table. An adsorption model of ammonium bisulfate to $\text{V}_2\text{O}_5/\text{TiO}_2$ catalysts [9] is schematically presented in Figure 1. The diagram shows the ammonium bisulfate adsorption onto the $\text{V}_2\text{O}_5/\text{TiO}_2$ surface where the TiO_2 surface is covered by V_2O_5 and a promoter,

and where Ti is replaced with an arbitrary atom M. In the model, the bonding strength of $\text{M}\text{---}\text{O}$, which is normally stronger than the adjacent $\text{H}\text{---}\text{O}$ bond, plays a critical role in the sulfur poisoning. If the bonding strength ($\text{M}\text{---}\text{O}$) is somehow weaker, the formed ammonium bisulfate salt can be easily desorbed. From the quantum chemical calculation, suitable metal promoters like Se, Sb, Cu, S, B, Bi, Pb and P were selected, which were likely to favor the weaker ($\text{M}\text{---}\text{O}$) bonding strength, resulting in easy desorption of adsorbed ammonium bisulfate salt formed during $\text{NH}_3\text{-SCR}$ of NO_x reaction over the catalyst surface at temperatures < 240°C. Among all the selected metal promoters, the order of bonding energy decreased as $\text{Pb} > \text{B} > \text{Bi} > \text{Cu} > \text{Sb} > \text{Se} > \text{S} > \text{P}$ (Table 1).

Table 1. The quantum chemical calculation results

Element	Bond Energy (eV)
Selenium (Se)	+2.940
Antimony (Sb)	+3.129
Copper (Cu)	+3.158
Sulfur (S)	+2.770
Boron (B)	+3.721
Bismuth (Bi)	+3.509
Lead (Pb)	+3.731
Phosphorous (P)	+2.501

Influence of promoters on SCR activity in the presence of oxygen The NO_x conversion of different metal-promoted $\text{V}_2\text{O}_5/\text{TiO}_2$ catalysts (Figure 2) was measured at temperatures ranging from 150 to 400°C with a reaction mixture containing 800 ppm NO_x , 800 ppm NH_3 , 3% O_2 at a space velocity of 60,000 h^{-1} . The results show a considerable increase in reaction rate at low temperatures (150–300°C). NO_x conversion of all catalysts increased with increasing temperature and achieved almost 100% NO_x conversion at 300°C. A considerable difference in the conversion was observed at low temperatures below 250°C. Among the candidate metals identified from QCC modeling, S and P did not adequately reduce NO_x . However, selenium (Se) showed the highest NO_x conversion at low temperatures, followed

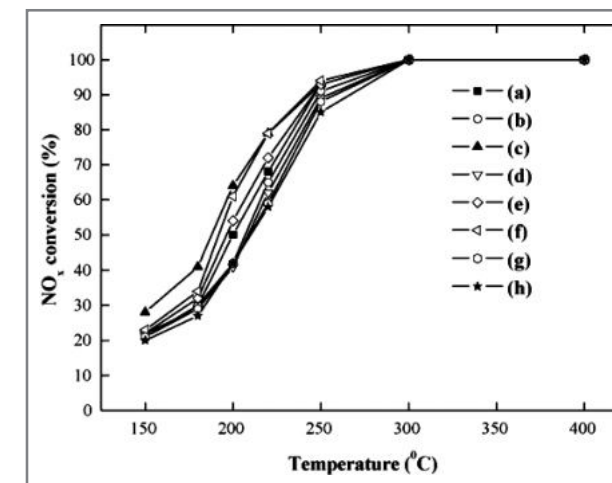


Figure 2. NO_x conversion vs. temperature over (a) $\text{V}_2\text{O}_5/\text{TiO}_2$ (b) 1% $\text{Cu}/\text{V}_2\text{O}_5/\text{TiO}_2$ (c) 1% $\text{Se}/\text{V}_2\text{O}_5/\text{TiO}_2$ (d) 1% $\text{Pb}/\text{V}_2\text{O}_5/\text{TiO}_2$ (e) 1% $\text{S}/\text{V}_2\text{O}_5/\text{TiO}_2$ (f) 1% $\text{Sb}/\text{V}_2\text{O}_5/\text{TiO}_2$ (g) 1% $\text{B}/\text{V}_2\text{O}_5/\text{TiO}_2$ (h) 1% $\text{P}/\text{V}_2\text{O}_5/\text{TiO}_2$ (Reaction conditions: 800 ppm NO_x , 800 ppm NH_3 , 3 vol% O_2 , GHSV – 60,000 h^{-1}).

by antimony (Sb). The efficiency order of promoters for NO_x conversions at low temperatures followed the ordered sequence: $\text{Se} > \text{Sb} > \text{S} > \text{Cu}$. The $\text{V}_2\text{O}_5/\text{TiO}_2$ catalyst showed a 50% NO_x conversion at a temperature of 200°C, whereas $\text{Se}/\text{V}_2\text{O}_5/\text{TiO}_2$ and $\text{Sb}/\text{V}_2\text{O}_5/\text{TiO}_2$ showed 64% and 61% of conversions, respectively.

Low-temperature SO_2 deactivation studies of $\text{MO}_x/\text{V}_2\text{O}_5/\text{TiO}_2$ In order to determine deactivation characteristics, NO_x conversions were measured with the introduction of 500 ppm SO_2 along with 800 ppm of NO , 800 ppm of NH_3 , 6% H_2O and 3% O_2 . Low-temperature SO_2 deactivation studies were carried out at 240°C for the metal-promoted (Se, Sb, Cu and S) $\text{V}_2\text{O}_5/\text{TiO}_2$ catalysts, which showed high NO_x conversions. Among the metal-promoted catalysts, Se, Sb, Cu and S showed high NO_x conversions. Figure 3 explains the effect of SO_2 addition on NO_x reduction over $\text{V}_2\text{O}_5/\text{TiO}_2$ and that promoted with Se, Sb, Cu, and S. The SO_2 deactivation was more serious on the Copper (Cu)-promoted catalyst than others due to easy formation of CuSO_4 . This is in agreement with the order of bonding energy ($\text{M}\text{---}\text{O}$) of the metal promoters ($\text{Cu} > \text{Sb} > \text{Se} > \text{S}$). The selenium catalysts also showed deactivation after 4 h because of high vapor

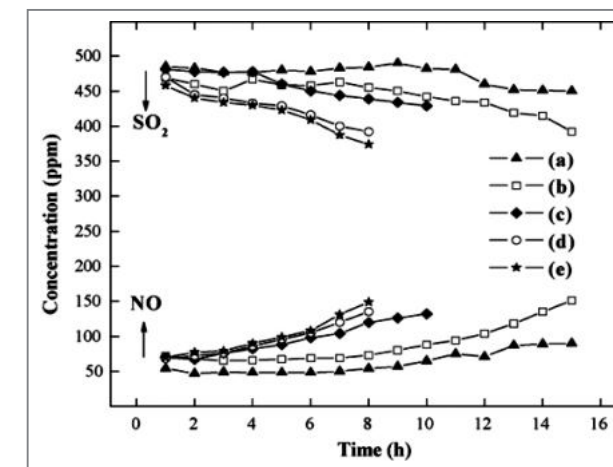


Figure 3. SO_2 deactivation study at 240°C over (a) 1% $\text{Sb}/\text{V}_2\text{O}_5/\text{TiO}_2$ (b) $\text{V}_2\text{O}_5/\text{TiO}_2$ (c) 1% $\text{Se}/\text{V}_2\text{O}_5/\text{TiO}_2$ (d) 1% $\text{S}/\text{V}_2\text{O}_5/\text{TiO}_2$ (e) 1% $\text{Cu}/\text{V}_2\text{O}_5/\text{TiO}_2$ (Reaction conditions: 800 ppm NO_x , 800 ppm NH_3 , 3 vol% O_2 , 6 vol% H_2O , 500 ppm SO_2 , GHSV – 60,000 h^{-1}).

pressure at reaction temperature. The best performance was obtained using antimony (Sb)-promoted $\text{V}_2\text{O}_5/\text{TiO}_2$ catalyst [10]. The amount of ammonia slip became very small, and the amount of emitted sulfur dioxide was nearly similar to the amount introduced. Therefore, it could be inferred that almost no oxidation of sulfur dioxide occurred within 16 h. This result clearly shows that antimony acts as a promoter enhancing the SO_2 -poisoning resistance. This catalyst has been patented and transferred to Daeyoung Industries Ltd., South Korea.

Influence of low and high temperature activity by ceria addition over SbV/TiO_2 The addition of ceria enhanced catalytic activities both at low and high temperatures (Figure 4). This difference in catalytic activity was more apparent at higher temperatures, but improvement in NO_x conversion was also observed at low temperatures between 175 to 250°C. As ceria loading increased from 5 to 10 wt%, a significant enhancement in the NO_x conversion was observed. However, a further increase in the ceria loading decreased the NO_x conversion, and displayed more or less similar activities for both 5 and 15 wt% ceria-loaded catalysts under given reaction conditions. Moreover, the $\text{SbV10Ce}/\text{TiO}_2$

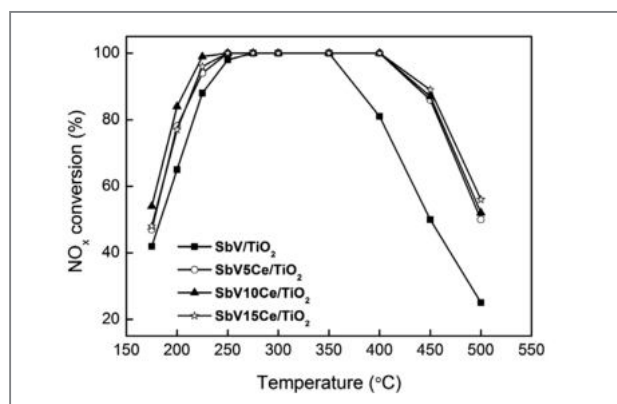


Figure 4. NO_x conversion of ceria added SbV/TiO₂ catalysts. (Reaction conditions: 800 ppm NO_x, 800 ppm NH₃, 3 vol% O₂, GHSV – 60,000 h⁻¹).

catalyst demonstrated a NO_x conversion of nearly 99% at temperatures as low as 220°C, and clearly widened the working temperature window from 250 – 400°C to 200 – 450°C. It is worth noting that the addition of ceria widened the SCR activity temperature window due to the positive synergetic effects of Ce, V, Sb on the surface of TiO₂.

The effect of H₂O and SO₂ on NO_x conversion of SbV/TiO₂, SbV10Ce/TiO₂ and V10Ce/TiO₂ catalysts are displayed in Figure 5 (a). At operating temperatures below 250°C, it was observed that the addition of 6 vol% H₂O and 800 ppm SO₂ into the reaction stream reduced the catalytic activity, while above 350°C, higher NO_x conversions were noticed. These results suggest that water vapor and SO₂ had inhibition effects at lower temperatures. When temperatures were high, the catalysts showed strong resistance to H₂O and SO₂. It can be observed in Figure 5 (a) that, the SbV/TiO₂ catalyst showed lower NO_x conversions compared to the other two catalysts. However, the SbV10Ce/TiO₂ catalyst showed superior catalytic activity (higher than 87%) in a wide temperature window ranging from 220 to 500°C. These results revealed that the addition of ceria could enhance the SO₂ and H₂O resistance. The selectivities of N₂ and N₂O over SbV/TiO₂, SbV10Ce/TiO₂ and V10Ce/TiO₂ catalysts are shown in Figure 5 (b) and (c), respectively. We found that the formation

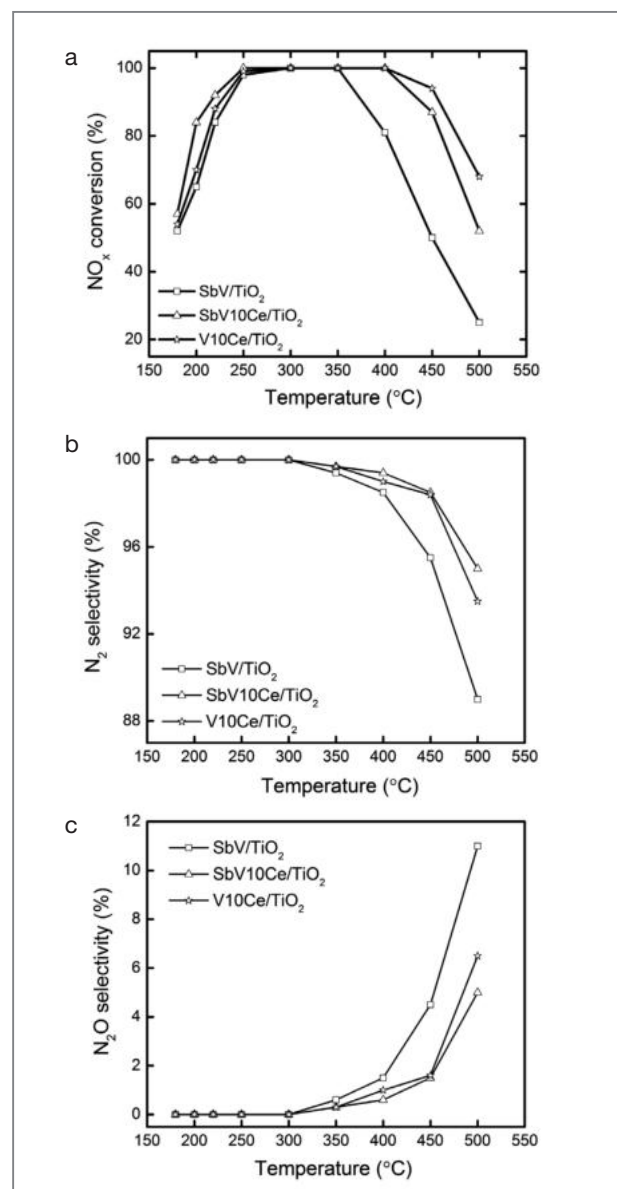


Figure 5. Activity of SbV/TiO₂, SbV10Ce/TiO₂ and V10Ce/TiO₂ samples under H₂O and SO₂ (a) NO_x conversion (b) N₂ selectivity and (c) N₂O selectivity. (Reaction conditions: 800 ppm NO_x, 800 ppm NH₃, 3 vol% O₂, 6 vol% H₂O, 800 ppm SO₂, GHSV – 60,000 h⁻¹).

of N₂O started above 300°C, consequently decreasing formation of N₂. The N₂O formation over the SbV/TiO₂ catalyst increased at temperatures higher than 350°C and reached a maximum of 11% at 500°C. By contrast, a decrease of N₂O formation was observed with the

addition of ceria to the SbV/TiO₂ catalyst, which showed an excellent N₂ selectivity over SbV10Ce/TiO₂ compared to SbV/TiO₂ and V10Ce/TiO₂ catalysts. It is worth noting that the SbV10Ce/TiO₂ catalyst showed N₂ selectivity higher than 95% up to temperatures as high as 500°C. Among all three catalysts, SbV10Ce/TiO₂ expressed the best NO_x conversion and high N₂ selectivity over a wide temperature range between 220 to 500°C.

Acidity and redox properties of VCe/TiO₂ and SbV_xCe/TiO₂ catalysts The NH₃-TPD patterns of SbV/TiO₂, SbV10Ce/TiO₂ and V10Ce/TiO₂ catalysts are presented in Figure 6 (a). These catalysts displayed two broad NH₃ desorption peaks, one in the range of 120–240°C and the other within the range of 250–450°C. The ammonia desorbed at low temperatures was ascribed to weak acidic sites, which correspond to physisorbed ammonia and partially ionic NH₄⁺ bound to Brønsted acid sites [4]. The high-temperature desorbed ammonia was ascribed to desorption of coordinated NH₃ bound Lewis acid sites [4]. As can be noted from Figure 6 (a), the ceria-promoted catalysts showed predominantly more desorbed ammonia at low as well as high temperatures. It seems that cerium species create new acidic sites, inducing a progressive increase of the surface acidity. This is exceptionally beneficial for the enhancement of the NO_x reduction activity with ammonia. Drastic improvement in the total acidity was observed for the SbV10Ce/TiO₂ catalyst as compared to acidity levels in the SbV/TiO₂ and V10Ce/TiO₂ catalysts. Thus, the improvement in ammonia adsorption over ceria-doped catalysts is believed to be significantly beneficial for NO_x reduction by ammonia at a wide temperature range. The NH₃ desorbed at low temperatures during NH₃-TPD was considered to exist on Brønsted acid sites, and that desorbed at high temperatures exist on Lewis acid sites. However, NH₃-TPD cannot differentiate the Brønsted acid sites and Lewis acid sites, i.e., the weak acid sites may contain few Lewis acid sites, and the strong acid sites may contain Brønsted acid sites. These could only be differentiated by *in-situ* DRIFT spectroscopy. Therefore, the catalysts were

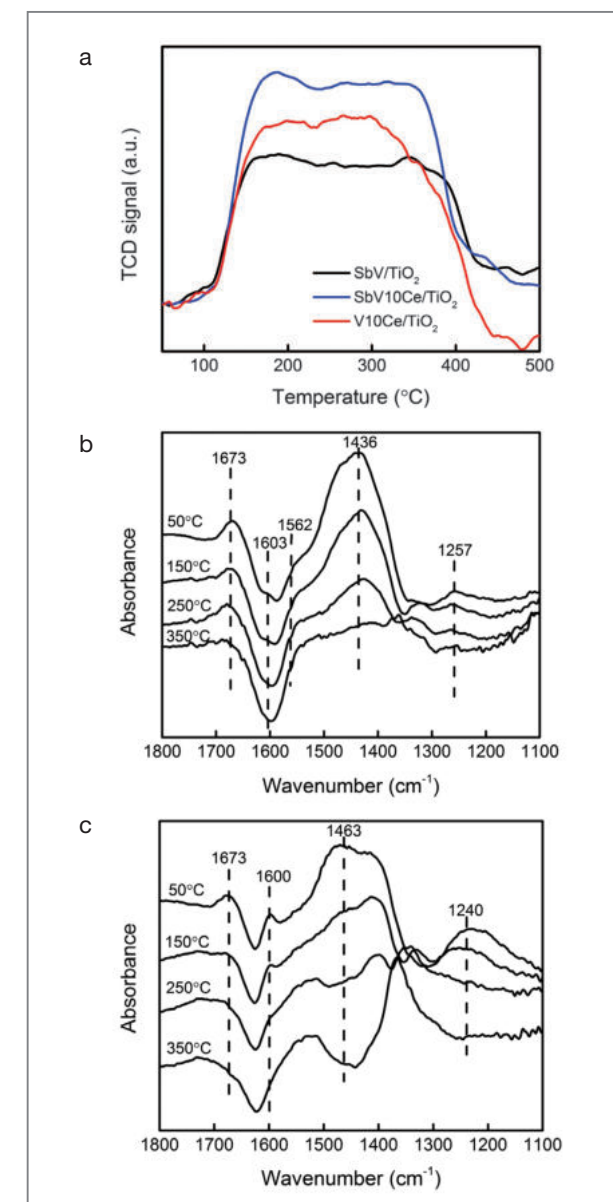


Figure 6. (a) NH₃-TPD patterns of SbV/TiO₂, SbV10Ce/TiO₂ and V10Ce/TiO₂ and (b) DRIFTS spectra of (i) SbV10Ce/TiO₂ & (ii) SbV/TiO₂ samples.

subjected to DRIFTS analysis with ammonia adsorption at room temperature, followed by desorption at various temperatures. The resultant desorption spectra at different temperatures (50, 150, 250 and 350°C) are shown in Figure 6 (b). Figure 6 (b) (i) represents the DRIFT spectra of NH₃ adsorption on a SbV10Ce/TiO₂ catalyst at 50, 150,

250 and 350°C. The vibration of the N-H deformation band of adsorbed ammonia molecules was observed in the range of 1100 – 1700 cm^{-1} . This is an important fingerprint region to differentiate the Lewis and Brønsted acid sites [11]. The bands observed at 1257 and 1603 cm^{-1} can be assigned to asymmetric and symmetric bending vibrations of the N-H bonds in NH_3 coordinately linked to Lewis acid sites [12], while the bands at 1436 and 1673 cm^{-1} could be assigned to asymmetric and symmetric bending vibrations of NH_4^+ bound to Brønsted acid sites [12]. It is noteworthy that the NH_3 adsorbed on Brønsted acid sites was much higher than that at Lewis acid sites.

The SbV/TiO_2 catalyst showed fewer Brønsted acid sites and more Lewis acid sites compared to SbV10Ce/TiO_2 (Figure 6 (b) (ii)). These Lewis acid and Brønsted acid sites were observed at bands of 1240, 1600 cm^{-1} and 1463, 1673 cm^{-1} respectively, on the SbV/TiO_2 catalyst. However, the peaks corresponding to Brønsted acid and Lewis acid sites disappeared above 150°C on the SbV/TiO_2 catalyst. According to the literature and our experimental results, the presence of abundant Brønsted acid sites on a SbV10Ce/TiO_2 catalyst is likely responsible for the increase of the SCR activities at a wide range of temperatures [13]. It is interesting to note that a weak peak at 1562 cm^{-1} appeared in DRIFT spectra for the SbV10Ce/TiO_2 catalyst. This peak is attributed to the $-\text{NH}_3^+$ group [14], indicating that the $-\text{NH}_3^+$ might have been formed from the decomposition of NH_4^+ adsorbed on the Brønsted acid sites. In particular, a group of peaks at 1330-1380 cm^{-1} was observed on the SbV/TiO_2 catalyst, which could be assigned to the intermediates of ammonia oxidation species with a drastic increase in intensities on the SbV/TiO_2 catalyst above 250°C. This indicates that the direct oxidation of ammonia is provoked at higher temperatures over SbV/TiO_2 , which, above 350°C, leads to lower NO_x conversions for the SbV/TiO_2 catalyst compared to ceria-loaded catalysts.

Redox properties of catalysts are directly related to their catalytic efficiency, and can be measured through

temperature programmed reduction (TPR) experiments. The H_2 -TPR patterns of SbV/TiO_2 , SbV10Ce/TiO_2 and V10Ce/TiO_2 catalysts are displayed in Figure 7 (a). All the patterns showed reduction peaks between 300 to 500°C, which could be assigned to the reduction of surface antimony, vanadia and ceria species. These surface reduction peaks were attributed to the reductions from Sb^{5+} to Sb^{3+} , V^{5+} to V^{3+} and Ce^{4+} to Ce^{3+} [15]. The SbV/TiO_2 catalyst exhibited a reduction peak at lower temperatures, around 400°C, while the addition of ceria increased the amount of H_2 uptake as well as the peak maximum temperature to 425°C. This could be attributed to the strong interaction between surface antimony, vanadia and ceria species. However, the amount of H_2 consumption for the V10Ce/TiO_2 catalyst was less than

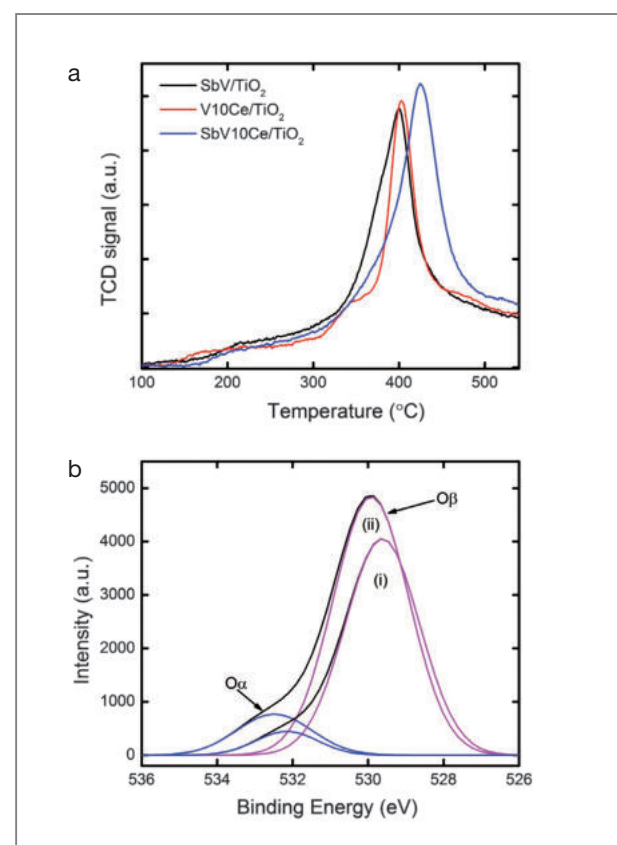


Figure 7. (a) H_2 -TPR patterns of SbV/TiO_2 , SbV10Ce/TiO_2 and V10Ce/TiO_2 and (b) XPS spectra of O 1s of (i) SbV/TiO_2 and (ii) SbV10Ce/TiO_2 samples.

that of SbV/TiO_2 and SbV10Ce/TiO_2 . This result suggests that the surface reduction of antimony oxides provides more lattice oxygen, which is also well supported by XPS spectra (Figure 7 (b)). The synergistic effect of antimony, vanadia and ceria on TiO_2 could induce thermal stability into the SbV10Ce/TiO_2 catalyst, thereby increasing high temperature NO_x reduction activity (>350°C). The total number of reducible species also increased for the SbV10Ce/TiO_2 (89.2 $\mu\text{mol/g}$) catalyst as compared to those of the SbV/TiO_2 (75.3) and V10Ce/TiO_2 (68.7) catalysts. From the above results, it can be concluded that the high acidity and high reducibility of the SbV10Ce/TiO_2 catalyst played an important role in increasing NO_x conversion efficiency in a wide temperature window.

SO_2 on-off long-term stability study Long-term durability studies with SO_2 on-off cycles were performed under isothermal conditions at 240°C. As illustrated in Figure 8, when 6 vol% H_2O and 800 ppm SO_2 were simultaneously added to the gas reaction mixture, the NO_x removal efficiency declined at different rates for the three catalytic systems. A gradual decrease and recovery every 5 h during a SO_2 on-off cycle over a 38 h continuous run was observed. Among all catalysts, the SbV10Ce/TiO_2 catalyst underwent a small decrease in NO_x conversion from 98% to 91%. However, the NO_x conversion of V10Ce/TiO_2 and SbV/TiO_2 catalysts decreased significantly from 91% to 75% and 93% to 60%, respectively. These results express a clear difference in deactivation behavior of the catalysts by H_2O vapors and SO_2 . In the presence of SO_2 and H_2O , SO_2 can be oxidized to SO_3 by O_2 and these SO_x ($\text{SO}_2 + \text{SO}_3$) compounds eventually form ammonium sulfate ($(\text{NH}_4)_2\text{SO}_4$) and/or ammonium bisulfate (NH_4HSO_4) by reacting with slipped NH_3 and H_2O [16]. It is possible that salt formation over the SbV/TiO_2 and V10Ce/TiO_2 catalysts occurred faster than over SbV10Ce/TiO_2 . This might result in a blocking of the catalytic pores and occupation of the catalytic active sites. Conversely, the SbV10Ce/TiO_2 catalyst showed higher resistance to SO_2 and water during 38 h of continuous study. During the course of the

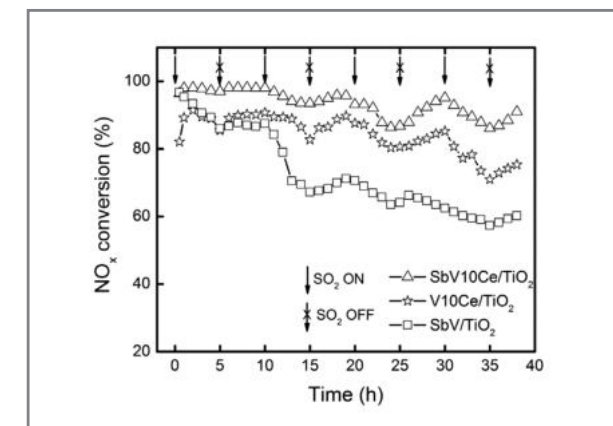


Figure 8. SO_2 on-off studies on SbV10Ce/TiO_2 , V10Ce/TiO_2 and SbV/TiO_2 samples: with SO_2 and H_2O at 240°C. (Reaction conditions: 800 ppm NO_x , 800 ppm NH_3 , 3 vol% O_2 , 6 vol% H_2O , 800 ppm SO_2 , GHSV = 60,000 h^{-1}).

reaction over the SbV10Ce/TiO_2 catalyst, a small amount of formed ammonium sulfates were removed by water in the absence of SO_2 (SO_2 off cycle) after which a gradual increase in the NO_x conversion efficiency was observed. On the other hand, larger amounts of ammonium sulfates formed over the SbV/TiO_2 and V10Ce/TiO_2 catalysts, but these deposits were not able to be completely removed by water in the absence of SO_2 , leading to continuous deactivation of those catalysts. The analysis of SO_2 -TPD for SbV10Ce/TiO_2 catalyst is in good agreement with the above results, indicating that less SO_2 adsorption associated with the SbV10Ce/TiO_2 catalyst is a reflection of its strong resistance to SO_2 and subsequent salts formation. Consequently, it appears that a SbV10Ce/TiO_2 catalyst offers increased resistance against SO_2 and H_2O during a SO_2 on-off long-term stability test.

Note

This article and images are cited from “ SO_2 resistant antimony promoted $\text{V}_2\text{O}_5/\text{TiO}_2$ catalyst for NH_3 -SCR of NO_x at low temperatures” in *Applied Catalysis B: Environmental*; 78(3-4): 301-308.

References

- [1] Bosch H, Jassen F. *Catal. Today* 1988; 2: 369–379.
- [2] Madia G et al. *Appl. Catal. B* 2002; 39: 181–190.
- [3] Kim YJ et al. *Catal. Today* 2010; 151: 244–250.
- [4] Sounak R et al. *Appl. Energy* 2009; 86: 2283–2297.
- [5] Suzuki H et al. *Toyota Tech Rev.* 1996; 46: 68–81.
- [6] Matsumoto S et al. *Appl. Catal. B* 2000; 25: 115–124.
- [7] Busca G et al. *Appl. Catal. B* 1998; 18: 1–36.
- [8] Ha HP et al. *Appl. Catal. B* 2008; 78: 301–308.
- [9] Zhu Z et al. *J. Catal.* 2000; 195: 268–278.
- [10] Ha HP et al. EP1904227.
- [11] Naito N et al. *J. Phys. Chem. B* 1999; 103: 7206–7213.
- [12] Gutierrez-Alejandre A et al. *Langmuir* 1998; 14: 630–639.
- [13] Amiridis MD et al. *Appl. Catal. B* 1999; 20: 111–122.
- [14] Amores JMG et al. *Appl. Catal. B* 1997; 13: 45–58.
- [15] Besselmann S et al. *Phys. Chem. Chem. Phys.* 2001; 3: 4633–4638.
- [16] Zhu Z et al. *Appl. Catal. B* 2001; 30: 267–276.

[Feature Articles]

Real-Time *In Vivo* Imaging of The Beating Mouse Heart at Microscopic Resolution



Sungon Lee

Interaction and Robotics Research
Center
solee@kist.re.kr

Introduction

Intravital microscopy refers to the imaging of live animals at microscopic resolution using fluorescence microscopy. Intravital microscopy, computational advances in optical imaging, and the development of novel molecular probes (new biological reporters [1] and more efficient fluorochromes [2]) have all contributed to significant insights into *in vivo* biology. One of the major advantages of optical microscopy over other imaging modalities, such as magnetic resonance imaging (MRI) and computer tomography (CT), is its high spatio-temporal resolution [3,4]. In addition, *in vivo* observation offers a distinct advantage over traditional *in vitro* and *ex vivo* observation; it provides researchers with a window into natural physiological conditions, which is very important for realistic results. It is well known that *in vitro* observations often correlate poorly with *in vivo* observation. *In vivo* imaging is now often done in optically transparent tissues and model systems (e.g., embryos, fish), isolated organ models (e.g., perfused heart preparations), or it involves exteriorizing and immobilizing entire organs on pedicles (e.g. exteriorized liver) or the use of dorsal skin window chambers [5]. These methods are not always reliable or practical and are not commonly compatible with long term serial observations and survival.

One major practical problem with intravital microscopy is that measurements are profoundly hampered by respiratory and cardiac motion. Thus, motion compensation and tissue stabilization are two major practical

challenges currently faced by researchers using intravital microscopy in murine models [6]. To overcome these issues, a number of different approaches [7-14] have been proposed, including the use of restraining cover slips or suctioning devices. While reducing motion to some degree, these approaches are far from perfect, and often induce tissue damage or alter physiology.

Here, we present a new approach for real-time microscopic imaging, one which involves a combination of motion stabilization and an algorithm for acquisition during advanced cardiopulmonary gating. We use this approach to perform *in vivo* confocal and multiphoton microscopy imaging of the beating murine heart at (sub)cellular resolution. This method not only enables prolonged observation for periods up to several hours, but also allows repeated imaging over several days, making it particularly suitable for studies of inflammatory responses which play out over several days rather than minutes to hours. Finally, we demonstrate that the described technique is capable of both optical sectioning in confocal and multiphoton mode as well as time-lapse fluorescence imaging, allowing cells to be tracked in the beating mouse heart. The method is simple and induces no measurable physiologic damage since the imaging objective is not in direct contact with the tissue being imaged.

Description of the imaging setup

The image stabilization approach consists of two distinct and integrated strategies. Firstly, we designed and implemented a specialized tissue motion stabilizer (Figure 1a-e), which reduces artifacts induced by respiratory and cardiac motion; such motion is typically in the order of several millimeters. Secondly, we used a real-time processing approach (Figure 2a) to trigger stabilized image extraction at appropriate phases of the respiratory and cardiac cycles using a retrospective electrocardiogram (ECG)-gating technique [15]. The custom-designed stabilizer (Figure 1a-e) consists of a 3 cm long rigid metal

shaft and a flat ring at one end (Figure 1b,c). The ring is bonded to the myocardium and thereby provides a contact-free central area in which a water immersion objective rests over unaltered myocardium. Bonding to the myocardium is achieved by coating the underside of the ring with a thin layer of approximately 50 μm of Dermabond, a clinical grade bonding agent which is FDA-approved for human surgical use and commonly used in cardiac surgery. The ring is then gently placed on the area of the heart to be imaged and is in direct contact with the visceral (i.e., inner layer) of the epicardium. Thereafter, the heart is returned to its original position (Figure 1d,e). The only pressure remaining is the one induced by the heart itself while contracting against the stabilizer ring, similar to the heart beating against the chest wall. For this study, the ring was maintained at an incline of 30 degrees, but this angle can be adjusted for other regions of the heart as necessary. The other end of the stabilizer was mounted on a monolithic tri-stage base plate to allow 6 degrees of freedom.

The use of this stabilizer setup resulted in near complete suppression of respiratory and cardiac motion artifacts (Figure 2b). During the entire acquisition period, the stabilizer ring was kept filled with physiological saline solution to provide index matching for the imaging objective and prevent tissue from drying out. To access the heart without altering the position of the ring, we used minimally invasive water immersion MicroProbe objectives (Olympus). Due to their small diameters (1.3mm) and working distances (200 μm), these objectives could be easily accommodated within the ring. Likewise, they also provided the capability for deep (100 μm) tissue imaging. To image deeper tissue structures, we utilized multiphoton imaging in combination with a large working distance (2mm) water immersion objective (Figure 1e). For this, the top side of the ring was machined so as to accommodate a seal-proof 1mm-tall plastic ring extension. A layer of 200 μm to 2 mm of water was present between the heart and the imaging lens, and there was thus no contact between the tissue and the objective (Figure 1e). The objective

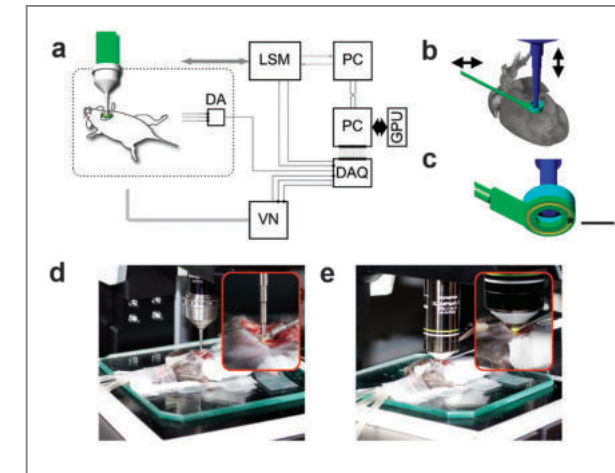


Figure 1. Experimental setup, stabilizer design. (a) Experimental setup: LSM (laser scanning microscope); GPU (graphic processing unit); DAQ (data acquisition card); VN (ventilator); DA (differential amplifier). The DAQ card controls all triggers, measures microscope timing, and records both ECG and lung airway pressure. (b) Three-dimensional schematic model of the motion compensation stabilizer. The underside of the ring's stabilizer was bonded to the surface of the heart. The position of the stabilizer could be adjusted in both the horizontal and vertical planes via a monolithic tri-stage base plate. The stabilizer robustly suppressed artifacts caused by respiration and cardiac contractions. The stabilizer was filled with a saline solution to provide index matching for the imaging objectives and to prevent the underlying myocardium from drying out. (c) Bottom view of the stabilizer. A shallow groove (yellow ring) was carved out in the bottom part of the stabilizer to increase the contact area between the stabilizer and the bonding material and thus ensure better attachment to the heart. Scale bar, 2 mm. (d, e) Pictures of the stabilizing setup during live imaging of the heart using either: (d) a stick objective (20x IV-OB13F20W20; Olympus) or (e) a water immersion objective (20x XLUMPLANFL; Olympus).

and the ring thus functioned as two distinct units which were not connected to each other. In addition, a shallow groove (Figure 1c) was carved out of the underside of the ring to increase the contact area between the glue and the surface of the stabilizer and thus maximize the bond between the stabilizer and the heart. Finally, to maintain both the ring and its enclosed physiological solution at 37°C, both the objective and the stabilizer were thermally controlled via resistive heaters and thermistors.

Retrospective gating acquisition and real-time processing

While the mechanical approach was relatively efficient at reducing the heart's range of motion by several orders of magnitude, residual motion artifacts were still present in the acquired images (Figure 2b); this was presumably a result of the cardiac contractions during the microscope acquisition time (approximately one beat occurs every 200 ms during deep anesthesia in mice). This problem was particularly troublesome during high resolution imaging, where the acquisition time is comparable to, or longer than, one ECG cycle (Figure 2a). To overcome this issue, we implemented both cardiac and respiratory gating. Since animals were mechanically ventilated in a pressure-cycle mode, image acquisition extraction could be gated to a particular phase of the respiratory cycle synchronized with the cardiac cycle (see timing diagram in Figure 2a). Specifically, we chose a ventilator timing window of 90 ms near the end of expiration which was achieved with a constant delay occurring immediately after the initial ventilation trigger. For the cardiac cycle, we chose an image acquisition timing window of 15 ms following the appearance of the P wave and coinciding with end-diastole in the ventricle (Figure 2a). When only cardiac gating was used, respiratory artifacts strongly affected the reconstructions. As a result, this strategy was abandoned.

Multiple gated images within the same phase of the respiratory and cardiac cycles were then consecutively acquired (white box, Figure 2b). These gated data were then fused to generate a final reconstructed image (Figure 2c) which was built in real time during acquisition. Analogously, a prospective gating approach could be adopted in a similar fashion using microscopy systems that allow fast triggering of image scanning. Data processing was done in real time, and all timing and pressure diagrams were recorded using a data acquisition card (DAQ, National Instruments). One PC ("slave") was used to control the microscope electronics and acquire the images, while a second PC ("master") was used to

acquire all timing and physiological data (Figure 1a). The master PC was connected to the slave PC via an Ethernet crossover cable to provide fast data transfer. Data was processed on a graphic processing unit (GPU) for fast denoising using a BM3D filter method [16]; the data were likewise processed for real-time ECG parameter extraction using a well established approach [17-19]. The latter determines the position of the QRS complexes and the beginning of the P waves. These analyses were critical for identifying the gating time window with minimal cardiac motion. All programming for data acquisition, data elaboration, noise reduction, ECG analysis, and cell segmentation was done in Labview, Matlab, C++, and using the Cuda Toolkit. With the setup, we were able to choose either fast (lower resolution) or slow (higher resolution) image acquisition modes. Fast imaging (15 frames per second) is useful for recording dynamic events such as vascular leukocyte tracking whereas slower high resolution images (2 frames per second) are useful when high signal-to-noise ratios (SNR) are required, e.g., for imaging intracellular structures.

Cardiac imaging

We subsequently tested the *in vivo* stabilization method in a mouse model of ischemia reperfusion injury, in which we tracked the migration of exogenously administered cells (Figure 2d). We chose this model because it is a commonly used and clinically relevant injury model [20] and because it allows visualization of leukocyte entry into the ischemic tissue. The left anterior descending artery was temporarily occluded for 30 minutes to induce the ischemic injury and to trigger an inflammatory response. Green fluorescent protein (GFP)-expressing cells, freshly isolated from the bone marrow of donor mice, were subsequently injected into the cardiac apex (Figure 2e), and live mice were imaged 24 hours later. Once the stabilizer was in place (red ring in Figure 2e), Griffonia simplicifolia-I lectin [21] was injected

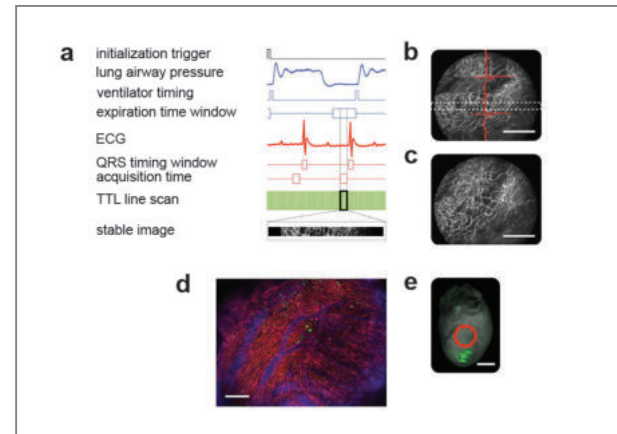


Figure 2. Reconstruction principle and processed data.

(a) Timing diagram used for the gated acquisition of images. From top to bottom: TTL initialization trigger, lung airway pressure, TTL ventilator timing, acquisition time window at the end of the expiration, electrocardiogram (ECG), timing window showing the QRS complex, end-diastolic acquisition time with minimal left ventricular motion, TTL line scan data obtained from the microscope (relative to the image acquired), a section of the image from within the timing window corresponding to a specific portion of the ECG cycle as well as to a well defined phase of the respiratory cycle. (b) Raw image acquired. Motion artifacts are still visible and their effects vary in accordance to the different phases of the ECG cycle (red line). Using a retrospective ECG-gating technique on each acquired image, only data that fell within the two white dotted lines and corresponded with the time gating window in (a) were considered. Scale bar, 200 μm . (c) The acquisition of multiple consecutive images leads to a varied collection of sampled regions. Scale bar, 200 μm . (d) Reconstructed image of the beating heart. Red represents the fluorescence lectin signal from stained capillaries; blue represents the fluorescence signal produced by the blood pool imaging agent Angiosense-680; green represents the GFP-expressing cells. The heart sustained an ischemia reperfusion injury (for 30 minutes) before being injected with GFP-expressing cells in the apex (e). Imaging was performed 24 hours post injury; the image shows migrating cells in the inflamed zone. Scale bar, 200 μm . (e) Fluorescence reflectance image of the heart shown in (d). Green represents the fluorescence signal of the GFP-expressing cells injected into the heart's apex. The red circle indicates the effective area where the stabilizer was positioned. All images were taken with the stabilizer placed on equivalent areas. Scale bar, 2 mm. Images for (d) were acquired using a 10x air objective (Olympus, UPlanFL N NA 0.30), and for (b, c) using a 6x MicroProbe objective (Olympus, IV-OB13F20W20).

by IV, which selectively stained mouse endothelial cells. Angiosense-680, an *in vivo* blood pool imaging agent, was also injected to visualize vascular perfusion. In the reconstructed image (Figure 2d), GFP-expressing cells are clearly visible in an area distant from the injection site, a

finding which suggests cell migration.

During a typical imaging session, we monitored multiple physiological parameters (heart rate, respiratory rate, temperature, blood pressure, oxygenation, hydration, etc). In addition, to determine whether the stabilizer had any effect on tissue perfusion, we imaged both lectin and Angiosense-680 in real time. In so doing, we were able to demonstrate that capillary perfusion appeared normal. ECG data before, during and after intravital imaging sessions showed normal cardiac electrical activity. In addition, heart function was not impaired during or after the imaging sessions. Using cardiac MRI, we quantified the left ventricular ejection fraction (n=4 mice) two days after intravital imaging, comparing it with the ejection fraction obtained before the imaging sessions. Ventricular ejection fractions were similar to pre- and post-intravital imaging. Moreover, CD11b immunohistochemistry staining of heart tissue following intravital imaging showed no inflammatory activity as a result of intravital imaging. Finally, use of fluorescent microspheres, the gold-standard method to measure organ perfusion in a non-survival experiment, did not demonstrate any micro-perfusion abnormalities in the imaging area as compared to control myocardium.

Characterization of the imaging resolution

Our next aim was to determine the extent of residual motion after placement of the stabilizer on the cardiac surface. For this, we injected fluorescein isothiocyanate (FITC)-labeled fluorescent beads (diameter of 5 micrometers) directly into the left ventricle (Figure 3a). After a few minutes, a small percentage of the beads became trapped in the myocardial microvessels, and thus served as reliable fiducial markers. Figure 3b shows the planar position coordinates of a single bead plotted at different time points during consecutively acquired images. Our findings indicated that hardware stabilization

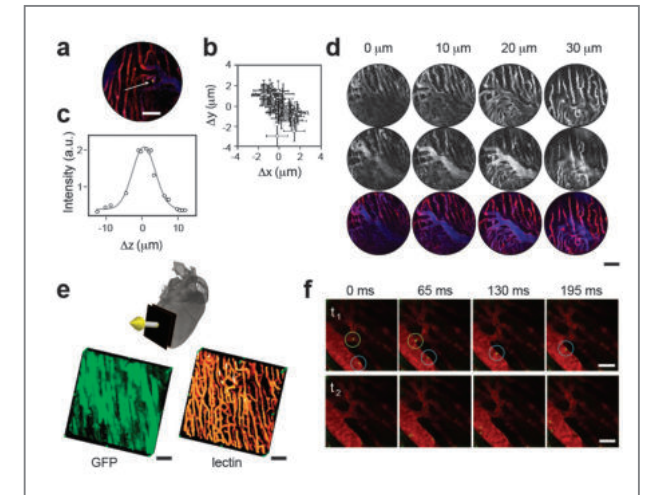


Figure 3. *In vivo* resolution characterization and imaging.

(a) A stabilized image of a fluorescein isothiocyanate (FITC)-labeled bead (diameter: 5 μm), trapped within a microvessel, used to determine the overall stabilized imaging resolution. Red: lectin-stained capillaries; blue: Angiosense-680 (blood pool imaging agent); yellow: the FITC-labeled bead. Scale bar, 50 μm . (b) The planar position coordinates of the trapped bead are plotted at different time points to allow acquisition of consecutive unprocessed images. Error bars correspond to errors in position determination. A resolution of 4 μm was achieved with hardware stabilization. Gating improved the resolution to 2 μm . (c) Characterization of the axial resolution achieved using the gating modality in combination with the motion compensation stabilizer. Here, the axial position of the bead within the imaging time gating window (defined in Figure 1) was determined at different depths. (d) *In vivo* optical sectioning of the myocardium. Top row, lectin. Mid row, Angiosense-680. Bottom row, fusion of top- and mid-row images. Images were taken at different depths in 10 μm increments, using a 20x MicroProbe objective. Scale bar, 50 μm . (e) Optical sectioning along the indicated direction (yellow arrow) allowed three-dimensional reconstructions in a GFP-expressing mouse. Green: GFP-expressing myocytes. Orange: lectin. Scale bars, 50 μm . (f) Time-lapse (65 ms step) fluorescence imaging allowed tracking of cells *in vivo* in the beating heart (Green: Rhodamine 6G-stained leukocytes; red: vessels stained with Angiosense-680). Top row: a single leukocyte (blue circle) is seen rolling along the inner surface of the vessel while another (green circle) is seen passing through the endothelium. Bottom row: a passing leukocyte can be seen initiating rolling. Shadows within the vessels represent red blood cells. Scale bars, 20 μm .

resulted in a planar resolution of 4 μm . This resolution, which can be greatly improved using the above-described gated acquisition approach, is primarily determined by two factors. Aside from obvious considerations regarding the optical components of the setup, the first factor is the reliability with which we can capture the beating heart at

the same time point in the respiratory and heart cycles. The second determining factor is the reproducibility of this time point over multiple image acquisitions. Using the above-described gating, we were able to obtain a planar resolution of approximately 2 μm for a stabilized image.

To measure the axial image resolution, mice were positioned on a translation stage, which provided motion along the vertical axis with nanometer accuracy. Measurements were obtained along the z-axis by moving the mouse (and therefore the heart) along the vertical direction. Both the mouse and the ring holder were located on the same moving plate while 3D stacks were acquired. The axial resolution of the current setup was determined as 7 μm by measuring the axial position of a bead at different depths within the heart, as well as within the imaging time gating window (Figure 3c), defined in Figure 2a.

We also compared stabilized reconstructed images with post-mortem images acquired in the same position. In so doing, we not only verified a good correlation between the two image sets, but also demonstrated the robustness of the technique. Thus, the image stabilizer, when used in combination with gated acquisition, provides superior motion compensation, which in turn facilitates high resolution imaging. The view-sharing approach adopted here may be new for high resolution intravital microscopic imaging, but is well established for cardiac MRI imaging [22].

We subsequently applied this methodology to *in vivo* optical sectioning of the beating heart. This was done by moving the imaging objective along the vertical axis so as to obtain gated reconstructed images at different depths within the myocardium. Stabilized images obtained at four different depths are shown in Figure 3d. Here, fluorescent contrast was obtained using lectin and Angiosense-680 perfusion. If more detailed microvascular analysis is required, three-dimensional renderings of the beating heart could be obtained (as illustrated in Figure 3e) by increasing the number of planes up to the time-gated axial resolution limit.

Imaging leukocyte recruitment

Given that the tissue stabilizer enables such a high degree of motion, we also used it for video rate imaging. This application is particularly useful for studying leukocyte recruitment in real time. To the best of our knowledge, this is the first time that this has been successfully achieved in the beating heart. After ischemia reperfusion injury, we found that Rhodamine 6G-labeled leukocytes could easily be identified within the vessel. Indeed, individual leukocytes could be clearly seen rolling along the endothelium (Figure 3f). In Figure 3f, we show four consecutive frames obtained at a speed of 15 frames per second. Thus, fluorescence time-lapse acquisitions of the stabilized heart, coupled with real-time processing of cell and vessel segmentation, enabled leukocytes to be tracked and counted in the beating heart. As a result, this technique opens up interesting possibilities for *in vivo* flow cytometry of the heart.

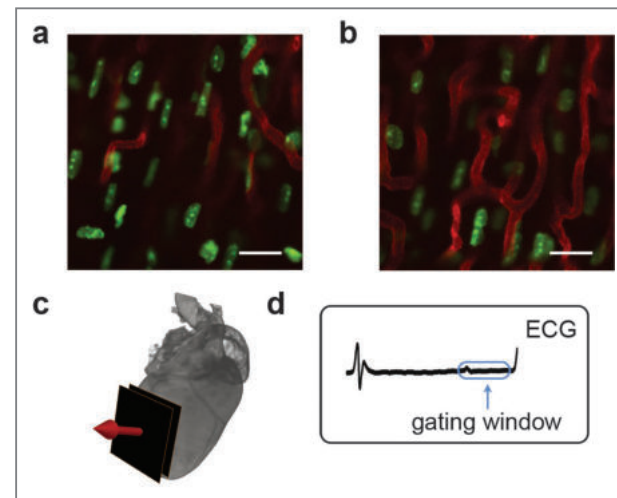


Figure 4. Imaging myocytes in the beating heart at high resolution. Stabilized fluorescence images of myocyte nuclei obtained at two different depths (a, b) within the beating heart while imaging along the indicated direction (c). The image acquisition time window is located within the blue box (d). Both subcellular and subnuclear structures are clearly resolved. Green: fluorescent Hoechst 33258 staining of myocytes; Red: fluorescent lectin staining of capillaries. Scale bar, 20 μm .

Imaging myocytes at subcellular resolution

Finally, the technique is capable of high resolution imaging of individual cells. Arguably, the next frontier in *in vivo* imaging is the ability to improve spatial resolution approximating that of cellular *in vitro* imaging. Here, we used Hoechst 33258 for topical staining of individual myocyte nuclei (Figure 4). As clearly seen in these images, even intranuclear structures (nucleoli) can be resolved in the beating heart using this technique.

Conclusion

We have established a new technique for motion compensation in rapidly moving tissue using a combination of mechanical stabilization and cardiorespiratory gated acquisitions. We demonstrated *in vivo* microscopy imaging, in both confocal and multiphoton mode, in the beating mouse heart for up to four hours over several days. No discernible tissue damage, inflammation, or perturbation of cardiac function was observed during or following imaging sessions. The technique was also shown to be capable of tracking cell migration *in vivo*. Dual-channel fluorescence time-lapse imaging not only enabled the counting of passing leukocytes via *in vivo* flow cytometry (seconds), but also allowed the visualization of both microvascular rolling and extravasation of leukocytes into injured myocardium (minutes) as well as slower tissue migration within the myocardium over prolonged periods (hours). Moreover, we were able to obtain true 4D information (the 4th dimension being time) in the beating heart.

The above described system had a measured gated spatial resolution of 2 x 7 μm (x/y vs. z axis) using calibration beads lodged inside tissue. The ultimate achievable resolution however, is primarily determined by the holder design and ring size. Future designs could be envisioned to further improve on the above resolutions

or coverage, for example, by changing the size or shape of the stabilizer or by increasing its contact area. Finally, similar holders and designs could be adapted to image other organs or orthotopic cancers at high resolution.

Note

This article and images are cited from “Real-time *in vivo* imaging of the beating mouse heart at microscopic resolution” in *Nature Communications*, Vol. 3, 1054, (2012).

References

- [1] Tsien RY. *Annu Rev Biochem.* 1998; 67: 509-544.
- [2] Waggoner A. *Curr Opin Chem Biol.* 2006; 10: 62-66 .
- [3] Condeelis J, Weissleder R. *Cold Spring Harb Perspect Biol.* 2010; 2: a003848.
- [4] Tsien RY. *Nat Rev Mol Cell Biol Suppl.* 2003; SS16-21 .
- [5] Lehr HA, Leunig M *et al.* *Am J Pathol.* 1993;143: 1055-1062 .
- [6] Mai W, Badea CT *et al.* *Magn Reson Med.* 2005; 53: 858-865 .
- [7] Looney MR, Thornton EE *et al.* *Nat Methods* 2011; 8: 91-96.
- [8] Lee S, Nakamura Y *et al.* *IEEE Trans. on Robotics* 2008; 24, 45-54.
- [9] Tabuchi A, Mertens M *et al.* *J Appl Physiol* 2008; 104: 338-346.
- [10] Schroeder JL, Luger-Hamer M *et al.* *Circulation Research* 2010; 106: 1129-1133.
- [11] Gioux S, Ashitate Y *et al.* *Journal of Biomedical Optics* 2009; 14: 064038.
- [12] Hedlund LW, Johnson GA. *ILAR J.* 2002; 43: 159-174.
- [13] McLaughlin RA, Armstrong JJ *et al.* *Opt Express* 2009; 17: 6568-6577.
- [14] Megens RTA, Reitsma S *et al.* *Journal of Biomedical Optics* 2010; 15: 011108.

- [15] Sun Z, Ng KH, Ramli N. *Biomed Imaging Interv J.* 2011; 7: e21.
- [16] Dabov K, Foi A *et al.* *IEEE Trans Image Process* 2007; 16: 2080-2095.
- [17] Li C, Zheng C *et al.* *IEEE Trans Biomed Eng.* 1995; 42: 21-28.
- [18] Pan J, Tompkins WJ. *IEEE Trans Biomed Eng.* 1985; 32: 230-236.
- [19] Chesnokov YC, Nerukh D *et al.* *Computers in Cardiology* 2006; 337-340 .
- [20] Leuschner F, Dutta P *et al.* *Nat Biotechnol.* 2011; 29: 1005-1010.
- [21] Laitinen L. *Histochem J.* 1987; 19: 225-234.
- [22] Foo TK, Bernstein MA *et al.* *Radiology* 1995; 195: 471-478.
- [23] Forouhar AS, Liebling M *et al.* *Science* 2006; 312: 751-753.
- [24] Baatz H, Steinbauer M *et al.* *Int J Microcirc Clin Exp.* 1995; 15: 85-91.

[Feature Articles]

Highly Efficient Transparent Gas Sensors



Hi Gyu Moon
Electronic Materials
Research Center
moonhigy@gmail.com



Jin-Sang Kim
jskim@kist.re.kr



Seok-Jin Yoon
sjyoon@kist.re.kr

Introduction

Simplicity in operation, low cost, flexibility in production and small size constitute the main advantages of metal oxide semiconductor (MOS) chemical sensors over electrochemical, optical, acoustic, and other chemical sensors [1-3]. Since the operation of semiconductor chemical sensors relies on adsorption and desorption of chemical molecules on the surface of sensing materials, operating temperatures usually range from 200 to 400°C, leading to high sensitivity of the sensors. Due to the implementation of heating elements in sensor devices, the power consumption of conventional semiconductor chemical sensors can be as high as hundreds of mW. The use of micromachined silicon platforms reduces the power consumption up to tens of mW, but this is still a substantial drain on portable devices working with lithium batteries. Recent studies have demonstrated ultralow power consumption of chemical sensors based on self-heated individual nanowires or nanobelts [4]. Unfortunately, the sensitivity of these sensors is not high enough for effective operation, and they are difficult to economically mass-produce [5]. In addition to high power consumption, the high operation temperature of conventional semiconductor chemical sensors based on thin or thick films composed of metal oxide nanoparticles induces long-term instability as evidenced by drifts in both sensor resistance and response. Nanoparticles inside the sensing layer suffer from aggregation and encapsulation into larger agglomerates. As a result of this morphology

change, the diffusion of gas molecules through pores inside the sensing layer is hampered, and as a result, the sensor response decreases along with the sensor resistance. Although pre-aging thermal treatment at higher temperatures can improve long-term stability, the complete elimination of aging is practically impossible unless operating temperature is lower than 200°C, at which point grain growth starts in nanoparticles of a few nm in size [6]. On the other hand, any improvements brought about by lowering the operating temperature are compromised by decreases in sensitivity and response rates. Therefore, producing highly sensitive chemical sensors that can operate effectively at low temperatures (< 200°C) is highly challenging.

The goal of our research described in this article was to achieve highly sensitive and stable MOS chemical sensors with low power consumption by nanostructuring the sensing films and enabling a capacity to self-heat. Another key aspect of our effort to develop high performance sensors was to obtain transparency of the sensors. No previously reported chemical sensors have been transparent because substrates, electrodes, heating elements, or sensing films themselves were opaque. Because the constituents of the sensors we developed at KIST are all transparent in visible wavelengths and the fabrication method is simple and scalable, these sensors are ready to be merged directly into transparent electronics, automobile windshields, and other devices or objects requiring invisible components. We believe the research highlighted in this article opens up much broader

applications for the use of chemical sensors on a mass scale.

Fabrication of transparent gas sensors

Indium-tine oxide (ITO) (150 nm thick, 10 Ω/□) interdigitated electrode (IDE) patterns of 5 μm spacing were fabricated on a glass substrate using photolithography and dry etching. After patterning the ITO IDEs, 360 nm thick WO₃ film was deposited onto predefined regions by a shadow mask in the ITO-IDE-patterned glass substrate using room-temperature RF sputtering, where a polycrystalline WO₃ target was utilized for the film deposition. To make the film porous, the sputtering deposition was carried out at a glancing angle (5°). The deposition rate of the film was 8 nm/min. The fabricated WO₃/ITO/glass sensor structure was annealed in air at 500°C for 60 min to crystallize the amorphous WO₃ film. For comparison, a plain WO₃ thin film sensor was fabricated using on-axis RF sputtering which led to the deposition of dense WO₃ film. Figure 1a shows the process of producing porous WO₃ thin films on IDEs by glancing angle deposition (GAD) using a rf sputter. Commercially available ITO-coated glass was used as the substrate and ITO IDEs with an interspacing of 5 μm were patterned using dry etching. Figure 1b shows the simple structure of a fabricated transparent chemical sensor. The 330-nm-thick porous WO₃ thin films are

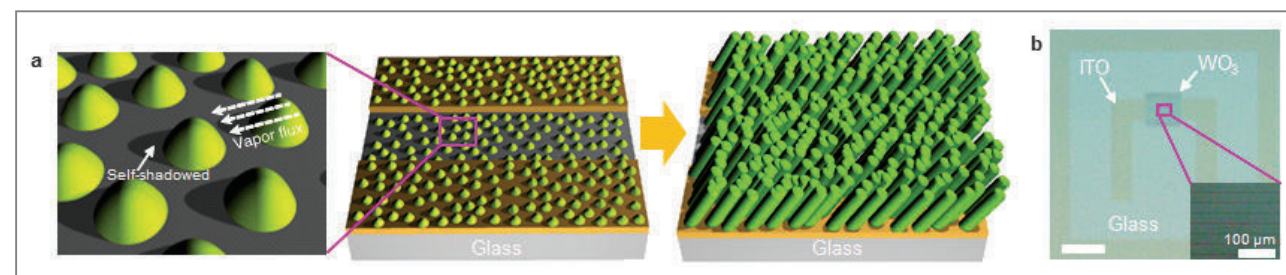


Figure 1. Synthesis of nanocolumnar WO₃ films. (a) Schematics showing the synthesis of nanocolumnar WO₃ film on glass substrate with ITO IDEs using glancing angle deposition. (b) Photograph of a fabricated sensor. Scale bar, 20 mm. Inset: photograph of a nanocolumnar WO₃ film on ITO IDEs.

referred to as *nanocolumnar* WO₃ thin films because of their characteristics which include diameters of individual nanostructures ranging from 30–80 nm and relatively low aspect ratios ranging from 5 to 8. A closer look at the nanocolumnar WO₃ films uniformly deposited between and on ITO IDEs reveals that the films are anisotropic (Figure 1b).

Sensor characterizations

Morphologies of the fabricated sensors were characterized by SEM (XL30 FEG ESEM, FEI) using a 15 kV voltage. TEM was performed using a JEOL-2100 Field Emission TEM. A dual-beam focus ion beam (FEI-Helios, FIB) was used to prepare the TEM samples. The crystallinity and phase of the sensor films were characterized by glancing angle x-ray diffraction (D/Max-2500, Rigaku), in which Cu Kα radiation (wavelength

= 1.5418Å) was used for the X-ray source and the incident angle was fixed at a small angle (2°). For all the WO₃ sensing films, selected area electron diffraction patterns from TEM and X-ray diffraction patterns could be indexed with a pure monoclinic phase of WO₃ with lattice constants $a = 5.261 \text{ \AA}$, $b = 5.128 \text{ \AA}$, $c = 7.650 \text{ \AA}$, and $\beta = 92.05^\circ$ (JCPDS #88-0550). The thermographic images of the sensors were obtained with an infrared camera (SC5000, FLIR). The transmittance of the entire sensor structure was measured over the wavelength range 200–900 nm by UV/VIS spectrometry (Lambda 18, Perkin Elmer). NECR measurements were carried out using a nanomechanical test instrument (TI 750 Ubi, Hysitron). The gas sensing properties of the fabricated thin film sensors were measured without external heating. As the flow gas was changed from dry air to a calibrated test gas (balanced with dry air, Sinyang Gases), change in the sensor resistance was monitored using a source measurement unit (Keithley 236). A constant flow rate

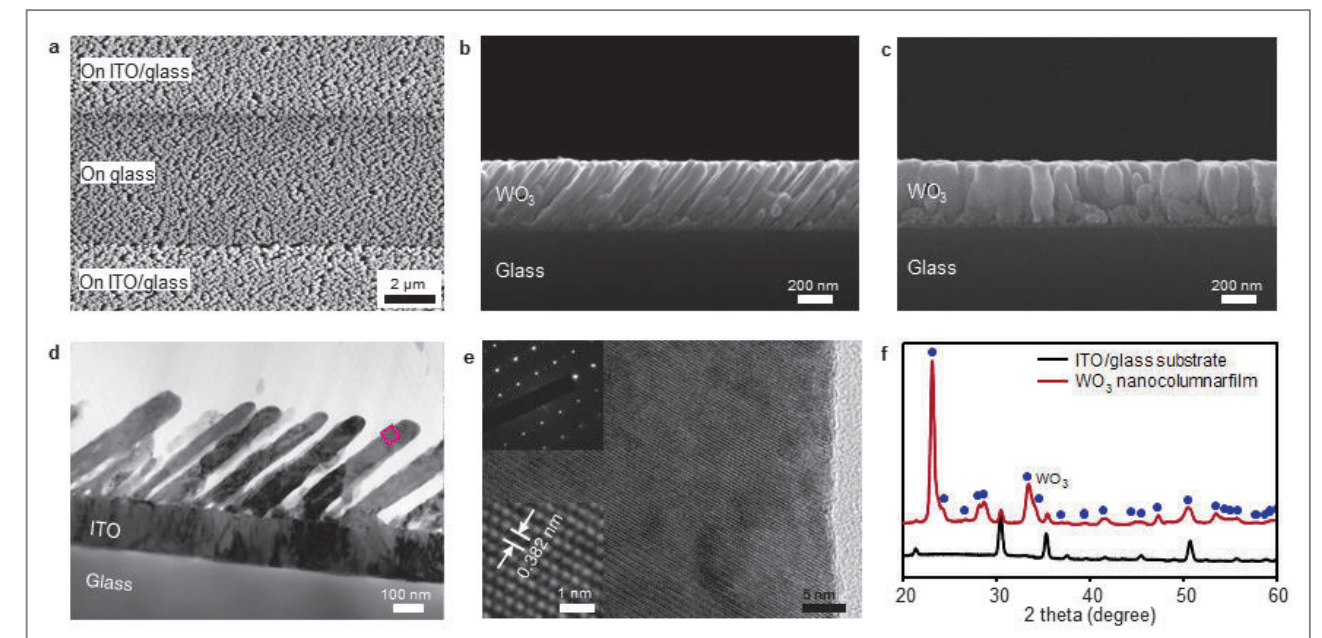


Figure 2. (a) Plain-view scanning electron microscopy (SEM) image of the nanocolumnar WO₃ film. (b,c) Cross-sectional SEM images of the nanocolumnar WO₃ film on glass (b) and along the ITO IDEs (c). (d) Transmission electron microscopy (TEM) image of WO₃ nanocolumns. (e) High-resolution TEM image of a WO₃ nanocolumn taken from the rectangular region. Inset: selected area diffraction pattern (top) and high-magnification TEM image of the interplanar spacings. (f) Glancing angle x-ray diffraction patterns of an ITO/glass substrate, and nanocolumnar WO₃ film on the substrate.

of 500 sccm was used for dry air and the test gas. The cross-sectional scanning electron microscopy (SEM) images show that all the individual nanocolumns were separated with pores near the surface (Figure 2a). In stark contrast, individual nanocolumns were connected and formed walls across the ITO IDEs (Figure 2c). The pores facilitated easy access of chemical molecules to the bottom of the film and the connected walls acted as paths for electrical current to flow through. The separation of individual nanocolumns along the ITO IDEs was confirmed, as shown by the cross-section transmission electron microscopy (TEM) image in Figure 2d. High-resolution TEM (Figure 2e) and X-ray diffraction (Figure 2f) show that each nanocolumn had high crystallinity and (002) was the preferred orientation, even though the overall film was polycrystalline.

Self-activation of dense-planar and nanocolumnar WO_3 thin film sensors was monitored by measuring resistance change with increasing applied voltage. Both devices displayed linear current-voltage characteristics, indicating ohmic behavior between the WO_3 films and ITO electrodes. When the applied voltage was increased from 0.1 V to 5 V, there was a decrease by a factor of 1.45 in sensor resistance, with time transient of 150 s for the conventionally prepared thin film sensor (Figure 3a). Thermographic images show that the increase in film temperature by self-activation was less than 2°C . For the same condition, the resistance of the nanocolumnar film decreased by two orders of magnitude with transient time of 120 s. The film temperature rose to 139°C due to self-activation (Figures 2b,c). The reduced resistance of the WO_3 film at higher temperatures reflects the semiconducting nature of WO_3 . The nanocolumnar thin film device exhibited approximately two orders of magnitude higher resistance than the conventional film at the applied bias voltage of 0.1 V, but due to the pronounced self-activation of the nanocolumnar film, both devices exhibited similar values of resistance under 5 V bias. Figure 2d shows a 40 μ -tilted SEM image of the nanocolumnar WO_3 film deposited between and on the

ITO IDEs. The porosity of the film was estimated to be 38% on the basis of the analysis of the black and white contrast. A closer look reveals that the nanocolumns were disconnected from each other at many points and that some current pathways in the film were established only along localized regions. Even percolating pathways often meander through narrow necks (20–40 nm in width). For this geometry, electron flow is constricted, leading to increased joule heating. Furthermore, ambient air in the pores, providing an excellent thermal barrier, suppresses heat dissipation laterally to the IDEs, while the small contact area between nanocolumns and glass substrate minimizes heat dissipation to the substrate. This is in contrast to large heat losses in conventional sensors, connected with the incorporation of independent heaters screen-printed or sputtered beneath the substrate or between the sensing film and the substrate. These findings clearly demonstrate that self-assembled nanocolumnar WO_3 films serve as very efficient self-activated microheaters with minimal heat loss and power consumption.

We measured the transmittance of the fabricated sensor. Figure 4 shows the total and specular

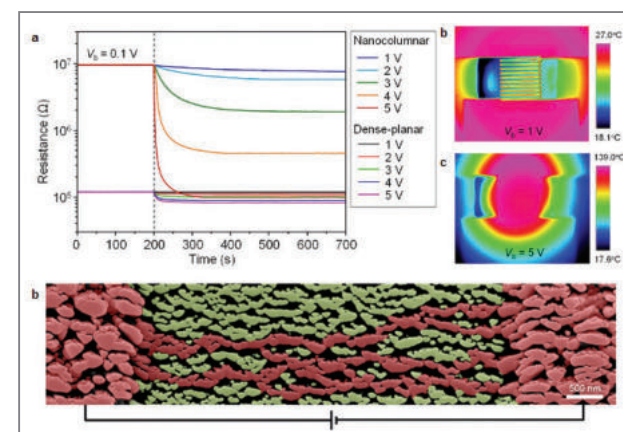


Figure 3. Self-activation. (a) Resistance-time characteristics with variation of applied bias voltage for dense-planar and nanocolumnar WO_3 thin film sensors. (b,c) Thermographic images showing temperature variation in the WO_3 thin film sensors with different bias voltages (V_b). (d) 40 μ -tilted SEM image of nanocolumnar WO_3 film between and on ITO IDEs. Parts highlighted in reddish color indicate localized current pathways which meander with narrow necks.

transmittance spectra of the nanocolumnar WO_3 film/ITO IDEs/glass structure from 200 nm to 900 nm. The longer onset wavelength of the spectra of the sensor as compared to that of the ITO/glass substrate is due to the smaller optical bandgap (E_g) of WO_3 (3.0 eV) compared to the E_g of ITO (3.9 eV). After averaging the oscillations in the spectrum due to optical interference effects, the total transmittance of the sensor over 450–900 nm was determined to be 90%, which is almost identical to the transmittance of the ITO/glass substrate. The response curve of the sensor, as shown in Figure 4 (inset), demonstrates its insensitivity to surrounding light signals, suggesting that the sensor can be used without being compromised by light.

Sensor resistance was measured under a DC bias voltage of 0.1–5 V. The response of the sensors ($\Delta R/R_0$ for NO_2 , $\Delta I/I_0$ for ethanol, acetone, SO_2 , NH_3 , H_2 , and CO) was accurately determined by measuring the baseline resistances of the sensors in dry air and the fully saturated resistances after exposure to the test gas. Gas flow was controlled using mass flow controllers, and all measurements were recorded on a computer through the use of LabVIEW over the GPIB interface. The current-voltage characteristics of the fabricated sensors were

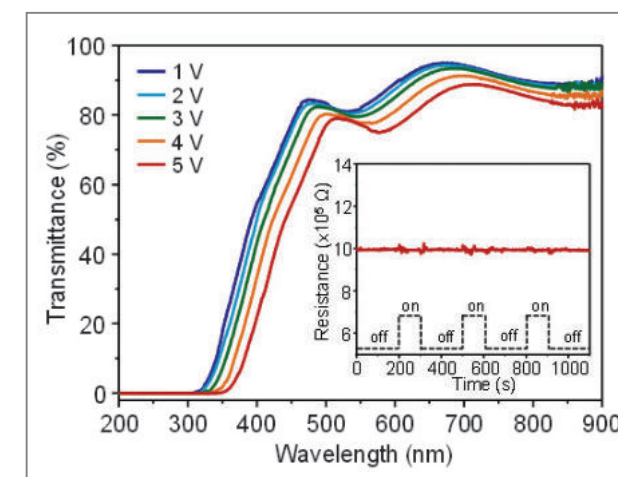


Figure 4. Bias-voltage-dependent specular transmittance spectra of the nanocolumnar WO_3 film/ITO IDEs/glass structure. Inset: response characteristic of the nanocolumnar WO_3 thin film sensor to office fluorescent light with a luminance of about 400 lx.

measured to check the contribution from the contact resistance between the ITO IDEs and WO_3 sensing film to overall performance. Figures 5a,b show responses of the plain and nanocolumnar WO_3 thin film sensors to 5 ppm NO_2 without external heating. The plain sensor exhibited higher response when the applied bias voltage was increased. However, the response (defined here as $\Delta R/R_0$ where R_0 and ΔR denote the initial resistance of the sensor in air and the resistance change of the sensor by exposure to the test gas, respectively) was as low as 0.15 at 5 V and the sensor did not show full recovery to the original resistance, which is analogous to chemical sensors based on carbon nanotubes or graphenes to NO_2 . The nanocolumnar sensor showed drastic enhancement in response with an increase in the bias voltage. At 5 V, the response was extremely high, about 450, which is the highest value ever reported for metal oxide thin film sensors, and the resistance fully recovered to its initial value. The linearly varied response of the nanocolumnar sensor to 1–5 ppm highlights the feasibility of using the sensor for detecting the concentration of the target gas (Figure 5c). By contrast, the response of the plain sensor was negligible.

To verify the significantly higher response of the nanocolumnar sensor compared to the plain sensor, the response to various gases such as NO_2 , $\text{C}_2\text{H}_5\text{OH}$ (ethanol), CH_3COCH_3 (acetone), NH_3 , H_2 , SO_2 , and CO was measured. For the plain sensor, the response ($\Delta I/I_0$ where I_0 and ΔI denote the initial current of the sensor in air and the current change of the sensor by exposure to the test gas, respectively) to acetone, NH_3 , H_2 , SO_2 , and CO was zero and the response to 5 ppm NO_2 and 50 ppm ethanol was lower than 0.2 (Figure 5d). In stark contrast, a high response to all the test gases was achieved from the nanocolumnar sensor. Especially for NO_2 and ethanol, the response was three orders of magnitude higher than that of the plain sensor. This high response of the nanocolumnar sensor is attributed to the combined effects of the self-heating, the porous nanostructure with high surface-to-volume ratio, and the presence of the narrow

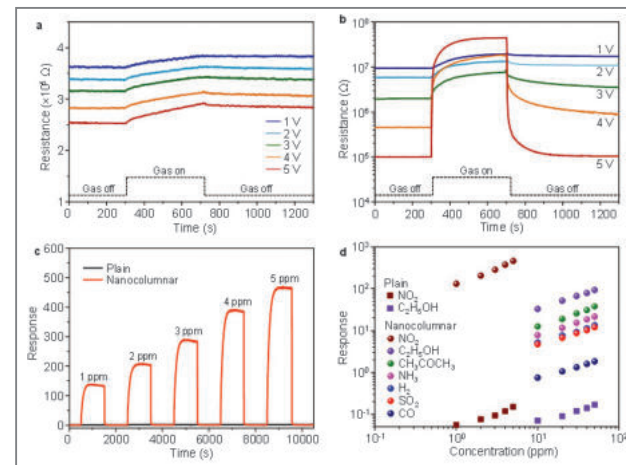


Figure 5. Gas sensing properties. (a,b) Typical response characteristics of the plain WO_3 thin film sensor (a) and the nanocolumnar WO_3 thin film sensor (b) to 5 ppm NO_2 . Measurements were carried out without external heating. (c) Response curves of the plain and nanocolumnar WO_3 thin film sensors to 1–5 ppm NO_2 . (d) Response of the plain and nanocolumnar WO_3 thin film sensors as a function of gas concentration for various target gases.

necks. Although an NO_2 concentration of 1 ppm was the lowest experimentally determined value, the theoretical detection limit (signal-to-noise ratio > 5) was calculated to be approximately 5 ppt (Figure 4e). This value is much lower than the ambient air quality standards (AAQS) of the European Union, the United States, and South Korea, which are several ppb levels (Figure 6a). For SO_2 and CO, the detection limits of the nanocolumnar sensor are lower than the AAQS levels, suggesting a potentially significant

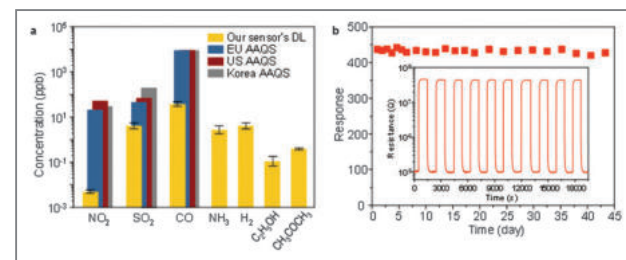


Figure 6. (a) Detection limits (DLs) of the nanocolumnar WO_3 thin film sensor to various gases. Ambient air quality standards (AAQS) of the European Union (EU), the United States (US), and Korea for NO_2 , SO_2 , and CO are presented for comparison. The averaging periods of AAQS for NO_2 , SO_2 , and CO are 1 year, 1 hour, and 8 hours, respectively. (b) Response changes of the nanocolumnar thin film sensor over 50 days. Inset: response characteristic of the sensor to 10 pulses of 5 ppm NO_2 .

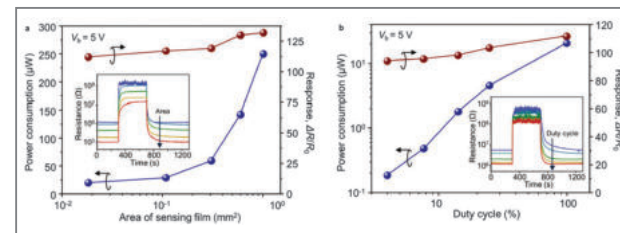


Figure 7. Power consumption and response time. Power consumption (a), response (a), and response time (b) of nanocolumnar WO_3 thin film sensors with different sensing area to 1 ppm NO_2 and 50 ppm $\text{C}_2\text{H}_5\text{OH}$. Inset: response characteristics of the 5 sensors to 1 ppm NO_2 .

application of the sensor for monitoring air quality.

Furthermore, detection limits of sub ppb levels to ethanol and acetone demonstrate the potential of the sensor for use in high performance volatile organic compound (VOC) sensors. Owing to a low working temperature ($\sim 140^\circ\text{C}$), the nanocolumnar sensor showed a very stable operation, as illustrated in Figure 6b. Chemical sensing with external heating confirmed that the working temperature of the sensor was lower than 150°C . Meanwhile, the temperature of the backside of the sensor was measured at 43°C during operation at an applied bias voltage of 5 V. Figure 7a shows power consumption of nanocolumnar sensors with different sensing areas. By reducing the area of WO_3 sensing film from 1 mm \times 1 mm to 100 μm \times 170 μm , the response of the sensors remained almost constant, while the power consumption of the sensors decreased from 251 μW to 21.6 μW . These values were much lower than the power consumption of the micromachined thin film sensors (10–200 mW) and comparable to those of single nanowire sensors (tens of μW). When the response of power consumption of the sensor with a 100 μm \times 170 μm sensing area was normalized with the power consumption, it exhibited incomparably superior performance to state-of-the-art MOS chemical sensors. In addition to lowering the power consumption, the reduction of the sensing area led to the enhancement of response speed in the sensors as shown in Figure 7b. From these results, we conclude that the nanocolumnar WO_3 thin film sensors are highly efficient

sensors which are ready to be embedded into portable devices.

Conclusion

We have successfully developed highly transparent chemoresistive sensors with ultrahigh response, extremely low power consumption, and excellent long-term stability by modifying the nanostructures of sensing films, which are easily self-heated with μA level current injection. The remarkable device performance we achieved broadens the application potential of MOS chemical sensors to transparent circuitries, transparent electronics and mobile devices. We believe that a very high performance, portable, electronic “nose” for selective chemical sensing can also be developed using our sensors and the described surface decoration technique. Our approach demonstrates a way to improve device performance significantly by removing heating elements, and instead, exploiting self-heating in solid-state devices such as sensors, fuel cells, and CO_2 splitting systems which must function at elevated temperatures to enhance chemical activities.

Original Article

This article and images are cited from “Self-activated ultrahigh chemosensitivity of oxide thin film nanostructures for transparent sensors” in *Sci. Rep.* 2, 588.

References

- [1] Cui Y, Wei QQ et al. *Science* 2001; 293: 1289-1292.
- [2] Sysoev W, Button BK et al. *Nano Lett.* 2006; 6:1584-1588.
- [3] Park JU, Nam SU et al. *Nat. Mater.* 2012;11: 120-125.
- [4] Prades JD, Jimenez-Diaz R et al. *Appl. Phys. Lett.* 2008; 93: 123110.

- [5] Choi KJ, Jang HW. *Sensors*. 2010; 10: 4083-4099.
- [6] Korotcenkov G, Brinzari V et al. *Thin Solid Films* 2005; 479: 38251.

Strain Evolution of Each Grain Type In Poly-Crystalline (Ba,Sr)TiO₃ Thin Films Grown by Sputtering



Jung-Hae Choi

Electronic Materials Research Center
choijh@kist.re.kr

Introduction

The mechanical properties of materials are fundamental material parameters and are generally represented by the relationship between strain (ϵ) and stress (σ). The ϵ and σ can also influence other fundamental material properties, such as electrical properties (piezoelectric effect) and defect distribution (piezochemical effect), as well as the mechanical response of materials. Perovskite-structured materials are a typical example of this correlation between different fundamental properties due to their high ionic polarizability. Many perovskite oxide thin films, such as (Ba,Sr)TiO₃ (BST), show a crucial influence of the ϵ and associated σ on the functionality of films, as evidenced by the dielectric constant, polarization, Curie temperature, and piezoelectric coefficient [1-10]. The strain can even transform the non-ferroelectric phase to the ferroelectric phase and vice versa [11].

The strain in thin films is induced by various intrinsic factors, such as the misfit strain and thermal expansion mismatch with the substrate, as well as extrinsic factors, such as the impurity/vacancy incorporation and shot-peening effect in sputtering [15]. In many cases, these factors simultaneously influence the strain state of the perovskite oxide films, which complicates attempts to reach a fundamental understanding of the influence of these factors on the properties of the films and often leads to disagreement between results and theoretical expectations.

The strain state of poly-crystalline film has a much more complicated

pattern due to the non-uniform structure and crystallographic direction of each grain. It appears that there are two fundamental questions regarding the strain status of poly-crystalline films: (1) what is the strain state of each grain, and is the strain state of each grain influenced by the strain state of neighboring grains? and (2) what is the defect (typically oxygen vacancy) concentration in each grain and does this have a certain relationship with the strain state of each grain? In this report, the authors attempted to answer these two important questions by adopting the X-ray diffraction (XRD) technique to poly-crystalline BST thin films with a thickness of 120 nm which were deposited on highly [111]-orientation preferred poly-crystalline Pt thin film electrodes by an rf magnetron sputtering technique at substrate temperatures (T_s) ranging from 338 to 505°C. Different T_s levels resulted in different film stress states; low and high T_s induced overall in-plane compressive and tensile stresses, respectively, due to the dominance of the shot peening effect (at low T_s) and the mismatch in the thermal expansion coefficients of Si substrate and BST film (at high T_s). In addition, BST films with thicknesses ranging from 29.6 to 155.8 nm were deposited at 505°C in order to understand the influence of film thickness on the stress and defect states of each grain. The strain state of each grain with different orientations was estimated by a careful XRD analysis using the $\sin^2\psi$ method. The results were compared with the expected strain-stress relationship from bulk compliance values. Semi-quantitative discussion of the reason for the evolution of different stress-strain states based on the crystal structure of the perovskite material is presented below.

Results

First, the influences of T_s on the structural properties of BST films are discussed. For the most part, the films were slightly Ti-rich (Ti/(Ba+Sr+Ti) ~ 0.52) and Ba-deficient (Ba/(Ba+Sr) ~ 0.48) and showed relatively random growth

directions with (110), (111) and (002) peaks. Although the diffraction peak intensity generally increased with increasing T_s , suggesting better crystalline quality and less mosaicity, the relative peak intensity ratio did not vary significantly. The peak position generally shifted into the high 2θ direction as T_s increased, suggesting that the films underwent more in-plane tensile stress due to the thermal expansion mismatch between the BST and Si substrate during the cooling down period after film deposition. Detailed strain evolutions for each grain type in the different films were examined by the $\sin^2\psi$ method. Here ψ is the angle between the direction normal to the film surface and the direction of the specific crystallographic orientation where the inter-planar spacing was measured.

Figures 1a-d show the variations in the lattice parameters of the Pt electrode film, [111]-, [110]-, and [002]-oriented BST grains as a function of $\sin^2\psi$ for the BST films grown at different T_s .

Figures 2a-d show the variations in the ϵ_0 and ϵ_z values as well as the variation of the effective Poisson's ratio, ν ($= -\epsilon_z/\epsilon_0$), of the Pt film and those of the three differently oriented BST grains as a function of T_s . In this paper, the positive and negative strains denote the tensile

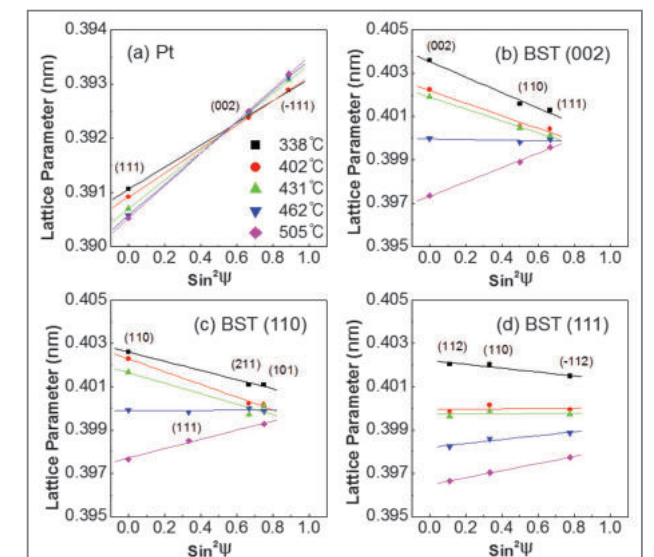


Figure 1. Variations in the lattice parameters of (a) Pt electrode film, (b) [002]-, (c) [110]-, and (d) [111]-oriented BST grains as a function of $\sin^2\psi$ for the BST films grown at different T_s .

and compressive strains, respectively. The Pt film had only [111]-oriented grains and showed in-plane positive strain at all T_s due to the thermal expansion mismatch with Si. However, the BST films showed a complicated development of strains depending on the T_s and types of grains. The [002]- and [110]-oriented grains grown at 505°C showed in-plane positive strain, but the same type of grains grown at lower T_s showed in-plane negative strains. The cross-over from the positive to negative strain state near the transition temperature, further changes in the negative strain associated with the [002]-oriented grains developed rather slowly as T_s decreased. However, that of [110]-oriented grains was more complicated and not yet clearly understood. In addition, the magnitudes of ε_0 and ε_z were symmetric and generally high in [002]-oriented grains due to higher compliance (S_{11}) and high ν along the [002] direction [11,12]. Nevertheless, ε_0 and ε_z were rather asymmetric in [110]-oriented grains along the tensile and compressive directions probably due to the different crystallographic structures. [111]-oriented grains also showed in-plane positive strain at the highest T_s but with a smaller magnitude of in- and out-of-plane strains. Interestingly, the transition into the negative strain state occurred at a much lower T_s (~ 400°C). Therefore,

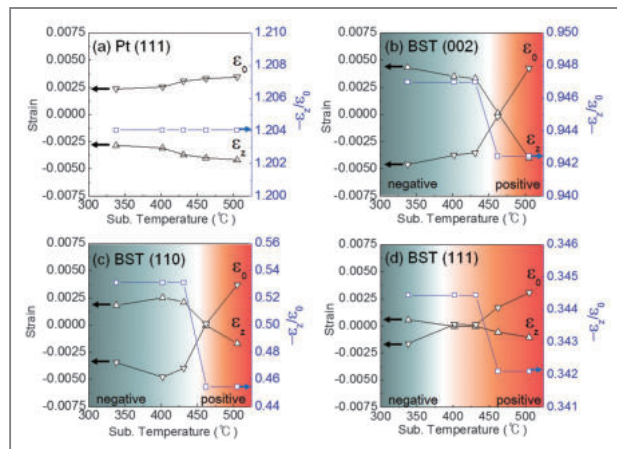


Figure 2. Variation of in-plane and out-of plane strain as a function of substrate temperature of (a) [111]-oriented grain of Pt, and those of (b) [002]-, (c) [110]-, and (d) [111]-oriented grains of (Ba,Sr)TiO₃ thin films.

the [111]-oriented grains demonstrated an in-plane negative strain state only at the lowest T_s with a much smaller magnitude of ε_0 and ε_z . In this case, the magnitude of ε_z was generally smaller than that of ε_0 . The variations in ν appear to be related to the strain state reflected in Figure 2 (b) and (c), but this is not the case in Figure 2 (d). Such variations in ν were actually related to the change in the Ba/Sr ratio with varying T_s , thus, a relative comparison with theoretically calculated values for a given Ba/Sr ratio can provide meaningful insights, as discussed below.

The in-plane tensile stress in BST grains can generally be understood from the thermal expansion mismatch between the film and Si substrate. The higher in-plane tensile stress state at higher T_s can be understood from the thermal effect. The in-plane compressive stress in sputtered films can be understood from the shot-peening effect [15]. Therefore, the increasing in-plane negative strain with decreasing T_s can be understood from the domination of the ion bombardment effect of the sputtering process over the thermal expansion mismatch. Given the low compliance along the [111] direction of the perovskite BST material, the out-of-plane strain (ε_z) of the [111]-oriented grains must be smallest at the lowest T_s (338°C), which was indeed the case as shown in Figure 2 (d). The same argument can be applied to the in-plane tensile cases; out-of-plane negative strain along the [111] direction was quite small at 505°C due to the lower in-plane tensile strain at the same temperature compared to other types of grains. In addition, the lower evolution of compressive stress by the larger decrement of the shot-peening effect in [111]-oriented grains compared to the grains with different orientations decreased the transition temperature from ~ 460 to ~ 400°C.

In order to confirm whether the different responses of each grain type to external stress coincide with the bulk properties of the material, ν under biaxial stress was calculated for the different orientations of the crystals where in-plane biaxial stress (σ_0) was applied to the isolated [111], [110], and [002]-oriented grains and the results were compared with the experimental

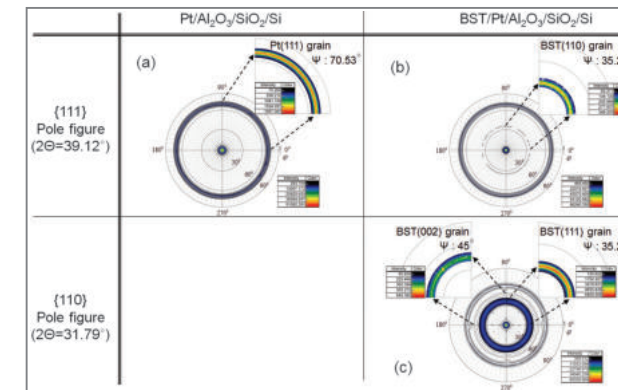


Figure 3. (a) [111] pole figure of Pt substrate, (b) [111] pole figure, and (c) [110] pole figure of (Ba,Sr)TiO₃ thin films.

results. It should be noted that each grain type must have a completely random in-plane orientation for this comparison to be valid, which was indeed the case for [111]- and [002]-type grains but not for [110]-type grains (Figure 3).

For the [002]-oriented grains, the measured ν 's were generally larger than the theoretically calculated values. In contrast, the measured ν 's of the [110]- and [111]-oriented grains were smaller than the theoretical values. Such a discrepancy between the theoretical and measured values of the ν 's and different relative tendencies suggests that the differently-oriented grains experienced a significant mechanical confinement effect due to the densely packed columnar microstructure, and that the smaller strain of the [110]- and [111]-oriented grains to the external biaxial stress was compensated for by the larger strain of the [002]-oriented grains.

Figure 3 shows the pole figures of [111]-oriented Pt electrode, [110]-oriented BST grains, and [111]- and [002]-oriented BST grains. A randomness of the in-plane distribution for the [111]- and [002]-oriented grains was observed. However, the [110]-oriented grains had a significantly more non-random in-plane orientation compared to the other cases, which might be related to the highly anisotropic nature of the crystallographic directions on the (110) plane. This may explain the peculiar variations in ε_z and ε_0 of this type of grain, as

shown in Figure 2c.

The different mechanical responses of the different types of grains, shown in Figure 2, can be understood from calculated compliance values and the Poisson's ratio along the different directions of the bulk crystal. The absolute value of the out-of-plane compliance along the [111] is the smallest and that along the [002] is the largest. One possible reason for such a discrepancy is the potential distortion of the TiO₆ octahedra.

Next, the oxygen vacancy concentrations of each type of grain were considered, based on the fact that the lattice parameter of oxygen-deficient bulk BST material is determined by the oxygen vacancy concentration. Figure 4 shows the variation in the measured a_0 of the differently-oriented BST grains as well as the Pt as a function of T_s . There were three notable findings. First, the measured a_0 was generally much larger than the bulk lattice parameter with the same cation composition. Second, the a_0 for each type of grain generally decreased at different rates as T_s increased. Third, the a_0 for each type of grain was not the same.

The larger a_0 values for the various types of grains

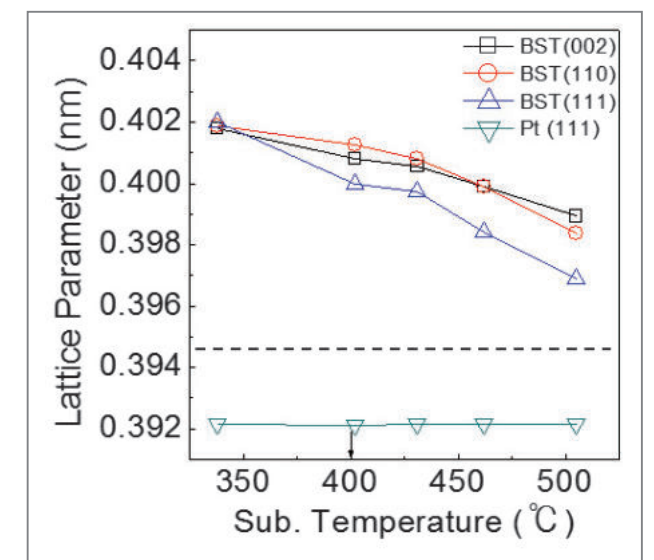


Figure 4. Variation in the measured unstrained lattice parameter, a_0 , of the differently-oriented (Ba,Sr)TiO₃ grains as well as the Pt as a function of substrate temperature. Dashed line indicates the bulk value of (Ba,Sr)TiO₃.

in BST thin film correspond to higher oxygen vacancy concentrations [13]. The different a_0 values of the BST grains with different orientations suggest that the oxygen vacancy concentration is also different. The different variations in a_0 for the three types of grains with increasing T_s are understood as follows. The almost identical a_0 at a T_s of 338°C suggests that the vacancy concentration is largely determined by the knocking-out effect during the sputtering process. As the T_s increases, the thermal healing effect appears to work and the vacancy concentration generally decreases. The faster healing effect of the [111]-oriented grains can be ascribed to the larger surface area of this type of grain which enhances the vacancy annihilation during growth at a higher T_s . At lower T_s , the more obscure evolution of grain morphology of the different grains makes this difference less evident, and thus the vacancy healing effect must be averaged out.

Figure 5 shows the effects of film thickness (t_f) on the evolution of the strains for the films grown at 505°C. Figures 5a-c show the variations in the ϵ_0 and ϵ_z values as a function of the t_f for the three differently-oriented grains. The ϵ_0 and ϵ_z values generally decreased with increasing t_f . However, the overall difference between

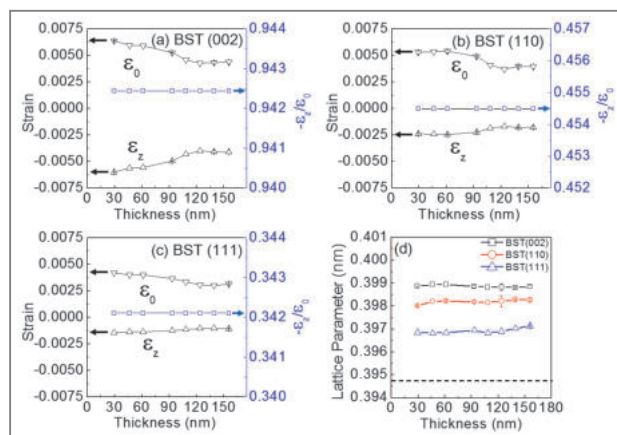


Figure 5. Variation of in-plane and out-of plane strain as a function of film thickness for the cases of (a) [001]-, (b) [110]-, and (c) [111]-oriented grains of the (Ba,Sr)TiO₃ thin films, and (d) comparison of lattice parameter (Ba,Sr)TiO₃ grains with different orientations. Dashed line indicates the bulk value of (Ba,Sr)TiO₃.



Lab photo; Linux Clusters ~7 teraflops

the different types of grains was almost identical to that shown in Figure 2; the strain of [002]-oriented grains was symmetrical and largest while that of [111]-oriented grains was asymmetrical and smallest. Figure 5d shows the variations of unstrained lattice parameter (a_0) for the different types of grains as a function of t_f . The a_0 for each type of grain was almost independent of the t_f but highly dependent on the type of grain. This means that the overall oxygen vacancy concentration is not dependent on t_f while the strain is dependent on it. The most striking result of our work, revealed from a detailed X-ray study of these ionic crystalline materials, is the presence of a different oxygen vacancy concentration in each type of grain. Another unexpected finding is that the oxygen vacancy concentration has nothing to do with the strain state of each grain.

It is believed that this work has opened a new approach to understanding the mechanical and chemical nature of poly-crystalline thin films. It is important to note that there could be many other thin film systems that show different levels of mechanical interactions between

the grains, but these too could be checked by the same X-ray technique. It is hoped that this technique can be more widely applied to many other poly-crystalline material systems in order to shed light on the mechanical and chemical nature of different grains.

Note

This article and images are cited from “Strain evolution of each type of grains in poly-crystalline (Ba,Sr)TiO₃ thin films grown by sputtering” in *Scientific Reports* 2012; 2: 939.

References

- [1] Choi KJ. et al. *Science* 2004; 306: 1005.
- [2] Lee HN, Hesse D, Zakharov N, Gösele U. *Science* 2002; 296: 2006.
- [3] Wang J et al. *Science* 2003; 299: 1719.
- [4] Neaton JB, Rabe KM. *Appl. Phys. Lett.* 2003; 82: 1586.
- [5] Pertsev NA, Zembilgotov AG, Tagantsev AK. *Phys. Rev. Lett.* 1998; 80: 1988.
- [6] Uwe H, Sakudo T. *Phys. Rev. B.* 1976; 13: 271.
- [7] Pertsev NA, Kukhar VG, Kohlstedt H, Waser R. *Phys. Rev. B.* 2003; 67: 054107.
- [8] Ban Z-G, Alpay SP. *J. Appl. Phys.* 2003; 93: 504.
- [9] Chang W, Gilmore CM, Kim W-J. *J. Appl. Phys.* 2000; 87: 3044.
- [10] Pertsev NA, Zembilgotov AG, Hoffmann S, Waser R, Tagantsev AK. *J. Appl. Phys.* 1999; 85: 1698.
- [11] Nix WD. *Metall. Trans.* 1989; 20A: 2217.
- [12] Nye JF. *Physical Properties of Crystals*, Oxford University Press, London. 1957.
- [13] Kim WJ, Chang W, Qudri SB, Pond JM, Kirchoefer SW, Chrisey DB, Horwitz JS. *Appl. Phys. Lett.* 2000; 76: 1185.

[Technical Review]

Organic Semiconductors for High Performance Ambipolar Field Effect Transistors



Bongsoo Kim

Photo-electronic Hybrids Research Center
bongsoo@kist.re.kr

Since the first polythiophene field-effect transistor (FET) was introduced in 1986, the development of new high performance conjugated polymer semiconductors has been a hot issue in scientific and industrial communities. These semiconductors have multiple advantages over their inorganic counterparts; for example, they can be synthesized with low-cost materials and are solution-processable, allowing a roll-to-roll process and low-cost, high-throughput production. Therefore, they are particularly suitable for large-area low-cost electronic device applications, such as flexible displays, radiofrequency identification (RF-ID) tags, memory devices, and sensors [1]. Moreover, they have already exhibited promising high carrier mobilities, even higher than amorphous silicon semiconductors.

The basic device structure of a polymer FET is shown in Figure 1. FETs comprise a thin semiconducting layer, a gate electrode positioned under the insulating gate dielectric, and source/drain electrodes that are in contact with the semiconducting layer and are separated by a channel length (L) and width (W). Source/drains can be positioned either on top of the semiconductor or below it. A self-assembled monolayer (SAM) is often employed to passivate the SiO_2 dielectric.

Figure 2 shows the relationship among materials, carrier mobility, and applications. To expand the use of polymer FETs, intense research efforts have been devoted to improving carrier mobilities. Various conjugated polymers have been synthesized over the past decades and have shown significant mobility enhancement, particularly in developing p-type

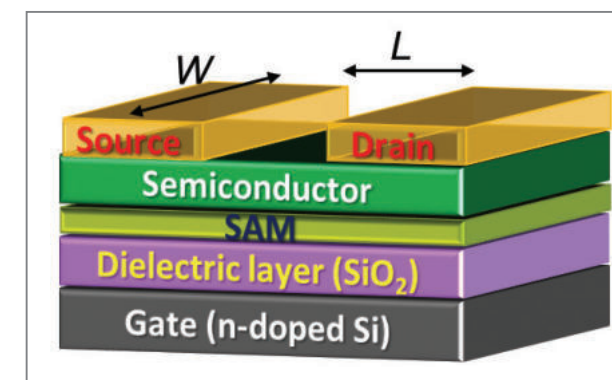


Figure 1. Basic device structure of a polymer FET.

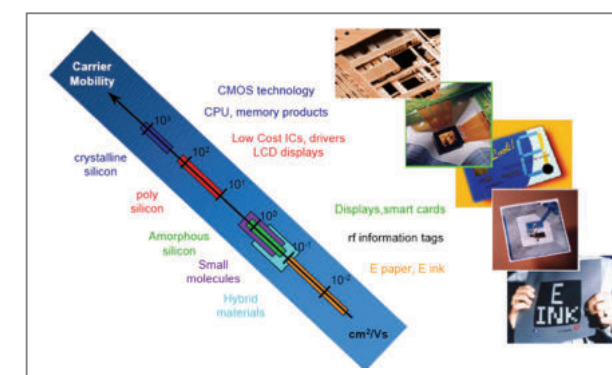


Figure 2. Materials, carrier mobility, and applications.

conjugated polymers. Conjugated polymers can be categorized by a monomeric structure. Representative donor-acceptor-type polymer structures are shown in Figure 3. The first category includes thiophene-based polymers. These polymers consist of series-connected thiophene rings with side alkyl chains. Representative polymers include poly(3-hexylthiophene) (P3HT), poly[5,5'-bis(3-dodecyl-2-thienyl)-2,2'-bithiophene] (PQT), and poly-(2,5-bis(3-alkylthiophene-2-yl)thieno[3,2-b]thiophenes) (pBTTTs), and they have exhibited hole mobilities of 0.1–0.6 $\text{cm}^2\text{V}^{-1}\text{s}^{-1}$. The second category is called donor-acceptor type polymers. These polymers consist of electron-rich donor and electron-deficient acceptor moieties with side alkyl chains (Figure 4). Donor moieties commonly comprise oligothiophenes, fused thiophenes, and selenophenes; acceptor moieties comprise isoindigos, diketopyrrolopyrroles,

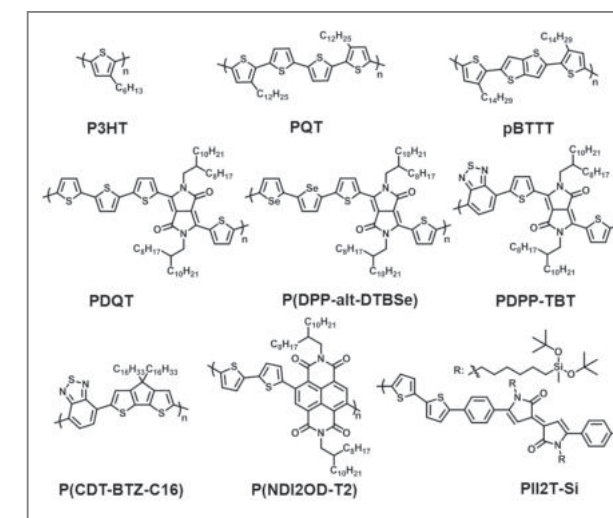


Figure 3. Chemical structures of polymers.

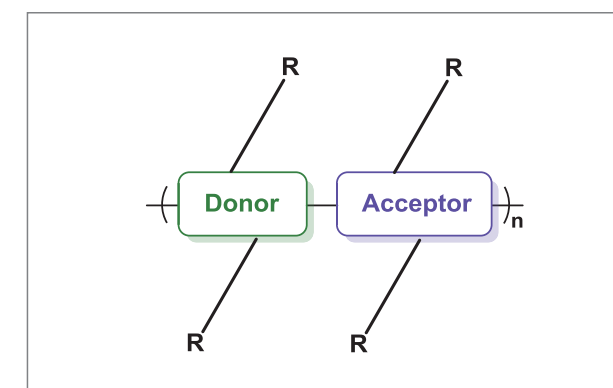


Figure 4. Basic structure of donor-acceptor type polymers. The polymers consisted of electron-rich donor (Donor) and electron-deficient acceptor (Acceptor) moieties with side alkyl chains (R).

benzothiadiazoles, and naphthalenedicarboximide. Recently, several research groups achieved higher carrier mobilities of 0.6–3.3 $\text{cm}^2\text{V}^{-1}\text{s}^{-1}$ from donor-acceptor-type low band gap polymers. The more impressive carrier mobilities have been achieved by a careful combination of side alkyl chains, donors, and acceptors in the polymer structure. First, side alkyl chains endow polymers with solubility, and facilitate the self-organization of polymer chains in the film state. Optimal alkyl chain lengths and proper interdistance between alkyl chains are important to form polymer lamellar structures via the interdigitation

of side alkyl chains. Second, the chemical structures of donor and acceptor moieties play a pivotal role in forming the polymer backbone and energy level alignment. Planar polymer backbones generally promote close interchain π - π stacking and support orbital overlapping between the donor and acceptor units. Both interchain and intrachain electronic communication profoundly affects the positions of highest occupied molecular orbital (HOMO) and lowest unoccupied molecular orbital (LUMO) levels of the polymers with respect to contact metal Fermi levels, and in turn determines the main carrier type, mobility, and contact resistance.

In addition to the issue of carrier mobility enhancement, fabrication of complementary metal oxide semiconductor (CMOS)-like inverters using semiconducting polymers has become an important research topic. To realize CMOS-like inverters, it would be more beneficial to use single-component ambipolar transistors rather than a combination of p- and n-channel transistors. Low band gap polymers are a good candidate for ambipolar transistors because both their HOMO and LUMO levels lie close to the Fermi levels of source/drain contact metals. However, low band gap polymers have rarely exhibited ambipolar behavior. For further improvement in both carrier mobility and the hole/electron transport balance in ambipolar transistors, it is crucial to understand the dependence of transistor behavior on polymer chemical structure by exploring a conjugated polymer with a systematic change of the polymer aromatic backbone structure and side alkyl chains.

In this article, we present the FET performances of diketopyrrolopyrrole (DPP)-based polymers that we have studied recently [1,2]. Synthesis and chemical structures of the DPP polymers are shown in Figure 5. We varied aromatic ring structures in the donor and side alkyl chains in the acceptor. The three kinds of aromatic rings used in our investigations were thiophene-naphthalene-thiophene (T2NAP), terthiophene (T3), and thiophene-thienothiophene-thiophene (T2TT) and the two kinds of side alkyl chains were 2-hexyldecyl (HD) and

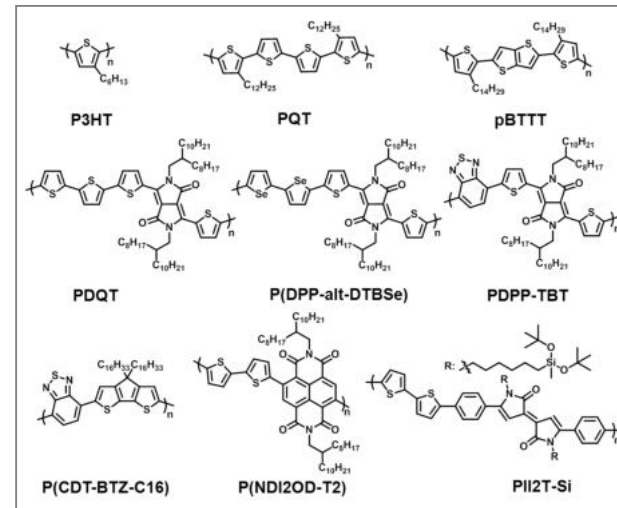


Figure 5. Polymer synthetic routes and chemical structures of polymers.

2-octyldecyl (OD). The naphthalene (NAP), thiophene (T), and thienothiophene (TT) units were conjugated and planar, and they provided closely stacked crystalline lamella-like microstructures. Such units also introduced sufficient spacing between alkyl chains to facilitate alkyl chain interdigitation. On the other hand, the dihedral angles between those units and neighboring thiophenes were expected to be different. Thus, an interesting aspect of the research was to find the dihedral angle dependence on the TFT performance for a given alkyl chain. Moreover, those two alkyl chains with different lengths would provide us with controllability over processability and film morphology since the longer alkyl chains generally make polymers more soluble. Given these variables of the polymer backbone planarity and alkyl chain length, the charge transport behavior in these polymers was investigated by fully characterizing the polymer films using UV-visible spectroscopy, cyclic voltammetry, grazing-incidence X-ray diffraction (GIXD), and density functional theory calculations. This work demonstrates the good correlation between chemical structure, film crystallinity, and carrier mobility.

Low band polymers of pDPPT2NAP-HD, pDPPT2NAP-OD, pDPPT3-HD, pDPPT3-OD, pDPPT2T-

HD, and pDPPT2TT-OD were synthesized by Suzuki or Stille polymerization (Figure 5). Their electronic properties were examined by UV-visible absorption spectroscopy and cyclic voltammetry. Figure 6 shows the UV-visible absorption spectra and energy diagram of polymer HOMO and LUMO levels. pDPPT2NAP-HD and pDPPT2NAP-OD polymers absorbed photons across a wide spectral range that extended to ~ 900 nm (Figure 6a,b). pDPPT2NAP-OD polymer showed a slight (~ 15 nm) red-shifted light absorption and strong main peak absorption compared to the pDPPT2NAP-HD, indicating that pDPPT2NAP-OD polymer chains carrying the longer alkyl chains were more closely stacked. After annealing polymer films at 25, 100, 150, and 200°C for 30 min, the absorption peak red-shifted as the annealing temperature increased. This observation indicated that thermal energy promoted self-organization of the polymer chains. Figure 6c shows UV-visible absorption spectra of pDPPT3-HD, pDPPT3-OD, pDPPT2TT-HD, and pDPPT2TT-OD. Compared to T2NAP-containing polymers, T3 and T2TT-containing polymers showed increasingly broader absorption bands. This is mainly due to the backbone planarity, which facilitates the polymer interchain packing and the narrowing of the polymer band gap. The

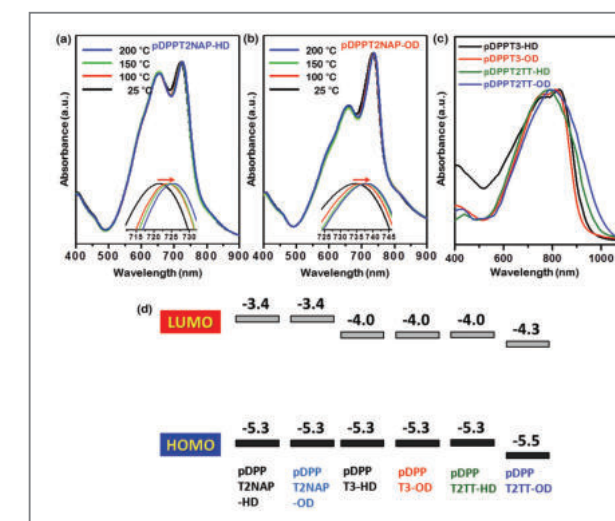


Figure 6. UV-visible absorption spectra and HOMO/LUMO energy levels of polymers. Energy unit: eV.

backbone planarity is in the order of T2NAP < T3 < T2TT (details are further discussed below). The dependence of energy levels on the backbone structure can be deduced from the energy diagram in Figure 6d. Interestingly, the naphthalene moiety limits conjugation to some degree and the LUMO levels of T2NAP-containing polymers are higher than the rest of the polymers by 0.6 eV. Meanwhile, T3 and T2TT-containing polymers showed similar energy levels because their polymer backbones are quite planar. This fact again supports that the conjugation is more limited by the backbone twisting between thiophenes and naphthalene units in the T2NAP-containing polymers. Interestingly, pDPPT2TT-OD polymer had the lowest HOMO and LUMO levels because its crystallinity is the highest among the polymers. In-depth study on the polymer chain packing and polymer backbone planarity were conducted and are further discussed below. We note that the energy levels of the polymers are suitable for ambipolar FETs.

Bottom-gate top-contact polymer FETs were used to evaluate the electrical properties of the polymers as a function of the branched alkyl chain length and thermal annealing temperature. Figure 7a,b depict the drain current (I_D)-gate voltage (V_G) characteristics at a fixed drain voltage (V_D) of -80 V for PFET devices based, respectively, on pDPPT2NAP-HD and pDPPT2NAP-OD films annealed at various temperatures, and with Au source/drain contacts. The transistors exhibited typical ambipolar behavior in hole-enhancement ($V_D = -80$ V) and electron-enhancement ($V_D = +80$ V) mode operations. The carrier mobilities of each PFET were calculated in each respective saturation regime using the relationship $I_D = C_i \mu W (V_G - V_{th})^2 / 2L$, where W and L are the channel width and length, respectively, C_i is the specific capacitance of the gate dielectric (11 nF/cm 2), V_{th} is the threshold voltage, and μ is the carrier mobility. Polymer FETs based on as-cast pDPPT2NAP-HD showed hole and electron mobilities of 0.037 and 0.023 cm 2 V $^{-1}$ s $^{-1}$, respectively. In contrast, PFETs based on as-cast pDPPT2NAP-OD with longer branched alkyl chains yielded higher

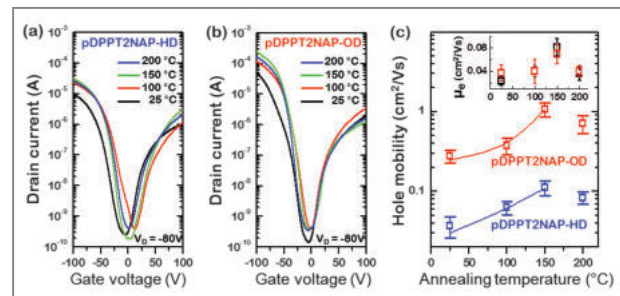


Figure 7. Transfer characteristics at a fixed V_D of -80 V for PFETs based on: (a) pDPPT2NAP-HD and (b) pDPPT2NAP-OD films annealed at various temperatures: 25, 100, 150, and 200 °C. (c) Hole and electron mobilities of the pDPPT2NAP-HD and pDPPT2NAP-OD PFETs as a function of the annealing temperature. Electron mobilities are shown in the inset.

hole and electron mobilities of 0.28 and 0.037 $\text{cm}^2\text{V}^{-1}\text{s}^{-1}$, respectively. Thermal annealing of the polymer films at 100 or 150 °C resulted in a significant increase in carrier mobility, as shown in Figure 7c. The average hole mobilities of the PFETs were 0.11 and 1.1 $\text{cm}^2\text{V}^{-1}\text{s}^{-1}$ for the 150 °C-annealed pDPPT2NAP-HD and pDPPT2NAP-OD, respectively. The PFETs based on pDPPT2NAP-OD carrying longer alkyl side chains were highly responsive to the annealing temperature.

In a similar manner, pDPPT3-HD, pDPPT3-OD, pDPPT2TT-HD, and pDPPT2TT-OD polymers showed superior ambipolar behavior and more dramatic mobility improvement upon annealing. Figure 8a,c summarizes the mobilities of the polymer FETs and Figure 8b,d shows the crystallinity enhancement upon thermal annealing. After film annealing at 150 °C for 30 min, the average hole mobilities of pDPPT3-HD, pDPPT3-OD, pDPPT2TT-HD, and pDPPT2TT-OD polymer FETs were 0.3, 1.57, 0.79, and 1.93 $\text{cm}^2\text{V}^{-1}\text{s}^{-1}$, respectively, and the average electron mobilities of pDPPT3-HD, pDPPT3-OD, pDPPT2TT-HD, and pDPPT2TT-OD polymer FETs were 0.12, 0.18, 0.04, 0.06 $\text{cm}^2\text{V}^{-1}\text{s}^{-1}$, respectively. The polymers carrying the longer alkyl chains of ODs showed higher hole mobilities than the corresponding (i.e., the same-backboned) polymers carrying the shorter alkyl chains of HDs. All of these electrical characteristics of PFETs as a function of alkyl chain length and annealing temperature were

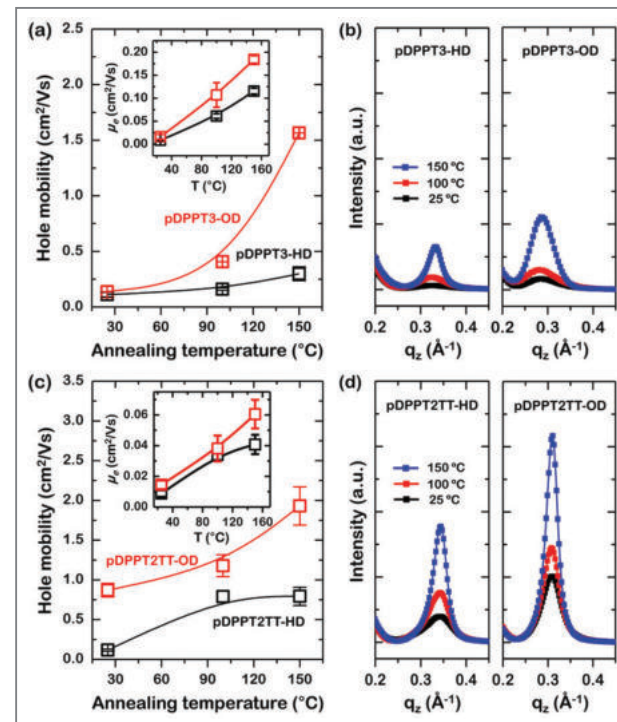


Figure 8. (a) Hole mobilities of polymer FETs based on ambipolar pDPPT3-HD and pDPPT3-OD films as a function of the annealing temperature. The inset shows the changes in the electron mobility. (b) The enlarged (100) Bragg peaks of the XRD pattern of pDPPT3-HD and pDPPT3-OD films. (c) Hole mobilities of PFETs based on ambipolar pDPPT2TT-HD and pDPPT2TT-OD films as a function of the annealing temperature. The inset shows the changes in the electron mobility. (d) The enlarged (100) Bragg peaks of the XRD pattern of pDPPT2TT-HD and pDPPT2TT-OD films.

strongly associated with the evolution of the crystalline structures of the semiconducting polymers that were confirmed by following GIXD studies.

Crystalline structures of polymer films were characterized using synchrotron 2D GIXD measurements. Figure 9a shows the 2D GIXD patterns of the pDPPT2NAP-OD films, a representative polymer for all the polymers presented here, demonstrating the evolution of crystallinity and the orientation of polymer crystalline domains. The x coordinate indicates the probing beam direction parallel to the substrate (in-plane), and the z coordinate indicates the direction normal to the substrate (out-of-plane). pDPPT2NAP-OD polymers showed intense (100)

reflections with higher order peaks along the q_z direction and (010) reflections along the q_y direction. The (010) diffraction peaks were very weak along the q_z direction for both films. This observation indicates that the alkyl side chains were aligned along the normal to the substrate, and the polymer backbones were essentially parallel to the substrate. This molecular orientation was particularly favorable for charge transport through the π - π stacks in the PFETs, such that the drain current flowed along the semiconducting channel parallel to the substrate. The out-of-plane spacings of the ordered pDPPT2NAP-OD phases were 20.0 Å, respectively, estimated from the spacing between the (h00) peaks. A comparison of these spacings to the fully extended polymer widths, i.e., two alkyl side chain lengths plus the aromatic backbone width, suggested that the side chains of the polymer were interdigitated or tilted out of the polymer backbone plane. Upon annealing, higher-order diffraction peaks and much weaker diffuse scattering intensities around the (h00) diffraction peaks along the Debye rings were observed. The higher order diffraction peaks and a narrower orientation distribution in the pDPPT2NAP-OD upon annealing indicated that thermal energy promoted polymer chain ordering and crystalline domain formation, which favors charge transport. This characteristic applies to all the rest of the polymer films, and the polymers with longer alkyl chains generally produced longer-range

upright crystalline plane orientations (see Figure 9b). Thus, we concluded that side long alkyl chains were critical to the control over film crystallinity and orientation, and thus carrier mobilities of the longer alkyl chained polymers were always higher than those of the corresponding shorter alkyl chained polymers.

We also found that the distance between alkyl chains in the polymer backbone plays a crucial role in forming interdigitated lamellar structures. For instance, for a given OD alkyl chain, the out-of-plane spacings of the ordered polymer lamella were calculated to be 20.0 Å, 21.1 Å, and 23.6 Å for pDPPT2NAP-OD, pDPPT2TT-OD, and pDPPT3-OD, respectively. Longer distances between alkyl chains, as were observed in pDPPT2NAP-OD or pDPPT2TT-OD films, provided more room for interdigitation/packing of the branched alkyl side chains and more efficient space filling in the q_z direction, which facilitated crystallization of the polymers.

Combining the GIXD results and conducting density function theory (DFT) calculations allowed us to find another crucial factor: the torsional angle between backbone aromatic rings. The simplified backbone structures of T-DPP-T-NAP-T, T-DPP-T-T-T, and T-DPP-T-TT-T (representing pDPPT2NAP-OD, pDPPT2TT-OD, and pDPPT3-OD, respectively) were geometrically optimized to an energy minimum using Gaussian 09 at the DFT B3LYP level with the 6-31+G(d,p) basis set. To expedite the calculation, alkyl chains were shortened to methyl groups on the DPP nitrogen. Figure 10 shows the energy levels of the frontier orbitals, their surface plots, and geometric models of their structures. The DFT results offered an explanation for why the band gap found in the UV-visible spectra increased in the order of pDPPT3-OD, pDPPT2TT-OD, and pDPPT2NAP-OD. More importantly, the geometrical information from the DFT calculations supported the correlation between the carrier mobility and the π - π stacking distance since the carrier hopping through π - π stacking is a mobility-determining step. The bottom figures in Figure 10 show that the torsional angles of φ_1 and φ_2 were similar for T-DPP-T-T-T and T-DPP-T-

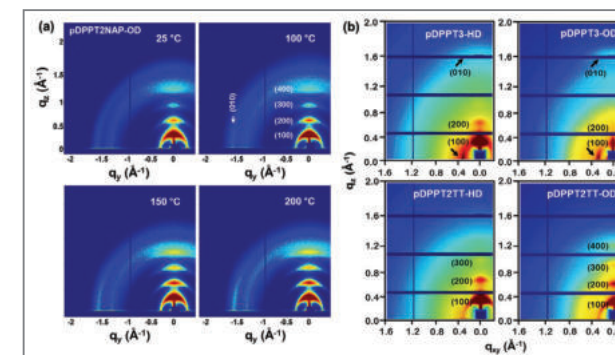


Figure 9. 2D GIXD patterns: (a) pDPPT2NAP-OD films annealed at temperatures of 25, 100, 150, and 200 °C; and (b) pDPPT3-HD, pDPPT3-OD, pDPPT2TT-HD, and pDPPT2TT-OD films annealed at 100 °C.

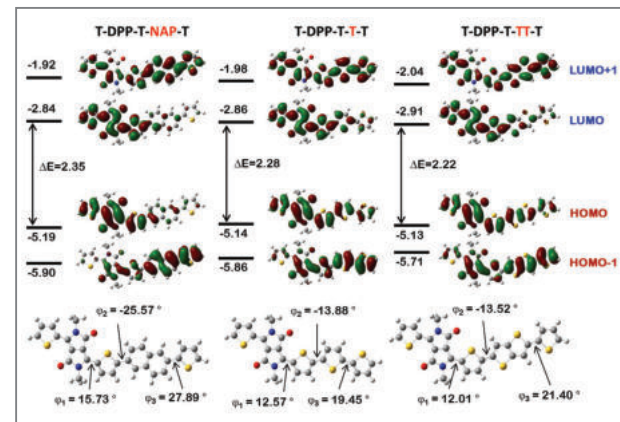


Figure 10. Energy levels and surface plots of frontier orbitals (top) and torsional angles (bottom) for model molecules representing polymer-repeating units. Energy unit is eV.

TT-T ($\varphi_1 \approx 12^\circ$ and $\varphi_2 \approx 14^\circ$), whereas the angles were higher in T-DPP-T-NAP-T ($\varphi_1 \approx 16^\circ$ and $\varphi_2 \approx 26^\circ$). The π - π stacking distances in pDPPT2NAP and pDPPT3, based on the GIXD experiments, were 3.95 Å and 3.65 Å, respectively. Considering the DFT and GIXD data together, we postulate that the torsional angles in the pDPPT3 and pDPPT2TT polymers afforded closer π - π stacking among the polymer chains. The close polymer chain stacking is beneficial for carrier hopping and carrier mobility. Therefore, the pDPPT2TT-OD polymer showed the highest hole mobility of $1.93 \text{ cm}^2\text{V}^{-1}\text{s}^{-1}$.

In this feature article, we have presented systematic modulations of semiconducting polymer structures for organic FET applications. All the polymers have shown high carrier mobilities. More importantly, we demonstrate the design rule of polymer structure to improve polymer chain packing and carrier mobility. The importance of the side alkyl chains and polymer backbone planarity in low band gap polymers is particularly compelling. We believe our results for high performance polymer FETs provide significant insights for the development of new low band gap polymers showing high performance ambipolar FET properties.

References

- [1] Lee JS, Son SK et al. *Chem. Mater.* 2012; 24: 1316-1323.
- [2] Lee HS, Lee JS et al. *J. Phys. Chem. C* 2012; 116: 26204-26213.

[Feature Articles]

Development of Low-Temperature Solid Oxide Fuel Cells with Thin Bilayer Electrolytes Produced by Chemical Solution Deposition



Hae-Weon Lee
High Temp. Energy
Materials Research
Center
hwlee@kist.re.kr



Jong-Ho Lee
jongho@kist.re.kr



Ji-Won Son
jwson@kist.re.kr



Kyung Joong Yoon
kjyoon@kist.re.kr



Byung Kook Kim
bkkim@kist.re.kr

Introduction

In recent years, scientists have been looking for ways to lower the operating temperature of solid oxide fuel cells (SOFCs) in order to improve their reliability and cost effectiveness [1,2]. However, at lower operating temperatures, a conventional SOFC suffers from a substantial increase of ohmic resistance of all its components, particularly of the electrolyte. To address this issue, the majority of research investigations have focused on either employing high conductivity electrolytes, such as doped ceria and stabilized bismuth oxide, or reducing the thickness of yttria stabilized zirconia (YSZ), the most frequently used electrolyte material in conventional SOFCs.

To reduce electrolyte thickness, the chemical solution deposition (CSD) process has many advantages over vacuum deposition techniques, particularly cost effectiveness and scalability [3,4]. However, processing flaws, generated from constrained sintering, have prevented this technology from practical application to SOFCs [5]. Most processing flaws in CSD routes have a very strong tendency to develop in a preferred orientation, i.e., thickness direction, due to the bi-axial nature of the substrate constraint [6]. This results in morphological anisotropy and spatially gradient distributions of porosity and pore/grain sizes, which is considered the main reason for electrolyte leakage. Therefore, it is imperative that a CSD route minimize the constraining effects of the substrate on the densification and microstructural development of thin electrolyte. By far the majority of previous investigations

have managed to avoid electrolyte leakage by simply increasing film thickness, but this improvement has come at the expense of ohmic loss [7].

In this study, we report the development of extremely thin and stable electrolyte SOFCs fabricated by CSD in which the electrolyte and cathode are produced by means of a layer-by-layer construction on a rigid anode (NiO/YSZ) substrate. Even though the layer-by-layer construction of all component layers is subject to macroscale processing flaws arising from constrained sintering, it offers advantages over conventional co-firing methods because the technique allows better control over the microstructure of each layer; individual components can be processed separately under optimized conditions and engineered to maximize their performance. We have demonstrated that the incorporation of “slow-sintering” YSZ nanoparticles into the chemical solution allows formation of a dense and gas-tight YSZ electrolyte as thin as 100 nm on a rigid NiO-YSZ substrate by spin coating of the chemical solution and low-temperature sintering. The external constraining stresses arising from the substrate can be substantially reduced to a controllable level by decreasing the sintering rate of the precursor powder derived from the chemical solution with the help of the internal constraints of the slow-sintering YSZ nanoparticles. This same approach was extended to the fabrication of both a gadolinia-doped ceria (GDC) interdiffusion barrier layer and $\text{La}_{0.6}\text{Sr}_{0.4}\text{Co}_{0.2}\text{Fe}_{0.8}\text{O}_{3-\delta}$ (LSCF) cathode layer, except that the content of slow-sintering particles in the chemical solutions was adjusted below and above the rigidity threshold in order to control the final porosity.

General stability criteria for thin film electrolytes

In order to produce a thin YSZ layer in a YSZ/GDC bilayer electrolyte system on the anode side of GDC by CSD, it is necessary to consider at least three criteria for

the structural stability of the YSZ thin film on an anode substrate. First, the thickness of thin film YSZ needs to exceed the pore size present on the surface of the substrate in order to maintain its structural integrity throughout the fabrication process [8]. Secondly, the grain size of YSZ film should be kept smaller than its thickness in order to maintain its stability against film breakup [9]. Finally, the film thickness should be larger than the pore size of the reduced anode substrate for structural stability during operation [8]. By taking into account these film stability criteria, the final film thickness will be determined mainly by the substrate pore size and YSZ grain size. The substrate should have a fine-grained microstructure with residual porosity as small as possible in order to reduce the substrate pore size. Moreover, sintering at low temperatures should prevent excessive grain growth in order to minimize the film thickness. The stability criteria can be summarized as follows: the thin-film electrolyte needs to have a thickness greater than both the grain size of the film and the pore size of the substrate as long as major processing flaws are eliminated or at least reduced below a critical value.

Development of thin electrolyte SOFCs

Figure 1a shows a scanning electron microscopy (SEM) micrograph of a YSZ/GDC bilayer electrolyte deposited by CSD consisting of 100 nm thick YSZ and 400 nm thick GDC layers. The YSZ layer was spin coated using a chemical solution containing 5 vol% of commercially purchased YSZ nanoparticles with average particle size of 15 nm on a presintered NiO-YSZ anode substrate. Even though residual pores are present in a YSZ electrolyte in a porosity range of 5-10%, the macro-defects responsible for electrolyte leakage are mostly eliminated at the expense of the micro-defects, e.g., mainly isotropic pores of small sizes. It also should be emphasized that this thin YSZ electrolyte was produced at sintering temperatures

below 1100°C, leading to grain sizes smaller than 100 nm (Figure 1b). As a result, a thermodynamically stable YSZ film was achieved at a thickness of 100 nm. Likewise, a dense GDC layer was successfully deposited on top of the YSZ thin film layer by CSD processing without major flaws. The GDC layer completely covered the surface of the YSZ layer with a relatively uniform thickness, circa 400 nm, consequently forming a bilayer electrolyte with a total thickness of ~ 500 nm. Again, the local constraints generated by slow-sintering GDC nanoparticles with an average particle size of 10 nm effectively suppressed the substrate constraint and produced a relatively uniform microstructure without macro-defects, which are responsible for the formation of insulating second phase by chemical reaction between YSZ and LSCF layers.

Special attention should be paid to the interface between the YSZ and GDC layers in Figure 1a which shows very tight coverage and extremely good bonding. Considering the extremely high reactivity of the precursor

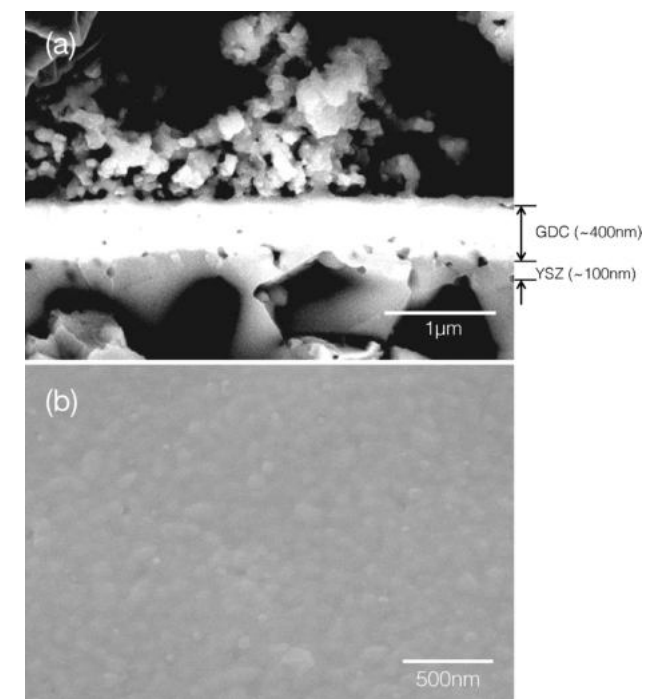


Figure 1. SEM image of: (a) YSZ (100 nm) / GDC (400 nm) bilayer electrolyte deposited on a rigid NiO-YSZ anode substrate; and (b) top view of the YSZ film (100 nm) showing the grain structure.

particles derived from the chemical solution and identical crystal structure of YSZ and GDC, the YSZ/GDC interface appears to be highly coherent [1]. Therefore, the YSZ/GDC bilayer collectively maintains its structural stability against the reduction of the load-supporting area by anode reduction in subsequent operation. In other words, if a cell with a 100 nm YSZ single layer is subjected to anode reduction, it cannot survive the reduction without local spallation followed by delamination cracking which results from the generation of pores in the substrate during the reduction process. The interface coherence found in the collective tailoring of the YSZ/GDC architecture in the bilayer electrolyte provides structural operating stability resulting from the total thickness of the combined layers, rather than the thickness of individual layers.

A thin GDC-LSCF interlayer (~40 nm) was spin coated prior to LSCF cathode deposition for the purpose of developing strong adhesion between the GDC and LSCF layers and reducing the interface pores (Figure 2a). In fact, this was facilitated by employing LSCF solution containing dispersed GDC nanoparticles, in which the LSCF precursor particles derived from the solution provide sufficient sintering driving force with strong adhesion to the LSCF cathode, and the GDC nanoparticles are active enough to form a great number of solid bridges between the interlayer and GDC layer [10]. At the same time, the relatively high density of this interlayer was deemed likely to bring about reduced area-specific resistance of the cell and cathode polarization loss. Finally, a 5 μm-thick LSCF cathode was deposited on top of the GDC-LSCF interlayer by spin coating followed by sintering at 950°C. Since the electrochemical performance of a LSCF cathode is strongly dependent on its microstructure, the grain and pore structures were optimized by utilizing a LSCF chemical solution containing LSCF particles (~150 nm) and fugitive pore former (hydroxypropyl cellulose (HPC)). LSCF particles in the solution in excess of the rigidity threshold resulted in a pore size of approximately 150 nm, and the surface was uniformly covered by extremely fine LSCF nanoparticles (< 50 nm)

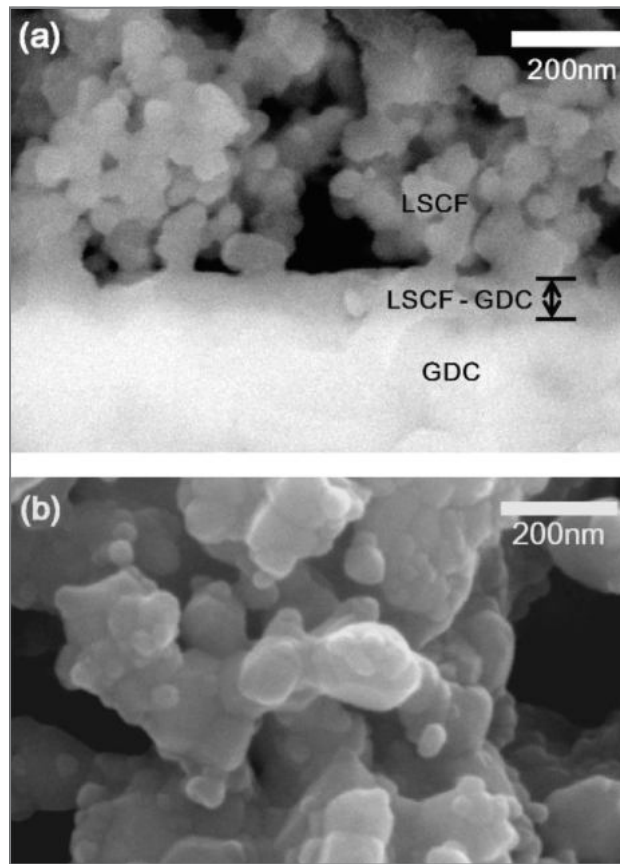


Figure 2. SEM images of: (a) LSCF-GDC interlayer; and (b) LSCF cathode.

synthesized from a salt solution, which would maximize the electrochemically active area and enhance the charge transfer reaction rate. Additional large pores (~2 μm) were introduced by the incorporation of HPC pore former to further improve mass transport through the electrode. As a result, a uniform LSCF cathode with an extremely high surface area and well-connected paths for gas diffusion was fabricated without sacrificing the structural stability of the bilayer electrolyte, as shown in Figure 2b.

Cell performance

A fabricated cell with an effective electrode area of 1 cm \times 1 cm was electrochemically characterized at 500–650°C using humidified H₂ (3% H₂O) as fuel and

air as oxidant. In Figure 3a, the open circuit voltage (OCV) was above 1 V over the entire temperature range, indicative of excellent gas-tightness of the thin electrolyte. This also supports our contention that the macro-defects rather than the porosity are the determining factors for electrolyte leakage. To the best of our knowledge, the OCV obtained in this study is the highest value reported so far for SOFCs with a thin electrolyte fabricated by the CSD process. The maximum power density was ~ 1.3 W cm⁻² and the power density at 0.8 V was 0.74 W cm⁻² at 650°C, which implies that cell performance could be significantly improved by decreasing electrolyte thickness and employing a nano-structured LSCF cathode. Specifically, the ohmic ASR at 650°C decreased from 0.12 $\Omega\cdot\text{cm}^2$ to 0.038 $\Omega\cdot\text{cm}^2$ as the total electrolyte thickness decreased from 7–8 μm common in conventional SOFCs to 500 nm in this study, and the polarization ASR was 0.226 $\Omega\cdot\text{cm}^2$ (Figure 3b), which is significantly lower than the values of conventional SOFCs measured at similar operating temperatures [11,12].

The postmortem analysis by SEM revealed that the extremely thin bilayer electrolyte maintained its structural integrity without any structural damages or failures. The YSZ layer consistently covered the GDC layer even in the presence of surface irregularities such as substrate warpage and surface roughness. As mentioned before, the interface coherence between the YSZ and GDC layers allowed us to elaborately manipulate the thickness of the bilayer electrolyte and to reduce the thickness of the individual layers to their thinnest limits. We cannot overemphasize that the reduction of electrolyte thickness and the elaboration of bilayer electrolyte are possible only when macro-defects are eliminated or reduced to insignificant sizes from the technical perspective of electrolyte leakage. In a cell with a 100 nm thick YSZ layer and 400 nm thick GDC layer, the GDC layer plays the role of a main electrolyte while the YSZ layer acts as a secondary electrolyte for blocking electron conduction of the GDC electrolyte. Whether the functional roles of component layers are as the main electrolyte or secondary

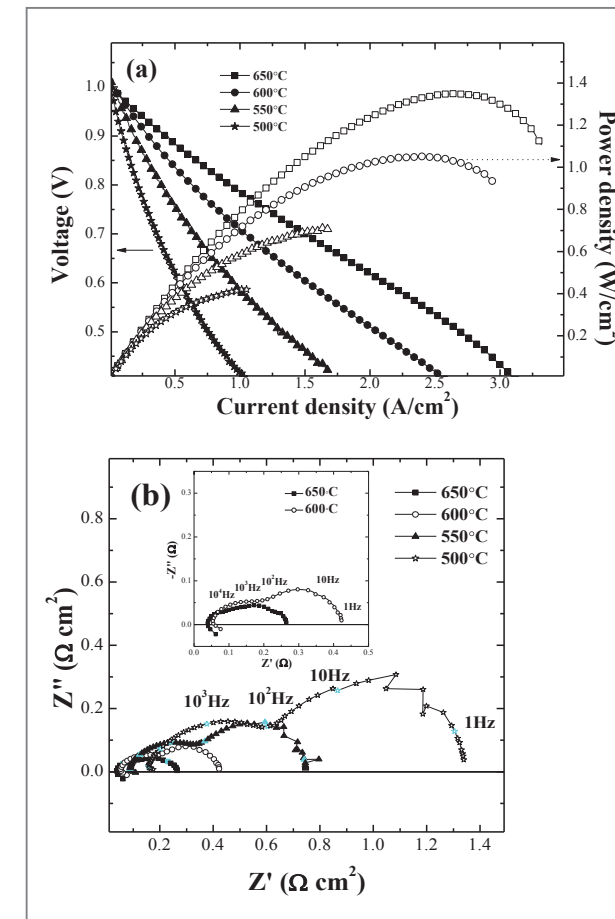


Figure 3. (a) Cell voltage and power density as a function of current density. (b) Impedance spectra at OCV measured at 500–650°C.

electrolyte, it is a prerequisite that they be capable of suppressing any gaseous transport through them. This is why macro-defects should be avoided in the component layers of a bilayer electrolyte in order to maintain structural stability during fabrication as well as operation.

Summary

The described CSD route is an enabling technique for thin electrolyte SOFCs only if macro-defects can be controlled and limited to an acceptable size. The macro-defects stemming from CSD techniques apparently originate from the constrained sintering of the electrolyte

in the presence of a rigid substrate, which promotes microstructural development in preferred orientations. Incorporation of slow-sintering nanoparticles into the chemical solution effectively suppresses the generation of macro-defects and directional development of film microstructure with the help of their local constraining effects. Judging from the results of this study, the thickness of the electrolyte could be further decreased by lowering the sintering temperature and reducing grain size. It should also be noted that in a YSZ-GDC system, structural stability against the substrate pores can be determined by the total thickness of the bilayer electrolyte rather than the YSZ layer alone. This allows the collective elaboration of the bilayer electrolyte to achieve maximum cell performance. To the best of our knowledge, the SOFC discussed in this study possesses the thinnest YSZ-GDC bilayer electrolyte yet developed, resulting in excellent electrochemical performance at low to intermediate operating temperatures.

Note

This article and images are cited from “Extremely Thin Electrolyte for Solid Oxide Fuel Cells (SOFCs) Fabricated by Chemical Solution Deposition (CSD)” in *Advanced Materials* 2012; 24: 3373- 3377.

References

- [1] Kwon CW, Son JW, Lee JH, Kim HM, Lee HW, Kim KB. *Adv. Funct. Mater.* 2011; 21: 1154.
- [2] Zou Y, Zhou W, Sunarso J, Liang FL, Shao ZP. *Int. J. Hydrogen Energy* 2011; 36: 9195.
- [3] Van Gestel T, Sebold D, Meulenberg WA, Buchkremer HP. *Solid State Ionics* 2008; 179: 428.
- [4] Hui R, Wang Z, Yick S, Maric R, Ghosh D. *J. Power Sources* 2007; 172: 840.
- [5] Xu X, Xia C, Huang S, Peng D. *Ceram. Int.* 2005; 31: 1061.

- [6] Kwon S, Messing GL. *J. Mater. Sci.* 1998; 33: 913.
- [7] Rose L, Kesler O, Tang ZL, Burgess A. *J. Power Sources* 2007; 167: 340.
- [8] De Jonghe L, Jacobson C, Visco S. *Annu. Rev. Mater. Res.* 2003; 33: 169.
- [9] Miller KT, Lange FF, Marshall DB. *J. Mater. Res.* 1990; 5: 151.
- [10] Soldati AL, Baqué L, Troiani H, Cotaro C, Schreiber A, Canero A, Serquis A. *Int. J. Hydrogen Energy* 2011; 36: 9180.
- [11] DiGiuseppe G, Sun L. *Int. J. Hydrogen Energy* 2011; 36: 5076.
- [12] Zhao F, Wang Z, Liu M, Zhang L, Xia C, Chen F. *J. Power Sources* 2008; 185: 13.

[Feature Articles]

Analysis of Rainwater Quality and Quantity for Effective Urban Water Management



Ju Young Lee

Natural Medicine Center
jyl7318@kist.re.kr

Introduction

As global population expands and becomes increasingly concentrated in urban areas, water resources are under constant threat. In particular, urbanization has contributed to increased surface runoff flooding and runoff contamination [1]. Current urban water management design is based primarily on downstream water control because this approach has been more economical than controlling runoff sources [2]. However, owing to climate change and expanding urbanization, downstream water management measures are increasingly ineffective. The occurrence of unpredictable rainfall events, for example, can cause severe imbalances in rainwater quantity through either flooding or drought, while expanding urbanization can cause an increase in nonpoint source pollution in downstream urban areas, which compromises the quality of rainwater. Hence, more attention is being focused on managing runoff in source areas rather than on increasing the flow efficiency and management of downstream water conveyance systems [2].

Increasingly, rainwater harvesting is becoming an integral part of the sustainable water management toolkit [3]. Effective rainwater harvesting strategies are essential to meet the escalating demand for sufficient good quality water in areas that experience urban stream depletion and water shortages [3]. Regarding rainwater quality, several studies have reported that rainwater harvesting may pose a public health risk because the collected

rainwater can potentially carry microbial pathogens [4,5]. Most guidelines for rainwater utilization suggest that bacterial pathogens such as total coliforms and *Escherichia coli* (*E.coli*) are not detectable at fewer than 1 CFU/100 mL [4]. The quality of harvested rainwater also depends on the type of roof where collection equipment is installed and environmental conditions, such as the unique local climate and atmospheric pollution [6]. Representative potential sources of nonpoint pollution on a rooftop are classified according to whether they are external or internal. External sources include airborne pollutants and organic substances from human activity, leaves and bird waste [1]. Internal sources of nonpoint pollution originate in the roofing materials themselves. Rainwater reacts physico-chemically with roofing materials, and the presence of lichens and mosses on the roof also influences water quality over the long term [1]. As regards effective water management, many studies have focused on conserving tap water through the installation of rainwater tanks [7], but only a few studies have focused on rainwater tank design to reduce runoff [2].

There are three different approaches that can generally be used for urban storm water modeling: the design storm event approach, the continuous simulation approach, and the derived probability distribution approach [8]. The design storm is a precipitation pattern based on historical precipitation data. However, this method has limitations which complicate drainage engineering because rainfall and runoff events involve many characteristics, including volume, intensity, and frequency. It is therefore impossible to include a full range of meteorological events when creating a response hydrograph, particularly when single events often overwhelm the interrelationships [8]. Hence, continuous simulation and analytical probabilistic modeling have been proposed as alternatives.

The main objective of this study was to examine the effect of roofing materials on the chemical and microbiological quality of rainwater harvested for domestic use. In addition, an analytical probabilistic model for use in designing a rainwater harvesting system was developed.

Quality assessment

To conduct our studies, conventional pilot scale roofs were constructed with wooden shingles, concrete tiles, Gi-Wa (clay tiles) and galvanized steel. The roofs were angled 20.5° from the horizontal with a catchment area of 2.55 m² (length = 1.5m, width = 1.7m). The channel, gutter and downpipe systems were manufactured from PVC. The gutters were shaped in a half round formation. Figure 1 shows a schematic diagram of the pilot scale roofs. Harvested rainwater samples were collected from the four pilot scale roofs made of different materials on 10 occasions in 2009, and 30 occasions in 2010. Table 1 summarizes the analytical parameters and methods.

Four types of roofing materials widely used in South Korea were analyzed to determine their suitability for application in rainwater harvesting for domestic use. Galvanized steel was found to be the most suitable roofing material after the first flush, with the resulting physical, chemical and biological water quality parameters meeting the Korean and WHO guidelines for drinking water quality. With regard to the physical and chemical parameters, the findings of this study show that the type of roofing material used has some influence on the quality of harvested rainwater. Regarding the microbiological aspect, the findings of this study suggest that galvanized steel and clay tiles are appropriate for rainwater harvesting

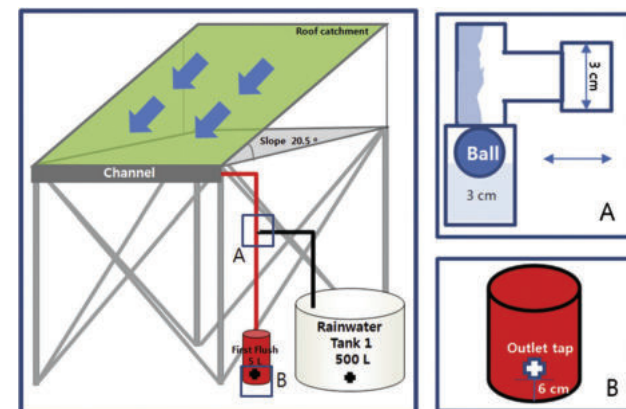


Figure 1. Schematic diagram of the pilot scale design.

Table 1. Review of analytical parameters and methods

	Parameter	Method and equipment
Physical	pH	Metrohm, Model 826 series
	TSS	APHA, 1995
Chemical	NO ₃ , SO ₄	DIONEX ICS 3000
	Metal	SHIMADZU AA-7000
Micro-biological	TOC	APHA, 2005
	TC, <i>E. coli</i>	GE-Sievers 5310 C, USA
	<i>Enterococci</i>	ISO method 9308-1
	<i>Pseudomonas spp.</i>	ISO 7899-2
	<i>Salmonella spp.</i> <i>Cryptosporidium spp.</i>	APHA, 1995

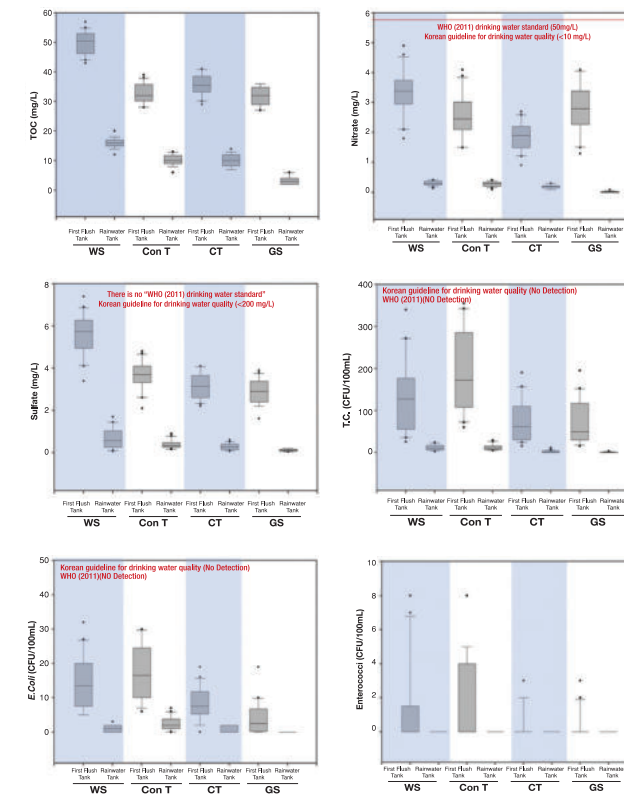


Figure 2. Box plot diagram for rainwater quality in the different roofing material samples (total events [n=40]). Note: WS=Wooden Shingle; Con T= Concrete tile; CT=Clay Tile (*Gi-Wa*); GS=Galvanized Steel

applications. No bacterial pathogens (*Pseudomonas spp.*, *Salmonella spp.* and *Cryptosporidium spp.*) were detected in the water samples taken from the first flush tank of the galvanized steel roof, possibly because ultraviolet light and high temperatures acted as disinfection agents.

Quantity assessment

The quantity assessment of a rainwater harvesting system is demonstrated by the water balance equations following Figure 3. After rainfall (*r*) occurs in the catchment (A), some of the water is lost by evaporation (E), some is retained on the catchment (S_c), and the remaining water leaves the catchment as runoff (Q_{out,c}) (Figure 3). Using the relationship between rainfall and runoff in the catchment, a mass balance equation for calculating the runoff from the catchment can be established using Equation 1.

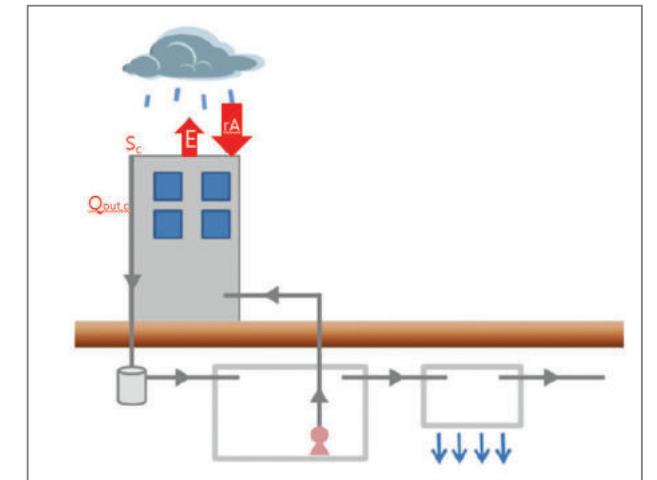


Figure 3. The schematic diagram of a rainwater harvesting system.

$$Q_{out,c} = \begin{cases} 0 & r \leq \frac{EA + S_c}{A} \\ rA - EA - S_c r & r > \frac{EA + S_c}{A} \end{cases} \quad (1)$$

In a rainwater storage tank, inflow (Q_{in,t}) into the storage tank is usually the same as the rainfall-runoff (Q_{out,c}) from the catchment. Some of the inflow is supplied to the building for toilet flushing and gardening (Q_s), and the rest is stored in the tank (S_{t,t}). When heavy rains occur, taking the inflow (Q_{in,t}) and outflow (Q_s, Q_{out,t}) into consideration, the mass balance equation for the storage tank can be calculated using Equation 2:

$$Q_{out,t} = \begin{cases} 0 & V_t \geq Q_{in,t} + S_{tb} - Q_s \\ Q_{in,t} + S_{tb} - Q_s - V_t & V_t < Q_{in,t} + S_{tb} - Q_s \end{cases} \quad (2)$$

Where V_t is the volume of the tank, S_{tb} is stored rainwater in the tank before a rainfall event. Stored water in the tank can be calculated by Equation 3. S_{ta} , stored rainfall in the tank after a rainfall event, is calculated by Equation 3 (Figure 4a).

$$S_{ta} = \begin{cases} 0 & 0 \geq Q_{in,t} + S_{tb} - Q_s \\ Q_{in,t} + S_{tb} - Q_s & 0 < Q_{in,t} + S_{tb} - Q_s \leq V_t \\ V_t & V_t < Q_{in,t} + S_{tb} - Q_s \end{cases} \quad (3)$$

Infiltration inflow ($Q_{in,i}$) comes from the catchment ($Q_{out,c}$) or as overflow from the storage tanks ($Q_{out,t}$) (Figure 4b). The amount of overflow from the infiltration facility can be calculated using Equation 4. $Q_{in,i}$ is inflow to the infiltration facility, and V_i is the volume of the infiltration facility.

$$Q_{out,i} = \begin{cases} 0 & V_i \geq Q_{in,i} + S_{tb} - Q_i \\ Q_{in,i} + S_{tb} - Q_i - V_i & V_i < Q_{in,i} + S_{tb} - Q_i \end{cases} \quad (4)$$

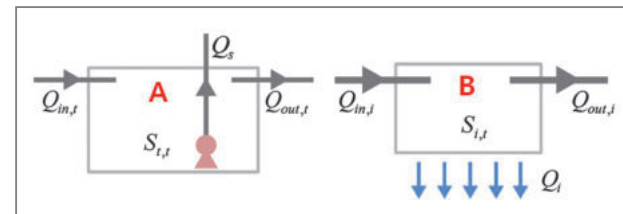


Figure 4. (A) Water flow in the storage tank. (B) Water flow in the infiltration system.

Analytical probabilistic modeling of rainfall for designing rainwater harvesting systems

There is no runoff from the catchment when the sum of evaporation and retention storage is larger than the total quantity of rainfall. The probability of no runoff occurring can be calculated using the steps illustrated in Figure 5. When rainfall exceeds the sum of evaporation

and retention storage, the runoff can be expressed by step 1. The probability density function of the runoff can then be calculated by differentiating step 2. Therefore, the quantity of runoff according to the range of rainfall on the catchment can be expressed by step 3. On the basis of step 3, the average runoff from the catchment can be expressed by step 4.

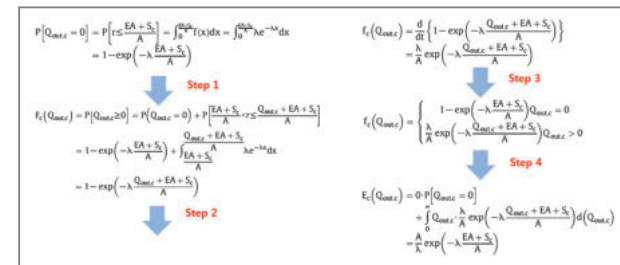


Figure 5. Calculating steps for rainfall-runoff on the catchment.

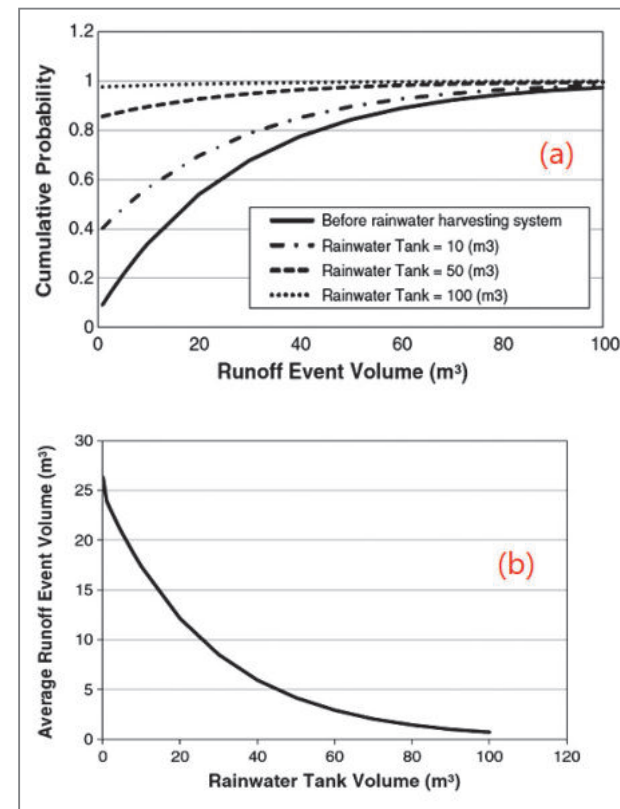


Figure 6. (a) The effect of storage tank volume on rainfall-runoff reductions in a rainwater harvesting system. (b) Average runoff depending on storage tank volume of a rainwater harvesting system.

We applied these derived equations to analyze rainfall-runoff at office building # 39 on the Seoul National University campus. Based on results from this analysis, Figure 6a displays the effect of a rainwater harvesting system on rainfall-runoff reductions for a specified return period. For example, when the return period is five years, a 10-ton rainwater tank will decrease the runoff event volume from 42 to 32 tons. This methodology provides a powerful tool for designing the storage capacity for a given catchment. The average response of runoff volume to tank capacity is shown in Figure 6b.

Conclusions

Unlike most prior studies which have focused on managing graywater, this study examined the quality and quantity of captured rainwater as part of an effort to identify alternative, sustainable water resources. Most notably, this study addressed the effect of specific harvesting systems on the reduction in rainfall-runoff and the variation of rainwater quality as determined by biological, chemical and physical parameters. Our findings demonstrate that different roofing materials have a direct impact on rainwater quality and we employed the use of a rainfall-runoff reduction model based on an analytical probabilistic analysis. Through our analysis of rainwater quality and quantity, we determined that harvested rainwater has considerable potential to help alleviate water shortages. The proposed model provides a powerful and easily applied tool for designing rainwater harvesting systems that can increase the utilization of runoff water onsite and can mitigate some of the problems associated with downstream flooding.

Note

This article and its images are cited from “The application of an analytical probabilistic model for

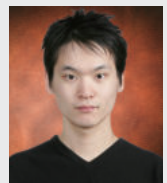
estimating the rainfall-runoff reductions achieved using rainwater harvesting system” in *Science of the Total Environment*, Vol. 424, pp. 213-218 and “Quality of roof-harvested rainwater-Comparison of different roofing materials” in *Environmental Pollution*, Vol.162, pp. 422-429.



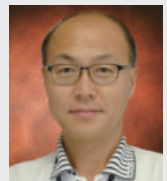
References

- [1] Lee JY, Han MY et al. *Environ. Pollu.* 2012; 162: 422-429.
- [2] Han MY, Lee JY et al. *Sci. Tot. Environ.* 2012; 424: 213-218.
- [3] Ward S, Memon A et al. *Wat. Sci. Technol.* 2010; 61(1): 85-96.
- [4] Ahmed W, Gardner T et al. *Environ. Qual.* 2011; 40: 1-9.
- [5] Simmons G, Hope V et al. *Wat. Res.* 2011; 35(6): 1518-1524.
- [6] Lye DJ. *Sci. Tot. Environ.* 2009; 407: 5429-5434.
- [7] Su MD, Lin CH et al. *Resour. Conserv. Recycl.* 2009; 53(7): 393-399.
- [8] Chen JY, Adams DR et al. *Appl. Hydrol.* New York: McGraw-Hill; 1988.

Effect of Steric Factors Affecting the Preferential Diffusion of Cu(II) in Mesoporous Structures



Jaeshik Chung
Center for Water
Resource Cycle
Research
jschung@kist.re.kr



Sang Hyup Lee
yisanghyup@
kist.re.kr



Seok Won Hong
swhong@
kist.re.kr

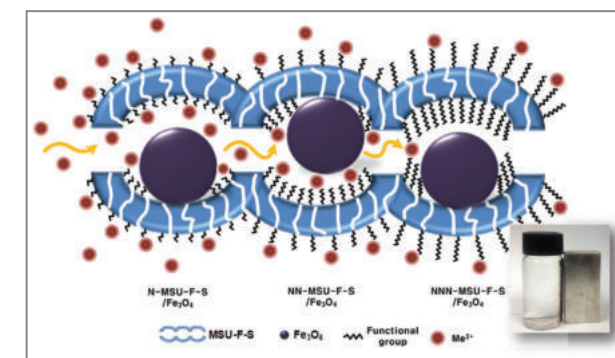
Introduction

Since copper is the most commonly used metal in industrial applications, including the electrical, electro-plating, metal finishing and paint industries, residual metal is often found in wastewater [1, 2]. Dissolved heavy metals are neither biologically degradable nor separable via membrane processes, and thus pose a threat to human health and entire ecosystems.

The development of porous materials with large surface areas is currently an area of extensive research, particularly with regard to potential applications in areas such as sorption, chromatography, catalysis, sensor technology, and gas storage [3]. Zeolite is a natural molecular sieve that has a pore size of 15 Å. MCM-41 and SBA-15, on the other hand, are chemically synthesized organic-inorganic hybrid materials with larger (2-10 nm) pores, allowing the potential introduction of various molecules. Although silica itself hardly reacts with other materials, the incorporation of an organic/inorganic functional group can turn it into an excellent sorbent. The thermal stability and high density of silanol groups (from 0.5 to 3.0 OH per nm²) [4] help to fix large amounts of silanes with sorption activity on to a silica surface [5]. Suzana et al. [6] used silica aerogels modified with a mercapto-(thiol-) functional group to remove Cu(II) and Hg(II) from wastewater. Unlike a thiol-functional group, there are several types of amino-silanes, classified by the number of amines in an organic chain. The surface density of functionalized groups and the mesoporous framework structure have been changed in order to clarify the

effect of the density of amino groups on molecular and nano scales, as well as the nature of the porous structure. Hideaki et al. [5] investigated sorption properties of chromate and arsenate onto amino-functionalized MCM-41 and SBA-1, finding that blockages by functional groups near the pore mouth sometimes caused mass transport hindrance.

Like any new technology, nanomaterials carry a potential for harm as well as good. Some of these novel materials may turn out to be hazardous to our health or the environment. The size of nanoparticles means that they can more readily escape into the environment and infiltrate deep into internal organs such as the lungs and liver [7]. Likewise, recovery of sorbent is important in water treatment applications. Gravity settling in the traditional water treatment process is usually the rate-limiting step which brings load to the entire process. In this study we synthesized mesoporous silica, MSU-F-S, and loaded nano-scale magnetite (Fe₃O₄) for easy recovery. Subsequently, mono-, di- and tri-amino functional groups were introduced to investigate the sorption properties of Cu(II) into macro- and micropores of mesoporous material (Scheme 1) and their reactivity was compared with various kinetic models.



Scheme 1. A schematic concept of preferential diffusion of metal ion into pores of functionalized porous material and magnetically separated MSU-F-S/Fe₃O₄ under an external magnetic field after 10 min of contact time. An excessive amount of functional molecules such as magnetite and/or ligand chains in the pore structure could exert unfavorable effects via steric hindrance.

Preparation of samples

MSU-F-S, the supporting material for the functional group, was prepared by the reported procedure [8]. Magnetite impregnation was carried out using 7 g of Fe(NO₃)₃·9H₂O as a precursor in 40 ml Ethanol, and functionalization was achieved using different amino (mono-, di-, tri-) silanes. Each synthesized sample was characterized using TEM and CHN analysis.

Cu(II) sorption kinetics procedure

0.01 g of dried amino-functionalized MSU-F-S and MSU-F-S/Fe₃O₄ was added into a 15 mL vial containing 10 mg/L CuCl₂ and shaken for a certain interval with a 10 rpm-rotary shaker. Samples were then taken, and the supernatant was filtered through a 0.45 μm membrane filter and analyzed using ICP-OES (Varian, Vista PRO). The amount of copper uptake was determined by the difference in concentration between the initial and final solutions. All experiments were performed in triplicate.

Characterization of synthesized materials

Synthesized MSU-F-S had about 30 nm of uniform pores in the TEM image (Figure 1). These pores are slightly larger than those of the other mesoporous silica

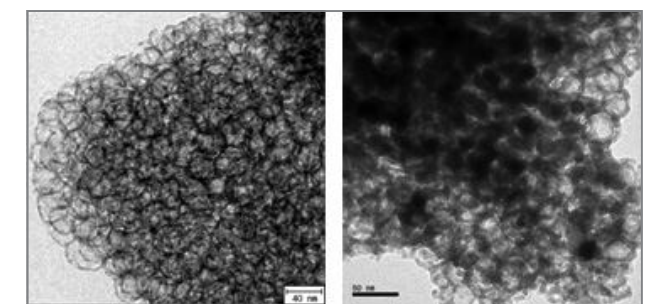


Figure 1. TEM image of synthesized MSU-F-S (left) and MSU-F-S/Fe₃O₄ (right).

Table 1. Surface characteristics of mono- (N-), di- (NN-), tri-amine- (NNN-) grafted MSU-F-S/(Fe₃O₄)

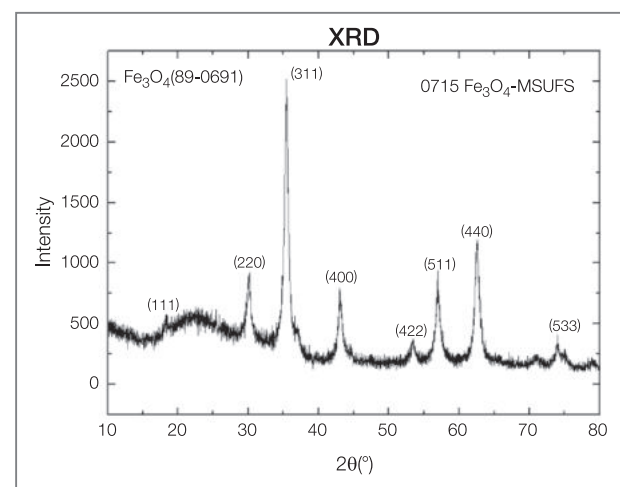
	MSU-F-S (/Fe ₃ O ₄)	N-MSU-F-S (/Fe ₃ O ₄)	NN-MSU-F-S (/Fe ₃ O ₄)	NNN-MSU-F-S (/Fe ₃ O ₄)
Surface Area (m ² /g)	363.4 (242.4*)	312.1 (165.1*)	251.3 (129.1*)	210.1 (89.6*)
Pore Volume (cm ³ /g)	1.72 (1.05*)	1.55 (0.81*)	1.35 (0.77*)	1.16 (0.51*)
N Contents (mmol/g)	-	1.53 (1.16*)	2.80 (1.99*)	3.58 (4.06*)
pH _{PZC}	1.0 (1.0*)	4.8 (4.8*)	5.0 (5.0*)	10.0 (10.0*)

* with nano-scale magnetite(Fe₃O₄) loaded

(MCM-41, SBA-15), thereby offering a more conducive surface for the application of nano-scale magnetite. Important surface characteristics, including surface area, pore volume, N contents, and zeta potentials of the materials, are listed in Table 1.

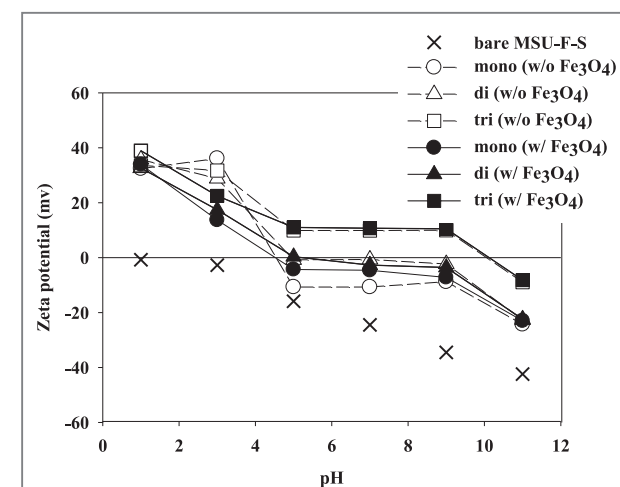
The bare MSU-F-S exhibited pores averaging 30 nm in diameter in the TEM image (Figure 1). Pore volume and surface area shrank gradually after Fe₃O₄ impregnation and grafting of the amino functional groups whereas N contents were gradually increased as more amino groups were applied.

Embedded nano magnetite was characterized by XRD analysis (Figure 2). The original peak of the crystalline

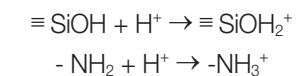
**Figure 2.** XRD pattern of synthesized MSU-F-S/(Fe₃O₄).

structure of Fe₃O₄, calculated using the Debye-Scherrer equation, was 13.7 ± 0.5 nm. After the experiment, residual particles in the vial were recovered from suspension by magnetic separation. By using a strong neodymium magnet, suspended solids were attracted immediately and most of the particles were recovered within 10 minutes.

Figure 3 shows the initial pH_i vs. surface charge obtained by the batch equilibration technique for a solid to solution ratio of 1 g/L. It has been found that MSU-F-S acts as a buffer in a wide range of pH from ca. 5 to 9. For all values of pH_i in this range, the pH_e increased by almost 9 (not shown here) due to the protonation of silanol and

**Figure 3.** Surface charge of synthesized MSU-F-S/(Fe₃O₄).

amino groups on the surface, as follows:



Surface charge analysis also displayed similar trends to those above; as more amine-groups were applied to the MSU-F-S/ Fe₃O₄, the surface tended to have (+) charges at certain pH values and the pH_{PZC} also increased. At pH values lower than the pH_{PZC}, surface silanol groups protonated, producing OH⁺ on the surface, which interrupted the approach of cationic metal ions. Amino groups also protonated into NH₃⁺, no longer valid for heavy metal complexation. On the other hand, with pH values higher than the pH_{PZC}, surface amino groups became negative due to the OH⁻ on surface silanol groups, and this may have caused cationic heavy metals to be attracted while the unshared electron pair of the amino group remained vacant for heavy metal complexation. Loading of nano-magnetite was found to have little effect on the surface charge.

Cu(II) sorption kinetics and steric factors

Kinetic analysis of certain reactions often provides useful information about reaction mechanisms. The equation can be generalized as follows:

$$d[A]/dt = -k[A]^a[B]^b$$

[A] = activity (concentration) of chemical species A

a = reaction order of chemical species A

k = reaction rate constant

If species A is the only reactive substrate, the 1st order reaction equation will be

$$d[A]/dt = -k_1[A]$$

k₁ = 1st order rate constant (min⁻¹)

The pseudo-2nd order model, which is based on sorption capacity of an sorbent, assumes that the sorption rate is proportional to the square of the difference

between sorption capacity and the sorbed amount at any time, t

$$dq_t/dt = k_2(q_e - q_t)^2$$

$$t/q_t = 1/(q_e k_2) + t/q_e$$

k₂ = pseudo-2nd order rate constant (g/mg.min)

q_e = maximum sorbed amount at equilibrium (mg/L)

q_t = sorbed amount at any time t (mg/g)

Figures 4 and 5 show the kinetic sorption experiment results of Cu(II) and how they fit to the model. Most of the Cu(II) was removed within the first 30 minutes in mono- and diamine-functionalized samples, whereas most triamine-functionalized samples took more than 240 minutes to reach equilibrium. The MSU-F-S embedded with magnetite demonstrated decreased sorption rates compared to that without magnetite, Embedded magnetite also had a negative effect on Cu(II) sorption rates compared to that with no magnetite inside, perhaps as a result of the modified surface.

The 1st order reaction model and pseudo-2nd reaction model were applied to find the rate constant [9] (Table 2). Although the R² value in the 1st order reaction model was low, the order of rate constant was mono- > di- ≈ tri-amine. Similar trends were found in the pseudo-2nd reaction model, yielding an approximate reactivity

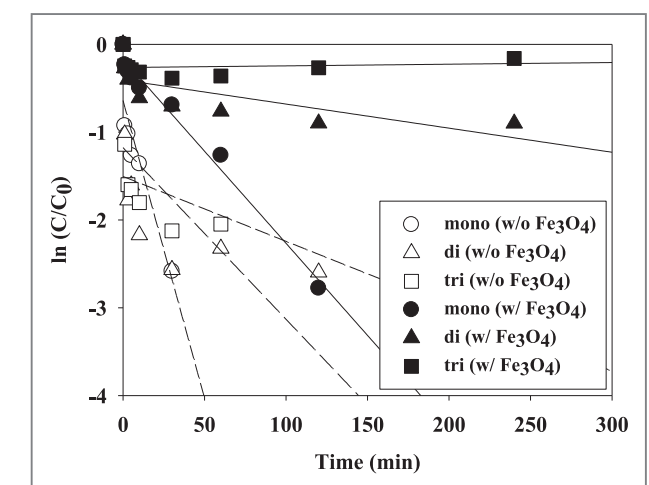
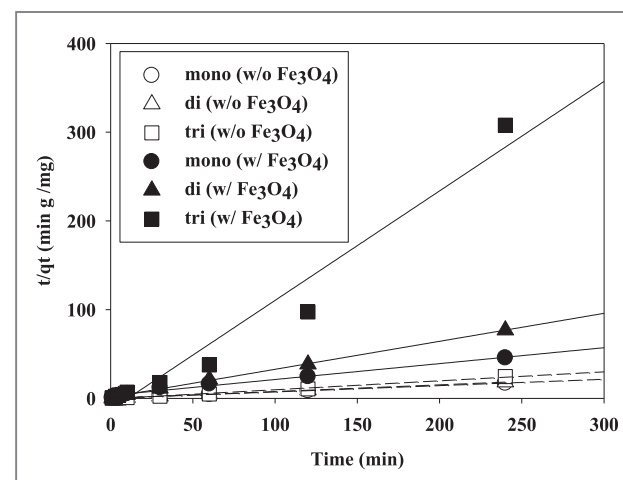
**Figure 4.** 1st order model fitted kinetic sorption experiment (C₀ = 10 mg/L).

Table 2. Estimated kinetic parameters of Cu(II) sorption experiment

	1st order reaction model		Pseudo-2nd order reaction model	
	k_1 (min ⁻¹)	R ²	k_2 (g/mg·min)	R ²
N-MSU-F-S (/Fe ₃ O ₄)	-6.8×10 ⁻² (-2.1×10 ⁻² *)	0.83 (0.98*)	3.8×10 ⁻² (9.6×10 ⁻³ *)	0.99 (0.98)
NN-MSU-F-S (/Fe ₃ O ₄)	-7.4×10 ⁻³ (-2.7×10 ⁻³ *)	0.42 (0.53*)	6.7×10 ⁻² (8.3×10 ⁻² *)	0.99 (0.99*)
NNN-MSU-F-S (/Fe ₃ O ₄)	-1.9×10 ⁻² (2.0×10 ⁻⁴ *)	0.35 (0.02*)	-2.7×10 ⁻² (-1.2×10 ⁻¹ *)	0.99 (0.96*)

* with nano-scale magnetite(Fe₃O₄) loaded

order of mono->di->tri-amine, which is more suitable for the data analysis (Table 2).

**Figure 5.** Pseudo-2nd order model fitted kinetic sorption experiment ($C_0 = 10$ mg/L).

Although tri-amine functionalized samples did not fit well to the model, the Cu(II) sorption rate onto amine functionalized MSU-F-S was highly dependent on the embedded magnetite and also on the number of amine groups in a ligand chain.

Because the pore size of MSU-F-S is not very big (30 nm), magnetite particles (about 15 nm) and entangled amine groups could block the entrance and hinder the intra-pore diffusion of metal ions in tri-amine-grafted MSU-F-S. Positively charged amino groups might push each other and expand, blocking the passage of metal ions into

the nanopores of MSU-F-S. As the chains of the attached functional group become longer and larger, it will be more likely that they become entangled and conceal the pores.

Conclusion

As stated above, various functionalities such as amine groups for Cu(II) sorption and nano-scale magnetite for easy separation were successively introduced to the mesoporous silica, and their reactivity was evaluated in terms of steric factors. The results were in agreement with pseudo-2nd order reaction kinetics more than 1st order, and embedded magnetite and amine groups played a significant role in sorption kinetics. Excessively introduced functional groups on certain pore structures seemed to cause failure of the system by the steric congestion effect. Thus, it should be noted that the pore size of the sorbent and characteristics of the functional group used are significant factors in the enhancement of sorption capacity.

Note

This article and images are cited from: Chung J, Chun J, Lee SH, Lee YJ, Hong SW. *J. Haz. Mat.* 2012; 239-240: 183-191.

References

- [1] Da'na E, Sayari A. *Chem. Eng. J.* 2011; 166: 445-453.
- [2] Da'na E, Sayari A. *Chem. Eng. J.* 2011; 166: 454-459.
- [3] Hoffman F, Cornelius M et al. *Angew. chemie.* 2006; 45: 3216-3251.
- [4] Zhao XS, Lu GQ et al. *Phys. Chem. B* 1997; 101:6525-6531.
- [5] Yoshitake H, Yokoi T et al. *Chem. Mater.* 2002; 14: 4603-4610.
- [6] Štandeker S, Veronovski A et al. *Desalination* 2011; 269: 223-230.
- [7] "Nano-Risks: A Big Need for a Little Testing" *Scientific American Magazine*, (<http://www.scientificamerican.com/article.cfm?id=big-need-for-a-little-testing>), January, 2010.
- [8] Kim S, Pauly TR, Pinnavaia TJ. *Chem. Commun.* 2000; 17: 1661-1662.
- [9] Ho YS, Mckay G. *Process Biochem.* 1999; 34: 451-465.

Amygdalar stimulation produces alterations on firing properties of hippocampal place cells

The Journal of Neuroscience
2012.8.15. 32(33):11424–11434.

Eun Joo Kim, Earnest S. Kim, Mijeong Park, Jeiwon Cho, Jeansok J. Kim
jeiwon@kist.re.kr

Stress is a biologically ubiquitous factor that, when perceived uncontrollable by humans and animals, can have lingering adverse effects on brain and cognitive functions. We have previously reported that rats that experienced inescapable-unpredictable stress subsequently exhibited decreased stability of firing rates of place cells in the CA1 hippocampus, accompanied by impairments in CA1 long-term synaptic potentiation and spatial memory consolidation. Because the elevated level of glucocorticoid hormones and the heightened amygdalar activity have been implicated in the emergence of stress effects on the hippocampus, we investigated whether administration of corticosterone and electrical stimulation

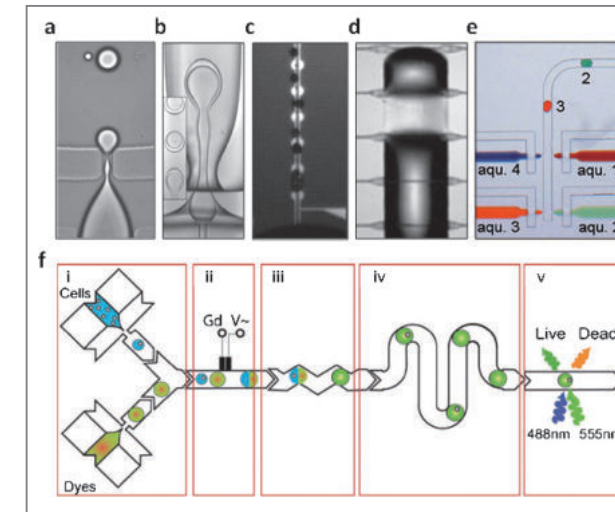
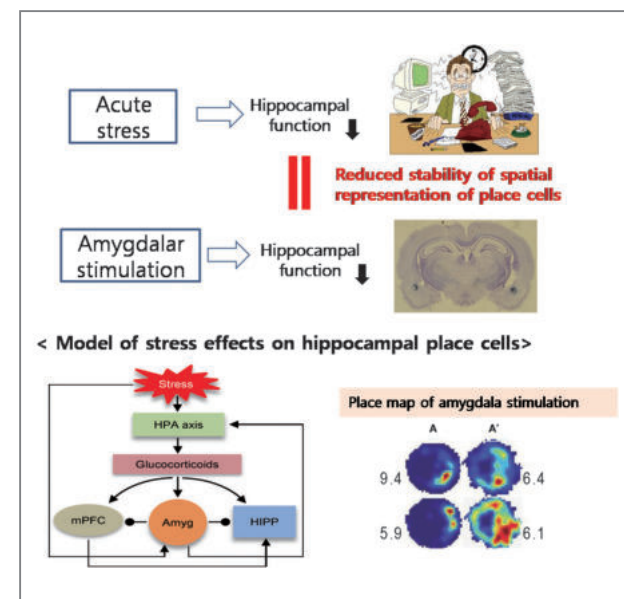
of the amygdala can produce stress-like alterations on hippocampal place cells. To do so, male Long–Evans rats chronically implanted with tetrodes in the hippocampus and stimulating electrodes in the amygdala were placed on a novel arena to forage for randomly dispersed food pellets while CA1 place cells were monitored across two recording sessions. Between sessions, animals received either corticosterone injection or amygdalar stimulation. We found that amygdalar stimulation reliably evoked distress behaviors and subsequently reduced the pixel-by-pixel correlation of place maps across sessions, while corticosterone administration did not. Also, the firing rates of place cells between preamygdalar and postamygdalar stimulation recording sessions were pronouncedly different, whereas those between precorticosterone and postcorticosterone injection recording sessions were not. These results suggest that the heightened amygdalar activity, but not the elevated level of corticosterone per se, reduces the stability of spatial representation in the hippocampus by altering the firing rates of place cells in a manner similar to behavioral stress.

Revisiting labonachip technology for drug discovery

Nature Reviews | Drug Discovery
2012; 8: 620–632.

Pavel Neuzil, Stefan Giselbrecht, Kerstin Lange, Tony Jun Huang, Andreas Manz
manz@kist-europe.de

The field of microfluidics or labonachip technology aims to improve and extend the possibilities of bioassays, cell biology and biomedical research based on the idea of miniaturization. Microfluidic systems allow more accurate modelling of physiological situations for both fundamental research and drug development, and enable systematic high-volume testing for various aspects of drug discovery.



Microfluidic systems are in development that not only model biological environments but also physically mimic biological tissues and organs; such “organs on a chip” could have an important role in expediting early stages of drug discovery and help reduce reliance on animal testing. This review highlights the latest labonachip technologies for drug discovery and discusses the potential for future developments in this field.

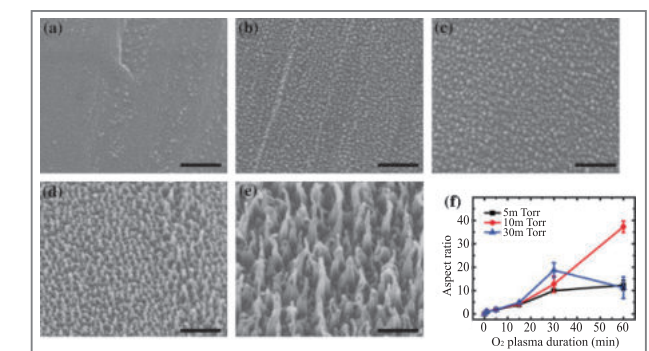
Water condensation behavior on the surface of a network of superhydrophobic carbon fibers with high-aspect-ratio nanostructures

Carbon
2012; 50: 5085–5092.

Tae-Jun Ko, Eun Kyu Her, Bongsu Shin, Ho-Young Kim, Kwang-Ryeol Lee, Bo Ki Hong, Sae Hoon Kim, Kyu Hwan Oh, Myoung-Woon Moon
mwmooon@kist.re.kr

We explored the condensation behavior of water on a superhydrophobic carbon fiber (CF) network with high-

aspect-ratio hair-like nanostructures. Nanostructures ranging from nanopillars to hairy shapes were grown on CFs by preferential oxygen plasma etching. Superhydrophobic CF surfaces were achieved by application of a hydrophobic siloxane-based hydrocarbon coating, which increased the water contact angle from 147 to 163 and decreased the contact angle hysteresis from 71 to below 5, sufficient to cause droplet roll-off from the surface. Water droplet nucleation and growth on the superhydrophobic CF were significantly retarded due to the high-aspect-ratio nanostructures under supersaturated vapor conditions. CFs became wet with condensation between fibers of the pristine surface under super-saturated vapor conditions, which eventually led to flooding. However, dropwise condensation became dominant in the superhydrophobic CF network, allowing for easy removal of the condensed droplets, which largely allowed the interstitial spaces of the fiber network to remain dry. It is implied that superhydrophobic CF can provide a passage for vapor or gas flow in wet environments such as a gas diffusion layer requiring effective water removal in the operation of a proton exchange membrane fuel cell.



ESEM images on three different fiber surfaces: (a) pristine; (b) 15 min plasma-treated and 30 s hydrophobic film-coated; and (c) 60 min plasma-treated and 30 s hydrophobic film-coated surfaces (Scale bars are 50 μm). (d–f) Schematics regarding the condensation of water with respect to the aspect ratio of nanostructures formed on the CFs.

Emerging memories: resistive switching mechanisms and current status

Reports on Progress in Physics

2012; 75(7): 076502-1-31.

Doo Seok Jeong, Reji Thomas, R S Katiyar, J F Scott, H Kohlstedt, A Petraru, Cheol Seong Hwang
dsjeong@kist.re.kr

The resistance switching behaviour of several materials has recently attracted considerable attention for its application in non-volatile memory (NVM) devices, popularly described as resistive random access memories (RRAMs). RRAM is a type of NVM that uses a material(s) that changes the resistance when a voltage is applied. Resistive switching phenomena have been observed in many oxides: (i) binary transition metal oxides (TMOs), e.g., TiO_2 , Cr_2O_3 , FeOx and NiO ; (ii) perovskite-type complex TMOs that are variously functional, paraelectric, ferroelectric, multiferroic and magnetic, e.g., $(\text{Ba,Sr})\text{TiO}_3$, $\text{Pb}(\text{ZrxTi}1-x)\text{O}_3$, BiFeO_3 and $\text{PrxCa}1-x\text{MnO}_3$; (iii)

large band gap high-k dielectrics, e.g., Al_2O_3 and Gd_2O_3 ; and (iv) graphene oxides. In the non-oxide category, higher chalcogenides are front runners, e.g., In_2Se_3 and In_2Te_3 . Hence, the number of materials showing this technologically interesting behaviour for information storage is enormous. Resistive switching in these materials can form the basis for the next generation of NVM, i.e., RRAM, when current semiconductor memory technology reaches its limit in terms of density. RRAMs may be the high-density and low-cost NVMs of the future. A review of this topic is valuable for focusing on the most promising materials to accelerate application into the semiconductor industry. This review is a small effort to realize the ambitious goal of RRAMs. Its basic focus is on resistive switching in various materials with particular emphasis on binary TMOs. It also addresses the current understanding of resistive switching behaviour. Moreover, a brief comparison between RRAMs and memristors is included. The review ends with the current status of RRAMs in terms of stability, scalability and switching speed, which are three important aspects of integration onto semiconductors.

Selective oxidative degradation of organic pollutants by singlet oxygen-mediated photosensitization: tin porphyrin versus c60 aminofullerene systems

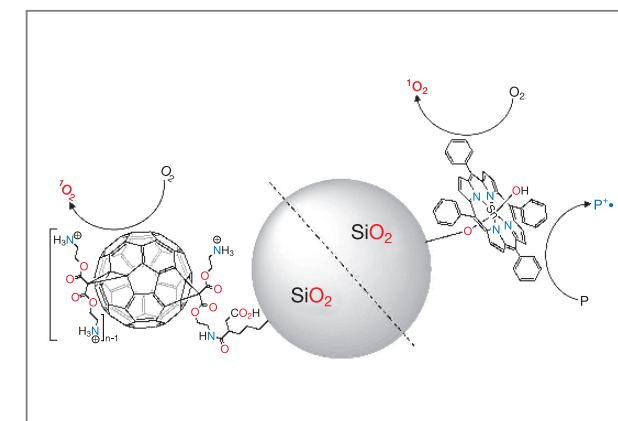
Environmental Science & Technology

2012; 46(17): 9606-9613.

Heechan Kim, Wooyul Kim, Yuri Mackeyev, Gi-Seon Lee, Hee-Joon Kim, Takashi Tachikawa, Seokwon Hong, Sanghyup Lee, Jungbae Kim, Lon J. Wilson, Tetsuro Majima, Pedro J. J. Alvarez, Wonyong Choi, Jaesang Lee
lee39@kist.re.kr

This study evaluates the potential application of tin

porphyrin- and C_{60} aminofullerene-derivatized silica (SnP/silica and $\text{aminoC}_{60}/\text{silica}$) as $^1\text{O}_2$ generating systems for photochemical degradation of organic pollutants. Photosensitized $^1\text{O}_2$ production with SnP/silica , which was faster than with $\text{aminoC}_{60}/\text{silica}$, effectively oxidized a variety of pharmaceuticals. Significant degradation of pharmaceuticals in the presence of the 400-nm UV cutoff filter corroborated visible light activation of both photosensitizers. Whereas the efficacy of $\text{aminoC}_{60}/\text{silica}$ for $^1\text{O}_2$ production drastically decreased under irradiation with $\lambda > 550$ nm, Q-band absorption caused negligible loss of the photosensitizing activity of SnP/silica in the long wavelength region. Faster destruction of phenolates by SnP/silica and $\text{aminoC}_{60}/\text{silica}$ under alkaline pH conditions further implicated $^1\text{O}_2$ involvement in the oxidative degradation. Direct charge transfer mediated by SnP , which was inferred from nanosecond laser flash photolysis, induced significant degradation of neutral phenols under high power light irradiation. Self-sensitized destruction caused gradual activity loss of SnP/silica in reuse tests unlike $\text{aminoC}_{60}/\text{silica}$. The kinetic comparison of SnP/silica and TiO_2 photocatalyst in real wastewater effluents showed that photosensitized singlet oxygenation of pharmaceuticals was still efficiently achieved in the presence of background organic matters, while significant interference was observed for photocatalyzed oxidation involving non-selective OH radical.



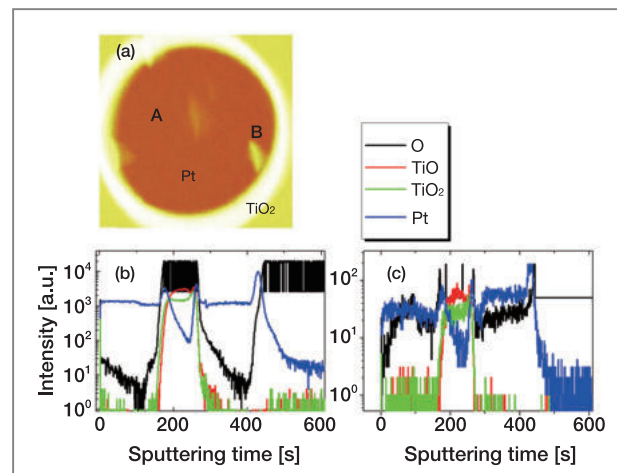
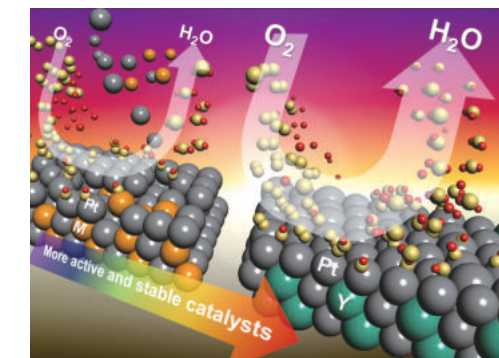
Role of electronic perturbation in stability and activity of Pt-based alloy nanocatalysts for oxygen reduction

Journal of the American Chemical Society

134(48): 19508-19511.

Seung Jun Hwang, Soo-Kil Kim, June-Gunn Lee, Seung-Cheol Lee, Jong Hyun Jang,† Pil Kim, Tae-Hoon Lim, Yung-Eun Sung, Sung Jong Yoo
sjhwang@kist.re.kr

The design of electrocatalysts for polymer electrolyte membrane fuel cells must satisfy two equally important fundamental principles: optimization of electrocatalytic activity and long-term stability in acid media ($\text{pH} < 1$) at high potential (0.8 V). We report here a solution-based approach to the preparation of Pt-based alloy with early transition metals and realistic parameters for the stability and activity of Pt3M (M = Y, Zr, Ti, Ni, and Co) nanocatalysts for oxygen reduction reaction (ORR). The enhanced stability and activity of Pt-based alloy nanocatalysts in ORR and the relationship between electronic structure modification and stability were studied by experiment and DFT calculations. Stability correlates with the d-band fillings and the heat of alloy formation of Pt3M alloys, which in turn depends on the degree of the electronic perturbation due to alloying. This concept provides realistic parameters for rational catalyst design in Pt-based alloy systems.



(a) Oxygen ion signal of TOF-SIMS analysis, integrated over depth on a $100 \times 100 \mu\text{m}^2$ Pt TE. This switching cell was electroformed by applying a positive voltage to the TE. The depth profiles of each element at a dark point (A) and a bright point (B) are plotted in (b) and (c), respectively. The depth profile of oxygen in the TE at B shows a higher concentration of oxygen than A, which is almost identical to that in the pristine.

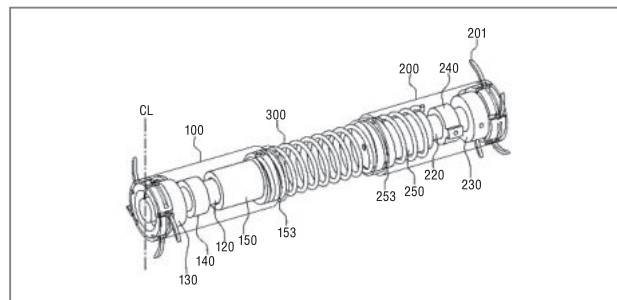
Copyright 2008, American Institute of Physics

BIDIRECTIONAL MOVING MICRO-ROBOT SYSTEM

U.S. 8322469 (2012.12.04)

Yoon, Eui Sung / esyoon@kist.re.kr

Disclosed herein is a bidirectional moving micro-robot system. The bidirectional moving micro-robot system has a first body having a plurality of legs foldably/unfoldably connected thereto, a second body having a plurality of legs foldably/unfoldably connected thereto and a connection member having both end portions respectively connected to the first and second bodies. In the bidirectional moving micro-robot system, the length of the connection member exposed between the first and second bodies is extended or contracted.

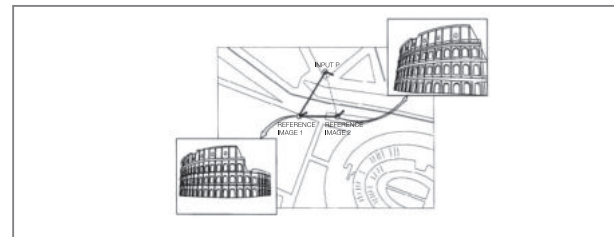


METHOD FOR GEOTAGGING OF PICTURES AND APPARATUS THEREOF

U.S. 8320706 (2012.11.27)

Kim, Ig Jae / drjay@kist.re.kr

Provided are a method and an apparatus for tagging a photograph with information. The method of tagging a photograph with information, which calculates a shooting position of an input image from reference images, includes: selecting a plurality of reference images; calculating a relative shooting position of the input image to the shooting positions of the reference images; calculating the shooting position of the input image on the basis of the calculation result; and storing the shooting position and shooting direction information on the input image in an exchangeable image file format (EXIF) tag of the input image.

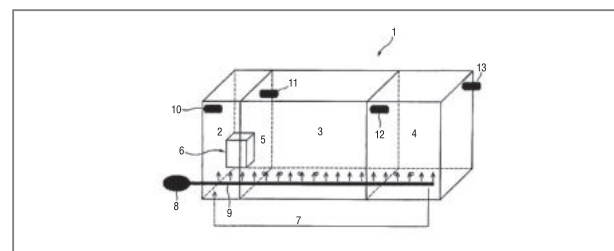


APPARATUS FOR DEODORIZING SEWAGE TREATMENT PLANT SLUDGE BY USING NATIVE MICROORGANISMS

U.S. 8298416 (2012.10.30)

Park, Wan Cheol / wcpark@kist.re.kr

The present invention relates to a deodorizing apparatus using native microorganisms. Specifically, the present invention relates to a deodorizing apparatus using native microorganisms for removal of malodors of sewage treatment plant sludge, comprising a native microorganism activating tank, where a colony of the native microorganisms in a spore state is germinated and activated through a proliferation process under conditions where oxygen and organic materials are supplied, and the native microorganisms returned from a second deodorizing tank is further activated; and a first and a second deodorizing tanks which remove malodorants from untreated matter under conditions where oxygen and the activated native microorganisms are continuously supplied. The deodorizing apparatus of the present invention, which is an eco-friendly and economical method using native microorganisms, can effectively remove malodor generated from various types of sludge including a primary sludge, a secondary sludge, a sludge containing night soil, etc. produced from sewage treatment plants.

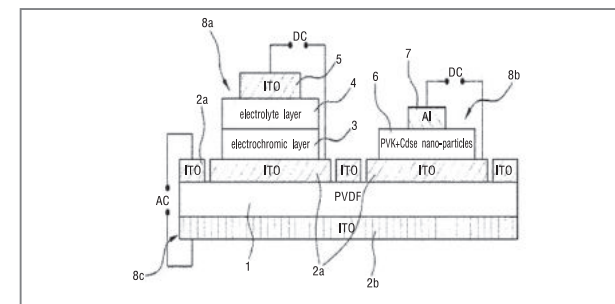


HYBRID ELECTRIC DEVICE USING PIEZOELECTRIC POLYMER SUBSTRATE

U.S. 288776 (2012.10.16)

Choi, Won-Kook / wkchoi@kist.re.kr

The present invention relates to an integrated, composite hybrid electric device in which various devices are formed as a single unit on one flexible substrate, and a fabrication method thereof. More particularly, the present invention a hybrid electric device in which a display device, a vibration-generating (or vibration-sensing) device, and a non-volatile memory device are formed on a single flexible piezoelectric polymer substrate into a single unit by using a flexible piezoelectric polymer substrate whose both surfaces are thinly deposited with a patterned transparent oxidation electrode, and a fabrication method thereof.



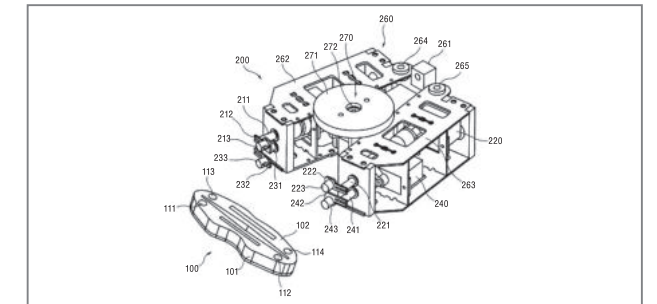
LIP MOVING DEVICE FOR USE IN ROBOTS

U.S. 8280553 (2012.10.02)

Kim, Seung-Jong / sjongkim@kist.re.kr

Various embodiments of a lip moving device for use in robots are provided. A lip moving device has first and second lip members. The first and second lip members are made from a flexible material. First and second driving parts apply torques to both ends of the first lip member, while third and fourth driving parts apply torques to both ends of the second lip member. The first and third driving parts are mounted in a first frame. The second and fourth driving parts are mounted in a second frame. The first and second frames are pivotally

coupled to a supporting part. An adjusting part pivots the first and second frames relative to the supporting part to adjust a distance between the first and second frames.

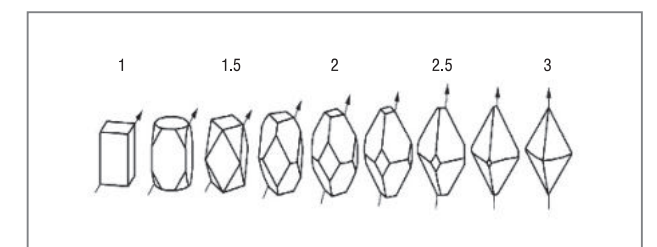


METHOD FOR GROWING THIN FILM

U.S. 8247031 (2012.08.21)

Baik, Young Joon / yjbaik@kist.re.kr

Disclosed is a method for growing a thin film, which includes modifying a surface grain size and surface roughness on a thin film to improve the mobility of a carrier and a light scattering effect. The method for growing a thin film includes: forming nuclei of grains having various grain orientations on a substrate; causing first grains having a first specific grain orientation to grow predominantly among the grains having various grain orientations, thereby forming a first preferred texture comprised of the predominantly grown first grains; and then causing second grains having a second grain orientation to grow predominantly, thereby forming a second preferred texture comprised of the predominantly grown second grains, wherein the surface grain size of each of the second grains forming the second texture is larger than that of each of the first grains forming the first texture.



Vietnamese Ambassador Attends KIST-IRDA Colloquium

September 18, 2012

KIST's International R&D Academy (IRDA) has established a tradition of holding colloquiums for its students and visiting foreign scientists at which foreign ambassadors to Korea are invited to speak. The goal of these colloquiums is to encourage science and engineering graduate students to develop an international perspective in their research work as well as their lives as global citizens. The most recent event featured the Vietnamese Ambassador to Korea, Tran Trong Toan, and was held in Conference Room 1 of KIST's International Cooperation Building on Tuesday, September 18, 2012, at 4:00 p.m. The ambassador gave an animated lecture to more than 70 graduate students. Providing clear examples, he introduced the students to many parallels between Korea and Vietnam, including cultural values and historical ties. He also conveyed, through an extensive range of data, thought-provoking ideas on reinforcing the cooperative relationship between the two countries. Prior to the colloquium, in his meeting with KIST President Dr. Kil-Choo Moon, the ambassador praised the rapid economic growth and advancement of science and technology in Korea, and during his speech, he pledged continued support for further cooperation in these areas through KIST and IRDA. After the lecture, the ambassador conversed with KIST's Vietnamese students. He

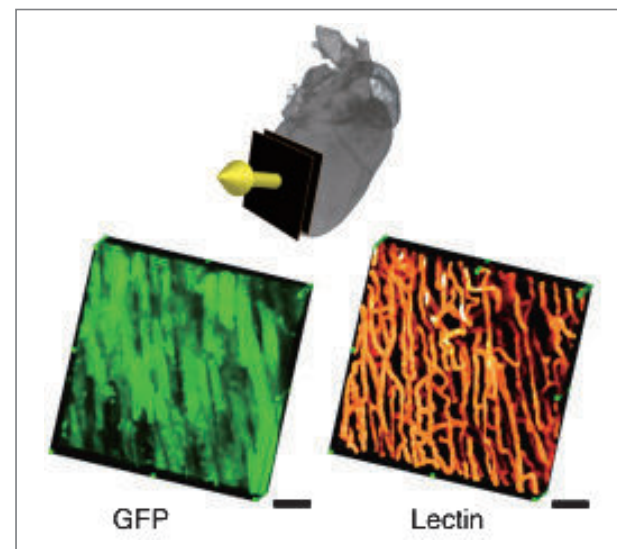


emphasized their important role in facilitating cooperation between Korea and Vietnam and urged them to continue devoting themselves to their studies.

KIST and Harvard Medical School Conduct Joint Research to Develop Cardiac Imaging Technology

September 18, 2012

Joint research involving the teams of Dr. Sungon Lee of KIST's Interaction and Robotics Research Center and Dr. Claudio Vinegoni of Harvard Medical School has produced improved technology for the real-time imaging of live rats' hearts with a high-magnification microscope. Although the microscope is essential equipment in bio-phenomenon research because it enables highly magnified observation in real time, it is limited by the need for the observed organism to remain immobile. Even the most minor movements have posed challenges, particularly those resulting from the autonomous movement of myocytes and the organism's breathing. The joint research team developed groundbreaking technology for the improved observation of a live rat's heart: a precision mechanical device that effectively fixates the heart and an image processing technique that restores distorted images. By this method, the team succeeded

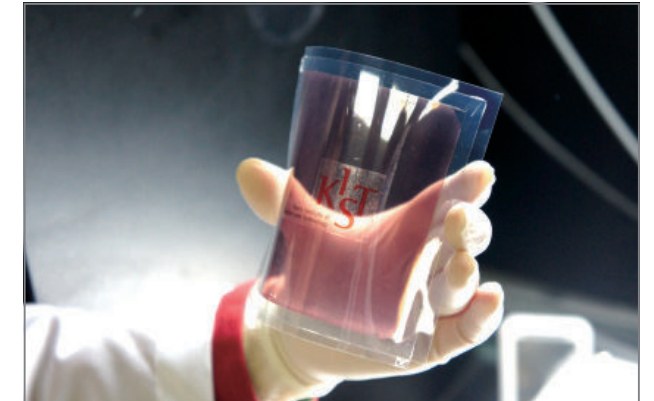


in observing the movement of leukocytes to a point of inflammation through cardiac vessels. The fixation device immobilizes the imaging section of the heart without imparting excessive pressure. It is composed of a peripheral section that fixates the imaging area and a precision location adjustment section. The peripheral section is ring-shaped with a diameter of 2.3mm, and a surgical adhesive approved by the FDA is coated on the ring to hold the object without exerting pressure. Meanwhile, the image processing technique developed by the joint research team recomposes the images via the "gating" method, using the signals at particular locations selectively. The laser scanning microscope currently used in bio-engineering research, which generates images by 2-dimensional scanning, produces distortions if the subject moves during the procedure; the new technique can generate non-distorted images by finding the portions with the least movement in various images and recombining them using ECG and respiration information. This technology is highly significant; it can be used to investigate causes of cardiac diseases and to aid in research on the development of related drugs. It can also be used to observe other organs besides the heart, which has been difficult with existing technology. The results of the research were published on September 11, 2012, in the online issue of *Nature Communications*, a sister publication of the globally respected academic journal *Nature*.

KIST Team Develops Unique Solar Cell Technology

September 20, 2012

A joint research team headed by Dr. Min Jae Ko of the Photo-Electronic Hybrids Research Center and Dr. In Suk Choi of the High Temperature Energy Materials Research Center has developed a dye induction solar cell technology that is transparent and remarkably flexible. The solar cell uses inexpensive dye and nanotechnology to produce both a wide range of colors as well as transparency. The team developed technology for forming



organic and inorganic hybrid photo-electrodes made up of macromolecular nano-fiber and titania nano-particles using a macromolecular electricity spinning method and inorganic nano-particle spray method simultaneously. The new solar cell displayed almost no cracking or reduction in efficiency, even under repetitive bending in more than 1,000 tests. The photo-electrode's mechanical durability is explained by its ability to firmly fixate the inorganic nano-particles and the ability of the flexible macromolecular nano-fiber to absorb external impact, thus fundamentally inhibiting the occurrence and spread of cracks. The research was published on September 20, 2012, as the cover page thesis for the October issue of *Energy & Environmental Science*, the foremost academic journal in the areas of energy and the environment.

KIST Recognized as the Great Work Place in Korea

October 25, 2012

KIST received the "Grand Prize for Great Work Place (GWP) in Korea" after being selected as one of the top 100 GWPs in the country and receiving the highest score by the evaluating institution in a tight national competition. GWPs are selected each year in 45 countries, including those in the EU, Central and South America, China and Japan. Fortune 100 companies based in the U.S. are evaluated using the same criteria, ensuring that comparative results are objective and meaningful. The selection is made through in-depth analysis of employee



satisfaction in light of institutional values such as trust, respect, fairness, pride and interest, as well as quality of the overall organization of the institution. KIST has been among the top 100 GWPs in Korea every year since 2002. The standards embodied by KIST that have led to its recurrent selection include the values of trust and sharing, the establishment of an amicable work place, a united culture of communication and hard work, and contributions to society through shared talents. KIST President Dr. Kil-Choo Moon accepted the prize at the GWP Korea award ceremony, which was held in the Convention Center of the 63 Building on October 25, 2012.

Ceremony Marking the Completion of KIST Jeonbuk Institute of Advanced Composite Materials

November 8, 2012

The ceremony marking the completion of the Composite Material Research Institute, the third research center comprising KIST Jeonbuk Institute of Advanced Composite Materials, was held on November 8, 2012, and was attended by more than 300 people from industry and academic research centers in the science and technology field. KIST Jeonbuk branch has more than 70 researchers, 20 of whom hold Ph.D.s, and includes two previously established research centers: the Soft Innovation Material Research Center and the Carbon



Fusion Material Research Center. The branch is intended to be the domestic base for global-level composite materials technology research. The number of researchers with Ph.D.s is projected to rise to 100 by 2014. With construction completed, the Jeonbuk branch will work on developing technology for high-function and high-value composite materials, including carbon materials, and to provide support to companies specializing in component and composite materials. KIST President Dr. Kil-Choo Moon stated, "the global market for composite material will reach 6.4 trillion won by 2015," and "KIST's Jeonbuk branch will make substantial contributions toward the reinforcement of national industrial competitiveness as the hub institution for research and development of the most advanced composite materials."

KIST Hosts the 2nd Hongreung Forum

November 27, 2012

The 2nd Hongreung Forum was held at KIST on Tuesday, November 27, 2012, at 10:00 a.m. It was presided over by Committee Chairman Dae Hwan Jang, Chairman of Maekyung Media Group, and included participation by 12 universities and a large number of research institutions based in the Hongreung area. The concept of Hongreung is that it will lead Asia as a region of idea generation and innovation. It is already an area of highly concentrated knowledge; within a 2km radius, it boasts more than 5,000 researchers with Ph.D.s. The



Hongreung Forum was inaugurated in July of 2012 for the purpose of defining future policy in an era of global convergence. The theme of this year's forum was "Hongreung Over the Next 50 Years." Blueprints laying out the planned development of Seoul's northeastern regions were shown, and Seoul's mayor, the Honorable Won Soon Park, presented the overall vision for the area, while Mr. Dong Ju Choi, Chairman of the Committee on Financial Projects at Kyung Hee University, proposed specific areas of growth expected to fuel economic development, such as green technology. Panel members included Jong Won Park, President of the Korea National University of Arts; Hong Bin Kang, Director of the Seoul Museum of History; and Byeong Gyu Yoo, Director of the Economic Research Center at the Hyundai Research Institute. The panel held a spirited debate on how the plans for northeastern Seoul should be implemented.

Ceremony Marking the Completion of the Accelerator Research Building

February 7, 2013

KIST celebrated the opening of the facility housing a 6 MV class medium- to large-scale electrostatic ion beam accelerator, which can be utilized for age-dating and advanced bio-research and materials research. The ceremony was held on Thursday, February 7, 2013 and was attended by more than 50 personnel and guests, including government officials and academic specialists

from Korea and abroad. The facility began operation in earnest immediately following the ceremony. Ion beam accelerators can analyze the internal composition of objects without destroying them. The equipment accelerates and collides various chemical elements with the sample material at high energy levels, and then measures the energy of X-rays and scattered particles generated from the collision. It is used in non-destructive ingredient analysis and the manufacture of semi-conductors. Electrostatic accelerators similar to the new one at KIST are currently in operation at the Korea Institute of Geoscience and Mineral Resources and at Seoul National University. The KIST facility contains 6 MV and 2 MV electrostatic accelerators with 400kV capacities. In Korea, existing accelerators below the 3 MV class are used for carbon dating but are limited to using only chemical elements, while 6 MV class medium-large scale ion beam accelerators offer significantly greater capability by measuring more diverse radioactive isotopes ranging from hydrogen to aluminum, chlorine, iodine and calcium. These accelerators are expected to make substantial contributions to the creation of next-generation growth engines since they can be widely applied in areas such as climate change research and environmental monitoring technology, semi-conductor manufacturing, the materials industry, and the development of new drugs.



KIST's Gangneung and Jeonbuk Branches

Serve as Regional Hubs of Cooperative Research

KIST established branches for specialized research first in Gangneung (2003) followed by Jeonbuk (2007). These branches were seen as a way to bring balanced economic growth to their regions by using manpower and other resources in the surrounding areas while serving as hubs for cooperative activities among industry, academia and research institutes. The following summary describes how the branches were conceived and developed, and the types of projects and research activities in which the branches are involved.

The Gangneung Branch

- In 1996 Gangneung City approached KIST about the possibility of establishing a research branch to promote the development of science and technology in the region. This proposal was part of a strategic development plan developed by the city to establish an advanced science industrial complex. Support for the plan was so strong that, despite a slowdown stemming from the IMF crisis that began in 1997, many important aspects of the future project were decided during the crisis years.
- The establishment of KIST's Gangneung Branch was formally approved in May

completed in 2005, reflected the branch's focus by using natural materials.

- The Gangneung Branch has played a central role in the advancement of science and technology in Gangwon Province. Not only does it pursue vital basic research, it has also been responsible for the development of an increasingly skilled and creative workforce through its Science and Technology Training Center, completed in 2009. In addition, the branch has opened a Science Experience Center designed for children to have hands-on experience in a wide

2003. It was decided that the branch would specialize in the research of natural materials and be organized into three centers: The Natural Medicine Center, The Functional Natural Substance Center and The Environmental Research Group. Even the construction of the research facilities,

range of scientific topics. Between 1300-1500 children visit the center each year. The branch also hosts various events including youth science classes, bio-science camps, high school internships and organizes events promoting general scientific cultural awareness.

- During its short history the branch already has many notable research achievements. These include the publication of 450 articles, 66% of which were registered in the Science Citation Index (SCI). 162 patent applications have been made of which 71 have been registered as of the end of 2012. Out of these, five technologies have been transferred.
- As it continues its efforts to promote health through discoveries related to natural substances, the Gangneung Branch plans to pursue research in diseases related to aging and metabolism including menopausal disorders, degenerative brain diseases and a wide range of metabolic diseases.

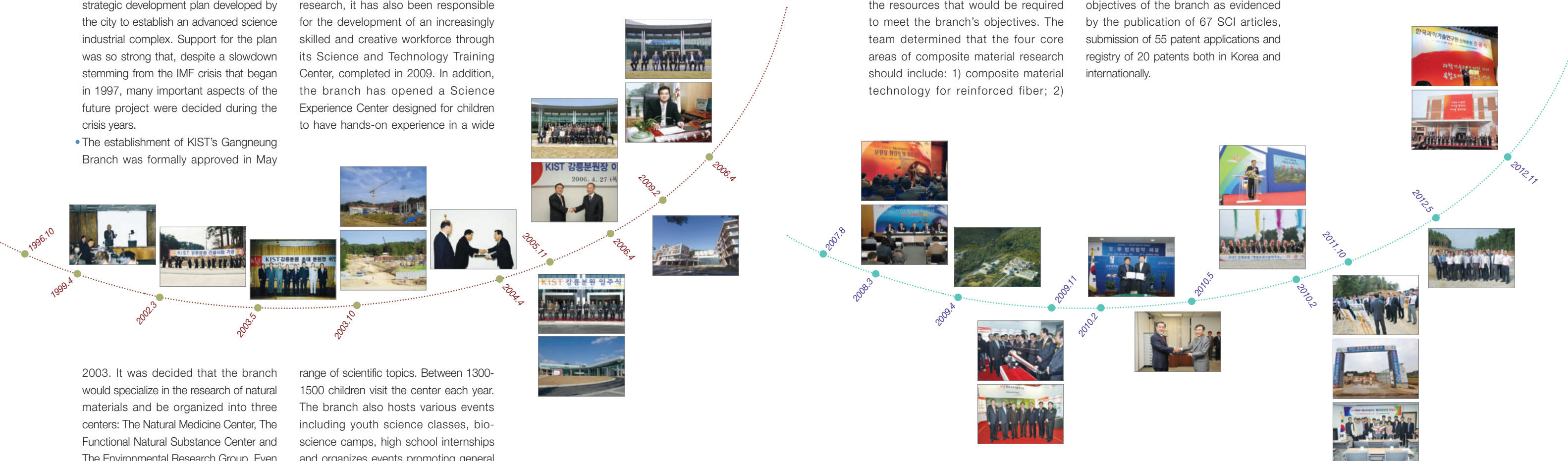
The Jeonbuk Branch

- Jeollabuk Province is a region of extensive plains where agriculture was dominant until the 1970's. Largely left behind by the rapid industrial growth of the last forty years, the province determined that an aggressive strategy was needed to bring economic growth to the region in the 21st century. The composite carbon material industry was identified as a way to do this, and KIST was subsequently asked by the provincial government to establish a branch to pursue research in composite materials. The branch was approved in 2007.
- KIST's initial Jeonbuk team identified the type of research activities that should be pursued at the new branch and the resources that would be required to meet the branch's objectives. The team determined that the four core areas of composite material research should include: 1) composite material technology for reinforced fiber; 2)

composite electronics material technology using nano-carbon; 3) composite macromolecular material technology using nano-dispersion; and 4) composite carbon-based energy material technology. Research has ultimately been organized into two centers: The Soft Innovation Materials Center and The Composite Carbon Materials Center.

- As planning continued prior to the branch's opening in 2012, cooperation agreements with regional universities were negotiated, resulting in collaborative arrangements for joint research with Chonbuk National University, Jeonju University and Kunsan National University. Also before construction was completed, researchers were already fulfilling the objectives of the branch as evidenced by the publication of 67 SCI articles, submission of 55 patent applications and registry of 20 patents both in Korea and internationally.

- Now in full operation, the Jeonbuk Branch is fully prepared to fulfill its role as the promoter of regional industrial growth, specifically in the area of composite materials. It will act as a center for cooperation between the industrial, academic and research sectors and be a leading participant in the global network of institutions working on composite material advances. Furthermore, it will bolster national economic development efforts and discourage costly duplication of research investment by installing expensive, state-of-the-art equipment that can be shared with industrial companies, private sector research institutes and academic institutions.



What do the Louvre Museum and KIST have in common? An ion beam accelerator.

KIST recently completed installation of a 6 MV ion beam accelerator to expand research in many fields, including biomaterials, geology, bio-chemistry, archaeology, environmental studies and earth science.



Dr. Jong Han Song explains 6MV ion beam accelerator.

If you climb the hill behind KIST to view the entire campus, you may be struck by one building in particular. It's a handsome structure that, until recently, had been hidden under a veil of construction. This is the Accelerator Research Building, with modern black and grey tones and clear glass windows that allow a majestic view of the surrounding area.

As you enter the first floor of the building, a huge cylindrical structure immediately comes into view. This is the 6 MV electrostatic ion beam accelerator. The complex structures and high ceilings of the interior are reminiscent of a complex movie set at a major film studio.

The accelerator installation project was initiated in 2006 as part of an effort by Korea's Ministry of Science and Technology to establish large-scale scientific facilities for basic science. The installation of the accelerator, including the dedicated research building was completed over a period of five to six years; in 2007, the Ministry of Science and Technology granted KIST full authority over

the project. The Accelerator Research Building opened on February 7, 2013.

According to Dr. Jong Han Song, the researcher in charge of the electrostatic ion beam accelerator lab, other types of accelerators have been installed elsewhere in Korea: a photon beam accelerator in Pohang and a proton accelerator in Gyeongju. Additionally, there are plans underway for the installation of a heavy ion accelerator within Korea's International Science and Business Belt. However, while these accelerators can each perform electron structure analysis, critical nuclear spallation and basic physics research, their methods and features differ from one another so that each offers unique research capabilities.

The accelerator is used for elemental analysis by measuring energy during the collision between high energy incident ions and target atoms. Ion implantation and micro-machining are other applications of the ion beam accelerator. It is useful in many areas of research.

Accelerator mass spectrometry (AMS) is another application of the accelerator and can be used in the areas of bio- and environmental science, geology, biochemistry and archaeology. It can perform analysis on even minute quantities of samples. Consequently, numerous countries throughout the world are taking steps to implement AMS to enhance their research programs.

The newest accelerator at KIST is a 6 MV class, large-scale electrostatic accelerator. It will be used for AMS and ion beam research. In contrast to the 1 MV and 1.7 MV AMS accelerators owned by Seoul National University and the Korea Institute of Geoscience and Mineral Resources, the 6 MV accelerator installed at KIST can analyze heavier isotopes including aluminum (Al), chlorine (Cl) and calcium (Ca). This will allow for expanded research into new areas of living matter and the environment.

So what's inside the accelerator? How does it analyze samples? Dr. Song pulled the handle on the front of the accelerator as if opening the door to a secret chamber, revealing hundreds of holes, as if the equipment had been riddled by bullets. He explained that this area, referred

to as the AMS "ion source," is where the samples are placed. The KIST accelerator has two AMS ion sources. One holds 200 sample carousels, the other holds 50 samples. He added, "samples are analyzed by placing them into the black holes of the pellet."

Determining the truth behind the Shroud of Jesus

Dr. Joonkon Kim, who is in charge of accelerator management and research at the Advanced Analysis Center (AAC), outlined the accelerator's many useful applications. For example, he described how it plays a significant role in the measurement of past climates and temperatures, the development of new drugs, and even the dating of ancient artifacts.

"It is possible to reconstruct the climate and temperatures as well as the atmospheric conditions 100 years ago by observing bubbles in the snow in the South Pole or Greenland with the ion beam accelerator. In particular, it has the advantage of enabling analysis even with very minute quantities of samples," he said.

Dr. Kim described the accelerator's potential application in the development of new drugs. By analyzing a blood or urine sample, he said, "the equipment can measure how the drug administered to people is metabolized, the substances it disintegrates into, how long it stays in the body, and the organs it infiltrates."

In addition, he explained, "the accelerator can take measurements with only 1mg of specimen, while the widely used liquid scintillation counting (LSC) method needs more than 1g. Moreover, it can take measurements within several minutes, while other methods require as many as several days. It is used frequently in archaeological research since it uses only very small quantities of specimen is enough to get a meaningful data, even though it is not completely non-destructive."

In fact, AMS accelerators ended the dispute over whether the Shroud of Jesus, discovered in Italy, was genuine or fake, while here in Korea, the person buried in the nameless tomb found in Gyeongju was identified by this method. Not surprisingly, many prestigious institutions

that conduct archaeological research have recognized the benefits of AMS. According to Dr. Song, one of these is the Louvre Museum which uses a 2 MV tandem accelerator.

Anything containing carbon can be age-dated

Can the accelerator analyze anything in the world? Dr. Byung Yong Yu of the Advanced Analysis Center is responsible for specimen research. He stated, "specimens can be made from anything that contains carbon."

Dr. Yu described the method used to date animal and plant specimens. Carbons in the atmosphere, he explained, include carbon 12, carbon 13 and carbon 14. While the majority of carbons are carbon 12 (99%) and carbon 13 (1%), carbon 14 exists at a ratio of 1 for every 1 trillion carbon 12's. Carbon dioxide in the atmosphere is constituted into plants through photosynthesis, and joins the ecosystem when animals consume the plants. Therefore, the ratio of carbon 14 to carbon 12 is consistent while an organism is alive. However, once the organism dies, the external supply of carbon is stopped (interrupted). While the quantities of carbons 12 and 13 are maintained at the time of this interruption, the quantity of carbon 14 decreases with time, reaching 50% in 5,730 years. Thus, dating can be achieved by finding the ratio of carbon 12 to carbon 14.

Dr. Yu said, "It is possible to date the age up to 60,000 years by using these characteristics of carbon. It is very helpful in disclosing the history of human development, as



well as the origin of humankind.” He also explained that “any substance that contains carbon, including paper, hair, bone, cloth, soil, timber, charcoal and ironware, can be used as a specimen” and that “age dating can be performed for shellfish in the ocean or in fresh water by extracting the carbon contained in the shell, as shellfish consume carbon dissolved in the water.”

Prior to analysis in the accelerator, it is important to obtain some initial data on the specimen. Preliminary processing of the specimen is conducted in the following sequence: physical treatment to remove pollutants → chemical treatment → oxidation to extract carbon dioxide → acquisition of carbon by reducing the carbon dioxide under a hydrogenated environment, using iron powder as a catalyst.

Processing takes a long time, and the reduction procedure for obtaining carbon from carbon dioxide is the most important stage in the process. KIST recently designed, and is currently manufacturing, reduction equipment that can reduce 12 samples simultaneously. This way, experiments may be performed by a greater number of researchers, and data can be generated faster.

Illustration of method of production of soil sample

In order to date soil, carbon must be obtained from humic acid. Humic acid is generated when microorganisms in the soil disintegrate organic substances. The method for producing an analysis-ready specimen from soil is as follows:

Roots and other organic matter present in the soil are removed under a microscope → the soil undergoes chemical treatment to obtain humic acid → organic matter is secured → the organic matter is heated under an oxygenated environment → water and carbon dioxide are generated → water is removed and the carbon dioxide is converted into carbon, producing the specimen.

Future research collaboration

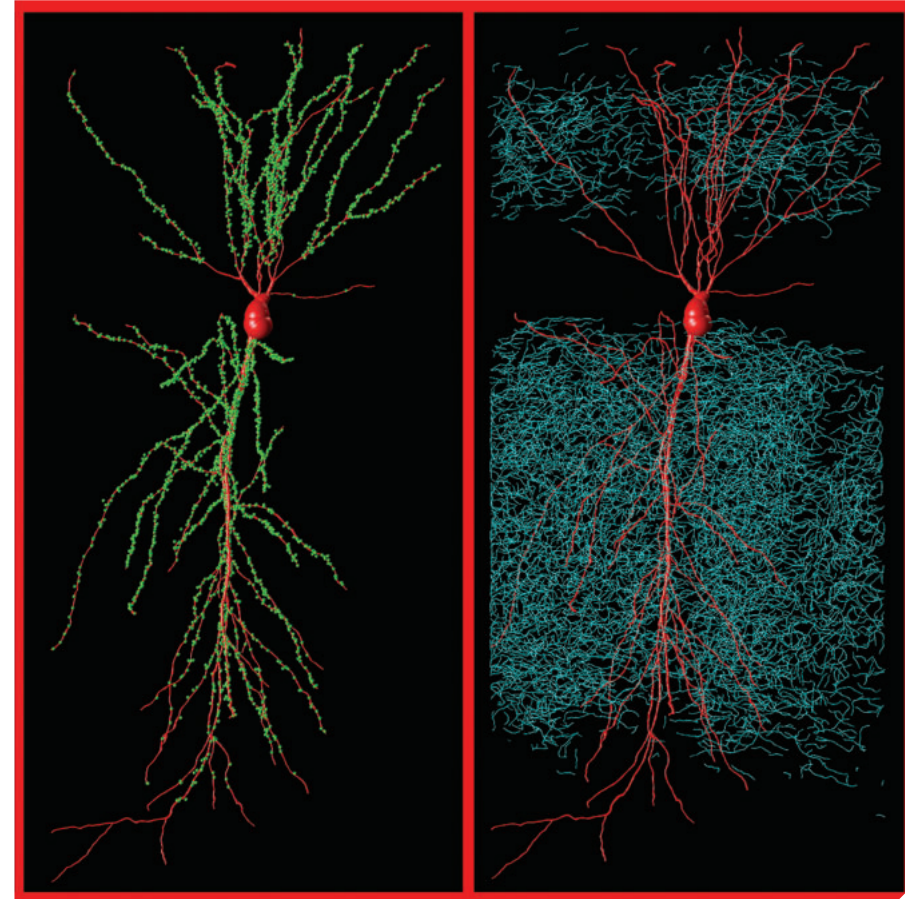
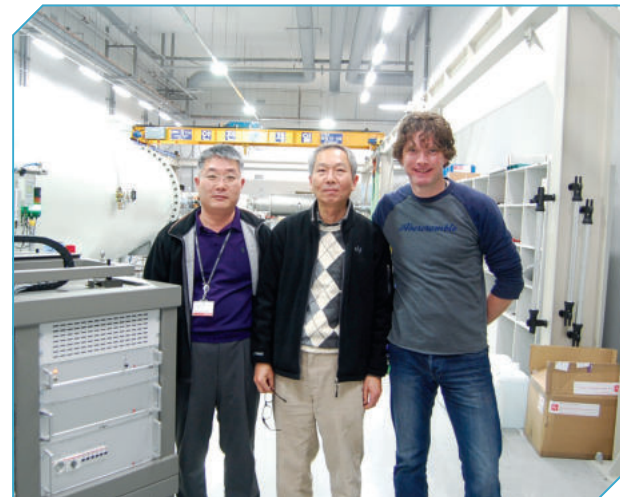
KIST is planning to use the ion beam accelerator not only for in-house research but also for joint research with other organizations and educational institutions. In light of the strong government support that was provided to successfully install the accelerator and its infrastructure,

the facility will be used as a national research facility.

Dr. Joon Gon Kim affirmed this collaborative approach by stating, “even though enterprises and educational institutions purchase an accelerator by investing several hundred million Korean won, there are still numerous difficulties due to the large space it takes up and the high cost of its maintenance...we will assertively establish the means of jointly utilizing the facility with external researchers.”

In particular, KIST is planning to share the process and technology used to produce specimens. Dr. Song and Dr. Kim explained that if, for example, a team from the Research Institute of Cultural Heritage wanted to use the facility, they would not be able to unless they also had the ability to produce specimens. This is where KIST can provide valuable support to external researchers who need the equipment but do not have their own specimen production process. Dr. Song and Dr. Kim added that KIST plans to implement an open laboratory policy in order to provide assistance in utilization of the equipment, thus enabling continuous research in relevant areas.

With the newly installed 6 MV accelerator and the relocation of previously owned 2 MV accelerators, KIST now owns three ion beam accelerators housed in a facility designed to greatly enhance joint research at the most advanced scientific levels.



Cover image mGRASP : Our software neuTube-generated reconstruction shows synapse (green) detected by mGRASP with hippocampal CA1 dendrites (red) and CA3 axons (blue)

Editorial Information

Editor-in-Chief
Byung Gwon Lee

Editorial Board Members
Hae-Young Koh
Hyun Kwang Seok
Il Ki Han
Joonyeon Chang
Youngsoon Um
Seok Won Hong
Jongjoo Kim
Seung Yun

Managing Editor
Kwihyang Han
kiwihyang@kist.re.kr
Editorial Office Telephone
+82-2-958-6313
Web Address
www.kist.re.kr/en

English Advisory Services
Anne Charlton
The Final Word Editing
Services
the_final_word@live.com

KIST Korea Institute of
Science and Technology

Hwarangno 14-gil 5, Seongbuk-gu, Seoul 136-791,
Republic of Korea
Tel +82-2-958-6313 www.kist.re.kr/en
E-mail kiwihyang@kist.re.kr